Design of a Misalignment Tolerant Control Scheme for a Bidirectional Inductive Charging System for Electric Vehicles

by

W. Vermeer

to obtain the degree of Master of Science
at the Delft University of Technology,
to be defended publicly on Monday September 10, 2018 at 10:00 AM.

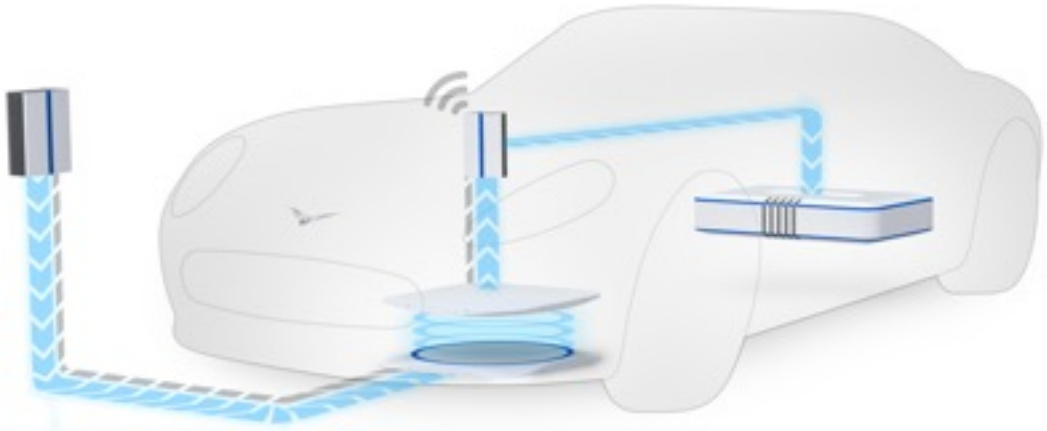

Student number:	4623134	
Project duration:	December, 1 2017 – September 1, 2018	
Thesis committee:	Prof. dr. ir. P. Bauer,	TU Delft
	Dr. ir. Z. Qin,	TU Delft
	Dr. ir. S. Tindemans,	TU Delft
	Ir. S. Bandyopadhay,	TU Delft

This thesis is confidential and cannot be made public until December 31, 2018.

An electronic version of this thesis is available at `http://repository.tudelft.nl/`.

CONTENTS

Abstract

In modern society the increasing energy demand, the depletion of fossil fuels, and the environmental polution which comes with it, are one of the biggest global problems. Therefore the transition towards a renewable transport and energy system is becoming more and more important. Electric vehicles are a big part of this transition and therefor the use of them should be promoted. However drawbacks such as operating range and charging time are obstacles for this transition. Inductive charging can help overcome these drawbacks using opportunity charging and because of its ease of use.

In this thesis the design and implementation of a misalignment tolerant control scheme for a bidirectional inductive power transfer is discussed. This control scheme allows the transformer coils to be misaligned while ensuring maximum power transfer efficiency of the inductive link. To do this the resonance frequency of the primary or secondary current is tracked. Furthermore two dc/dc converters are used before the inverter and after the rectifier, here one is used for controlling the power while the other is tracking the maximum power transfer efficiency point (MEPT). In order to calculate this MEPT, the coupling of the transformer coils is calculated using the secondary (or primary, depending on the direction of power) dc link currents and voltages.

The first part of thesis is a literature review including an investigation of the dynamics of a series-series resonant tank, part of this analysis is about the bifurcation phenomena. Since for control purposes it is important to determine the conditions for bifurcation free operation and the effects of bifurcation. Next, the best control scheme for controlling the output power is discussed and finally the proposed misaligment tolerant control scheme is proposed including how to estimate the transformer coupling and how to track the resonance frequency. It was found that using the MEPT control scheme bifurcation is always avoided.

The second part of this thesis is about the dynamic modelling and the design of the controllers. This dynamic model is comprised out of three different models, two of which are the dc/dc converters and one is the inductive link (specified from inverter input to rectifier output). These models are then combined in order to get the frequency response of the entire system. Based on this model the voltage controllers are designed.

The third and final part of this thesis is about the practical implementation of the needed hardware en the results obtained using the MEPT control scheme. In the end an improvement in efficiency of 5% was achieved at optimal alignment, up to 23% increase under 8 cm misalignment. The total system efficiency at optimal alignment was 80%.

Acknowledgements

This thesis is the final requirement for obtaining the degree of “Master of Science” at the Delft University of Technology at the Electrical Power Engineering departement, in the DC energy storage and systems group. The work done in this thesis could not have been the same without the amount of support i have received throughout the entire process. Therefor i would like to take this opportunity to express my gratitude to all of them.

First and foremost, i would like to give my sincere gratitude and thanks to my daily supervisor Soumya Bandyopadhyay. You have continuously supported me during my thesis and also motivated me to research further beyond the scope of my thesis. I have very much enjoyed working with you.

Also, i would like to acknowledge the help received by Joris Koeners, Bart Roodenburg and Harrie Olsthoorn. Without you i could not have proceeded as much in my practical work as i did now, and you also always supported me with the practical side of my thesis (Including the (seemingly) endless need of TI boards). I want to thank you for this.

Furthermore, i would like to thank Pavel Purgat. Your knowledge of power electronics was very inspiring and this also helped me a lot with the practical side of my thesis.

Next, i would like to show my gratitude to Zian Qin for being my official supervisor and helping me with global requirements of the control system and lending my your experience throughout the project.

Finally, i would like to thank my friends and family for always supporting me and also for providing the necessary distractions when this was necessary.

§

CHAPTER 1

INTRODUCTION

1.1 MOTIVATION

In modern society the increasing energy demand, the depletion of fossil fuels, and the environmental polution which comes with it, are one of the biggest global problems. Therefore the transition towards a renewable transport and energy system is becoming more and more important. Electric vehicles are a big part of this transition and therefor the use of them should be promoted. However drawbacks such as operating range and charging time[1] are obstacles for this transition. In the last years, wireless charging has been investigated as a method to replace plug-in charging to a more safe and convenient way of charging. As opposed to conductive charging wireless charging has the following advantages:

- **Safety** : Because of the isolation between the source and load, there is no shock hazard since there is no need for plugging in a cable. Especially in wet environments this can be beneficial.

- **Ease of use** : Since (stationary) wireless charging only requires the user to park the car over the charging pad, e.g. on their drivelane, it does not require any additional actions since the car will start charging by it self. This can improve the comfort of driving an electric vehicle.

- **Extended Range** : Probably the most important advantage of wireless power transfer is the possibility for opportunity charging and dynamic charging. Opportunity charging is especially useful for public transport, where electric taxi's or buses can charge their batteries when they are stationed at stops hereby increasing their driving range and/or reducing their battery size [2].

Because of these advantages wireless charging can be used to over come the drawbacks of electric vehicles and provide a more safe and easy to use system which can help in the transition to a more sustainable society. Another advantage of wireless charging is that it can be used for dynamic charging, i.e. charging when the vehicle is moving which dramatically increases the driving range.

Figure 1.1.1: Wireless charger for Electric vehicles

When referred to wireless power transfer most of the time inductive power transfer is ment. Here power is transferred using a resonating electromagnetic field, induced by a transmitter coil and picked up by a receiver coil. In the case of electric vehicles, this secondary coil is inside the vehicle, see Figure 1.1.1. The coupling between these coils is directly related to the energy transfer efficiency of the inductive link. However, in the case of an electric vehicle charger the coils can be subjected to a certain misalignment when the vehicle is not exactly aligned with the transmitter.
Therefore:

- the first goal of this thesis is to design and implement a control system for an inductive charging system for electric vehicles which is misalignment tolerant. This means that the system should be able to track the maximum power transfer efficiency of the inductive link for all values of its possible misalignment. This will be done by impedance matching of the transformer to the load using a dc/dc converter.
- The second goal of this thesis is to design the system in such a way that it allows for bidirectional power flow. This way it can act as a storage for sustainable energy sources such as photo voltaic (PV) systems or wind energy systems. In the end it will be part of a multi port DC nanogrid inside a smart dc house. Here the vehicle acts as the battery for the energy sources.

1.2 Research Questions & Objective

The research objective of this thesis summarized in a single sentence is:
To design and implement a misalignment tolerant control scheme for a bidirectional inductive power transfer system for electric vehicles.
In order to achieve this objective, the research questions and methodology below are used. These can be divided into three parts: the first part is a literature review explaining the basics behind inductive power transfer, a review of the most common control methods for inductive power transfer and it will discuss the novel misalignment tolerant control method. The second part consists of the modelling and simulations done to design the controllers and the design of the hardware needed to implement the control system. Finally the third part is the practical implementation of the controllers and hardware including experimental results and loss calculations. Below is a summary of the steps taken to cover these three parts.

- What are the dynamics of a series-series resonant tank?
- How does bifurcation play a role in a series-series resonant tank?
- What is the best control method for controlling the power in a bidirectional misalignment tolerant system?
- How can the system be controlled such that it will always achieve the maximum power transfer efficiency?
- How to estimate the alignment of the transformer coils, while using the charger?
- What method of modelling can accurately and efficiently describe the dynamic behaviour of a series series resonant converter?
- What is the frequency response of this control method and what is the stable region for the closed loop controllers?
- What is the efficiency of the overall system?

1.3 Methodology

The methodology behind this thesis can be divided into three parts:

- The origin and prevention of bifurcation, one of the most common struggles in inductive power transfer control, are analyzed;
- A review of the most common control methods of inductive power transfer are discussed and compared using simulations;
- Based on literature a control scheme for maximum power point tracking will be devised;

- The large signal modelling of the hardware is done in order to design the components needed for this.
- The small signal modelling is done to analyze the transient behaviour of the system
- The controller is designed based on the small signal modelling.
- The hardware is build, debugged and tested. This is first done seperately, after which it will be implemented in the system.
- The controller is implemented on the prototype and the simulations are compared to the experimental results
- A detailed calculation of the losses in the system is done.

1.4 Document Outline

The report is divided into x Chapters, of which the first is this introduction. Furthermore Chapter 2, 3 and partly Chapter 4 are part of the first part of the thesis: the literature review. The second part of Chapter 4, Chapter 5 and 6 comprise the second part of the thesis, the modeling part. Finally chapter 7 and .. make up the final experimental part of the thesis. Below is a short summary of each chapter.

- Chapter 1: Introduction; stating the motivation, research questions and methodology used in the report.
- Chapter 2: Basics of Inductive Power Transfer; including a summary of the mathematics behind inductive power transfer, modeling of a transformer and the use of compensation capacitors, an analysis on the behaviour of a series series resonant tank and the concept of bifurcation and how to ensure bifurcation free operation.
- Chapter 3: Control Methdods for Inductive Power Transfer; a review of the most common control methods of inductive power transfer, discussing the operation of each method and a qualitative comparison between them.
- Chapter 4: Misalignment Tolerance; in this chapter the approach of ensuring maximum power point tracking is discussed. Including the approaches to coupling factor estimation, resonance tracking and zero voltage switching.
- Chapter 5: Modeling; the first part of this chapter consists of the large signal modelling where the design of the dc/dc converter components is discussed. Secondly the small signal model of the dc/dc converters in both buck and boost mode and the inductive power part are discussed.
- Chapter 6: Controller Design; In this part the design of the power and MPPT controller is discussed.
- Chapter 7: Experimental Results; here the implementation of the prototype and the results of this are discussed and compared to the simulations. Also a calculation and analysis of the system effiency is done in this chapter.
- Chapter 8: Conclusion; conclusions and future work.

1.5 Scientific Contribution

The setup shown in Figure 1.5.1, was the starting point of this thesis. It consists of an open loop full bridge inverter with a series-series compensated resonant tank followed by a passive rectifier including a resistive load. The specifications are given in Table 1.5.1. Here power can be changed by changing the input voltage or the pulse width of the inverter.

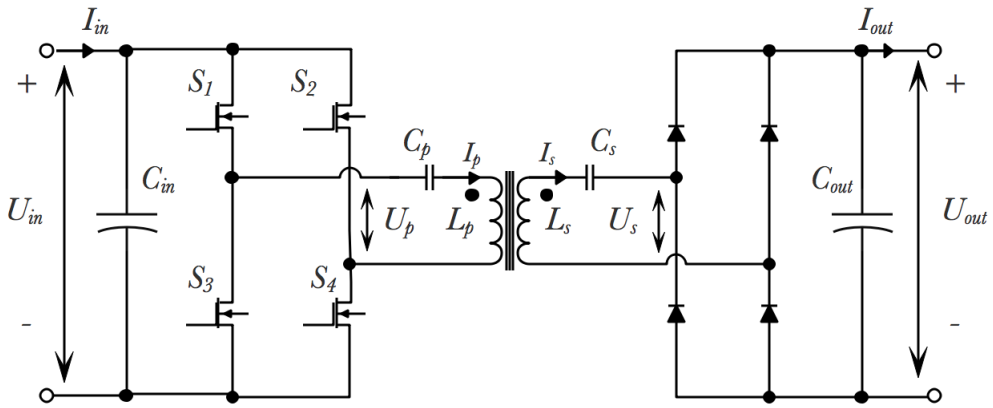

Figure 1.5.1: Setup at the beginning of this thesis

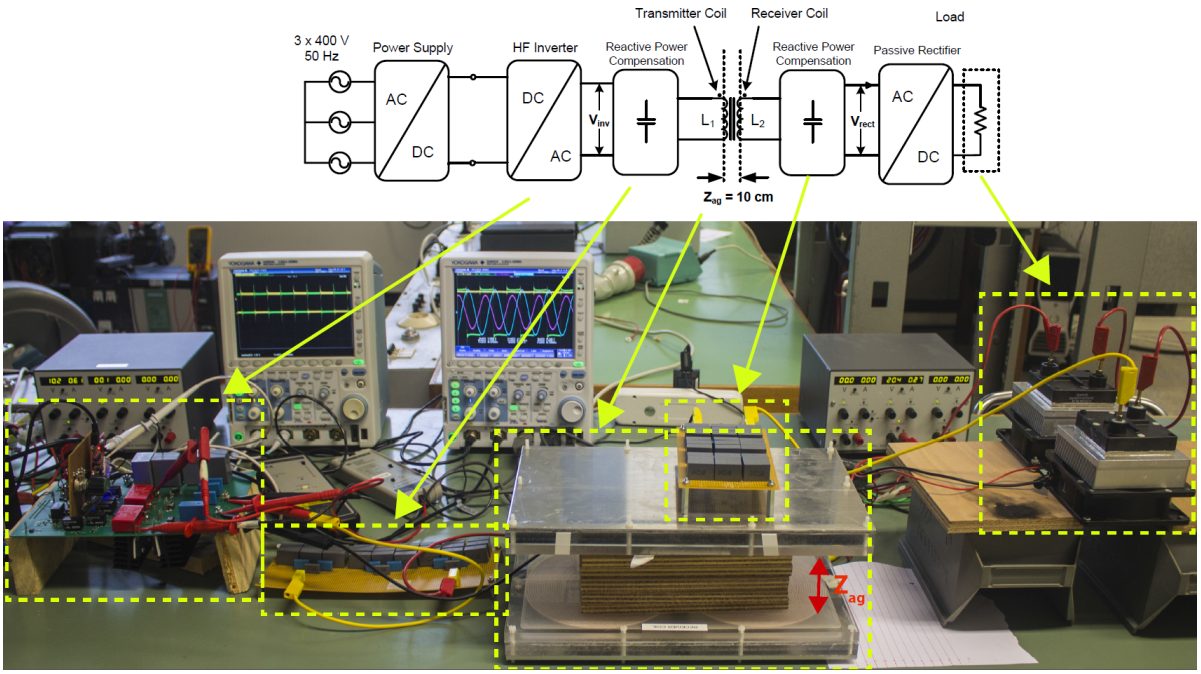

Figure 1.5.2: Picture of the setup at the beginning of this thesis

Figure 1.5.2 shows the setup and control scheme as it is at the end of this thesis. First two half bridge dc/dc converters are added for power control and maximum power point tracking (MPPT). The MPPT converter estimates the coupling of the transformer coils online by measuring the DC link voltage and current (depending on the direction of power this is done on the primary or secondary side). Then based on the power setpoint and coupling MEPT is performed. Both the power and MEPT are controlled by controlling the DC link voltages using PI controllers. The design of these controllers was is based on an analytical model of the entire setup.

Furthermore the passive rectifier is replaced by a synchronous rectifier for better efficiency and to make the system bidirectional. Finally, both the full bridge converters are tracking the resonant current on primary and secondary side for zero voltage switching (ZVS) and maximum power transfer efficiency of the resonant tank. This is done by measuring the phase between the resonant current and the gate voltage, which is then controlled to a reference using a PI controller. All component values can be found in table 1.5.1

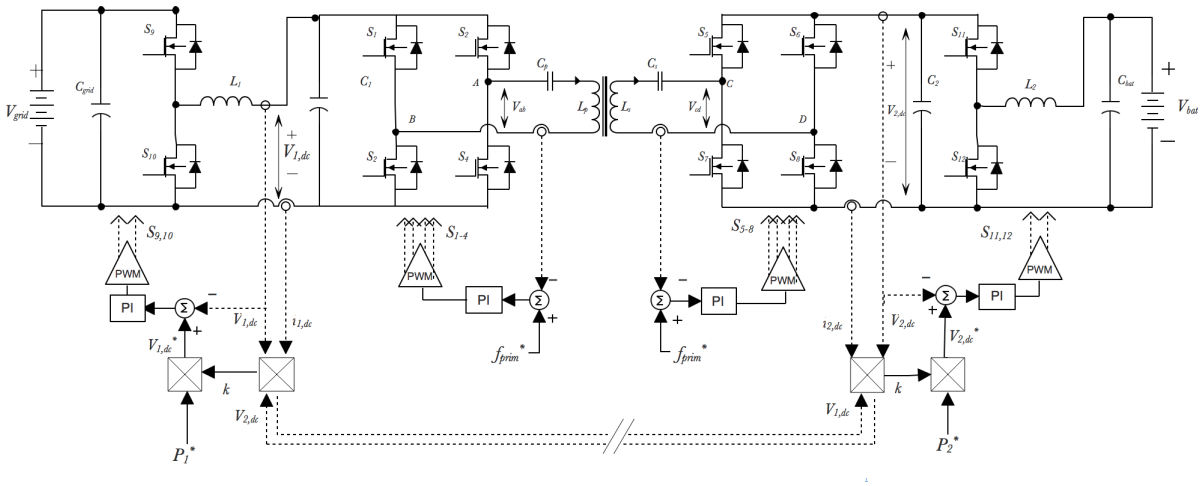

Figure 1.5.3: Final IPT setup and control scheme

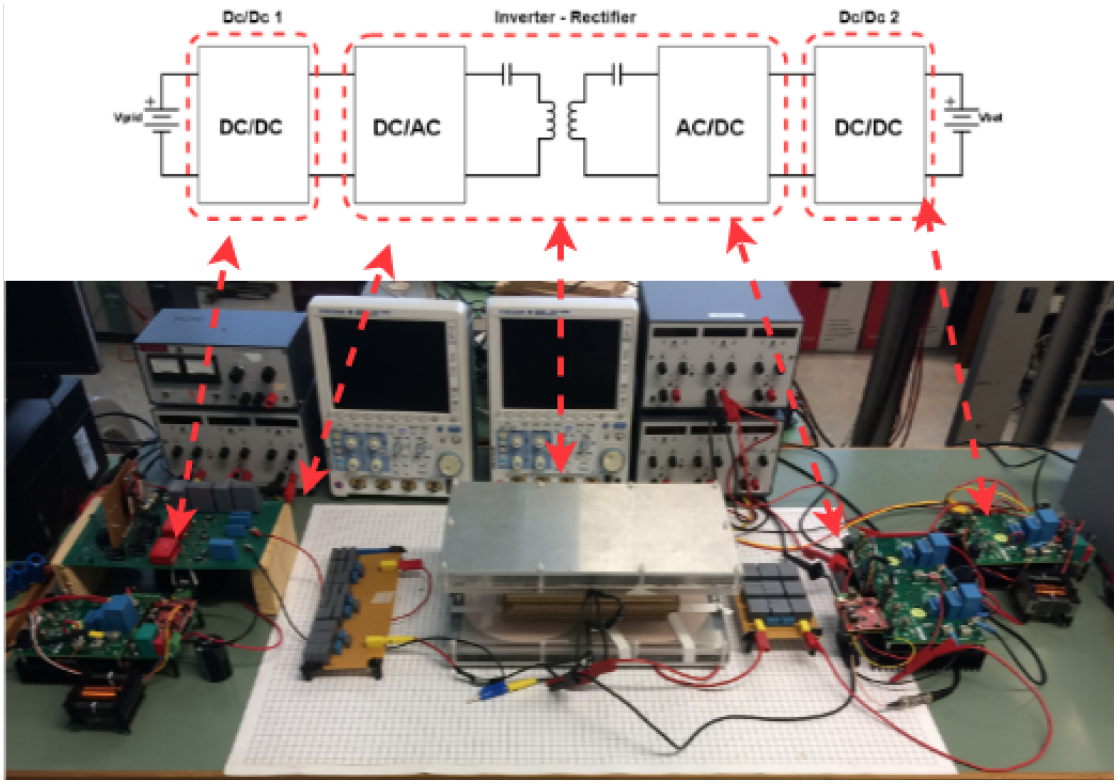

Figure 1.5.4: Picture of the setup at the end of this thesis

Table 1.5.1: Setup parameters

Symbol	Quantity	Value
V_{in}	Input Voltage	350V
V_{bat}	Battery Voltage	48V
L_P	Primary Inductance	200 μH
L_S	Secondary Inductance	200 μH
C_P	Primary Capacitance	18.9 nF
C_S	Secondary Capacitance	18.9 nF
L_1	Dc/dc 1 Inductor	2 μH
L_2	Dc/dc 2 Inductor	1 μH
C_1	Grid side DC link capacitance	300 μF
C_2	Vehicle side DC link capacitance	300 μF
C_{grid}	Grid side capacitor	15 μF
$C_{battery}$	Battery side capacitor	15 μF

CHAPTER 2

BASICS OF INDUCTIVE POWER TRANSFER

2.1 INTRODUCTION

In this chapter some of the basic principles of inductive power transfer are discussed. Starting with the electromagnetic theory behind it, on which the electric equivalent circuit of the transformer and resonant tank are based. After this an analysis of the series-series compensated resonant tank is done. Followed by an analysis of bifurcation for a series-series resonant tank

2.2 INTRODUCTION TO INDUCTIVE POWER TRANSFER

Inductive power transfer (IPT) is a way of transmitting power by means of an electromagnetic field which is transmitted and received by coils. The fundamentals which form the basics of inductive power transfer were already discovered begin 19th century by the scientists Maxwell, Ampere and Faraday (among other scientist which contributed in the field). Their discoveries are now famous and described in similarly named law's, which state:

- **Maxwell-Ampere Law** : Describes the relation between a closed loop current carying wire and the magnetic field around it. It states that if you take any closed path around a wire and sum up the magnetic field along this path, then this will equal the amount of current which is enclosed by that path. Mathematically this comes down to: is current

$$\frac{1}{\mu_0}\oint_C \mathbf{B}\cdot d\boldsymbol{l} = \iint_S \left(\mathbf{J}+\epsilon_0\frac{\delta \mathbf{E}}{\delta t}\right)\cdot d\mathbf{S} \tag{2.2.1}$$

  Here μ_0 is the permeability of free space (vacuum, but often also used for air), **B** is the magnetic flux density around the wire, $\boldsymbol{l}$ is the length over which the line integral is performed, **J** is the current density inside the wire, ϵ_0 is the permitivitty of free space, **E** is the electric field and finally **S** is the surface on which the surface integral is performed. The first term in the surface integral is the part of the magnetic field which is related due to the current, the second term is the time varying electrical field. The spatial arrangement of this can be seen in Figure 2.2.1

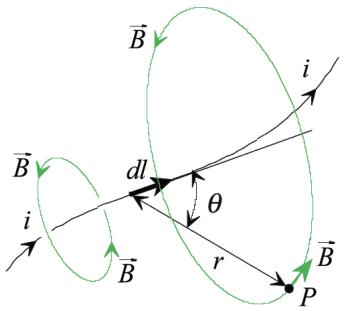

Figure 2.2.1: Magnetic flux density around a current carrying wire[4]

•**Faraday's Law** : Describes the relation between induced voltage and magnetic flux. It states that in a closed loop the rate of change of magnetic flux (enclosed by that loop) in time is equal to minus the induced voltage, also called electromotive force. This is shown in integral terms in equation 2.2.2.

$$\oint_C \mathbf{E} \cdot d\boldsymbol{l} = -n_{\text{loop}} \frac{\delta}{\delta t} \iint_S \mathbf{B} \cdot d\boldsymbol{S} \tag{2.2.2}$$

Here n is the amount turns of the loop. The first term represents the induced voltage in a wire (voltage equals electric field integrated over a distance) and the second term equals the time derivative of the magnetic flux (which is equal to the magnetic flux density integrated over a surface). An example of a magnetic field enclosed by a closed loop can be seen in Figure 2.2.2.

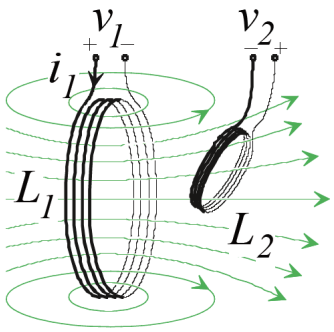

Figure 2.2.2: Voltage induced by a changing enclosed magnetic field[4]

Both of the above Law's are part of the Maxwell equation set, which form the foundation of electromagnetism. Note that the other two Maxwell equations are of course also valid but play a less significant role in inductive power transfer.

Now consider the case of two coils, a transmitter and a receiver (from now on called primary and secondary coil) which are in each other's vicinity, for example L1 and L2 of Figure 2.2.2. Then if an alternating current is flowing inside the primary coil, which induces an alternating magnetic field (Maxwell-Ampere Law), this alternating magnetic field is picked up by the receiver coil in which it induces a voltage. If the secondary coil is then closed, using a load for example, a current is induced inside this loop and power is transferred from the primary to the secondary side. This is the basic principle of IPT.

The amount of power which is then transferred is related to how well the two coils are coupled, so how much flux of L1 is picked up by L2, this is described by a parameter called the mutual inductance. Which relates the amount of voltage induced in the secondary coil to the current flowing throught the primary coil, or vice versa. This is described in equation 2.2.3 and 2.2.4

$$v_s(t) = M_{12} \frac{di_p}{dt} \tag{2.2.3}$$

or,

$$v_p(t) = M_{21} \frac{di_s}{dt} \tag{2.2.4}$$

Here $M_{12} = M_{21} = M$ [H]. The value of M is dependant on the geometry of the coils, materials used, spatial orientation, amount of turns and surrounding materials. Besides mutual inductance also self induction exists. This parameter, usually abbreviated as $L_{p,s}$ (primary/secondary inductance), describes how much magnetic field is induced by the current inside the coil and thus describes the amount of energy which is stored in a magnetic field related to the current. The self inductance is related to the same parameters as the mutual inductance. Using these two inductances the voltage equations for a two coil transformer can be written as:

$$v_p(t) = R_p I_p + L_p \frac{di_p}{dt} + M \frac{di_s}{dt} \tag{2.2.5}$$

$$v_s(t) = R_s I_s + L_s \frac{di_s}{dt} + M \frac{di_p}{dt} \tag{2.2.6}$$

Here $R_{p,s}$ are the coil resistances. Furthermore, also a third inductance exists which is called leakage inductance and is defined as the part of field which is not coupled: $L_{leakage,p} = L_p - M$. Now this theory will be used in the next section to make an electrical equivalent model of the transformer.
[4]: IPT book chapter 2

2.3 TRANSFORMER MODEL & COMPENSATION

For modeling the behaviour of a transformer an equivalent circuit is used. As always with modeling a good trade-off between model complexity and accuracy is needed. In this case the equivalent circuit shown in Figure 2.3.1 is used since the distinction between inductances and induced voltage makes the analyses very intuitive. The parasitic coil capacitances and core losses are assumed to be negligible.

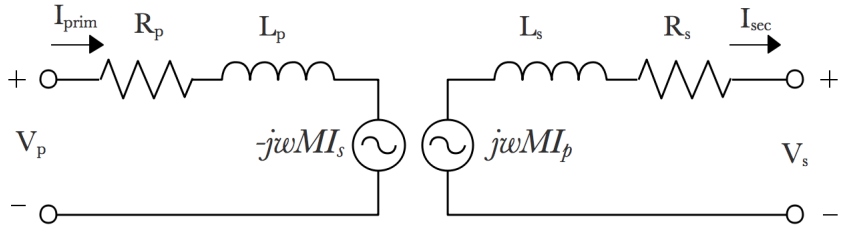

Figure 2.3.1: Transformer equivalent circuit

Here R_p and R_s are the primary and secondary coil resistance, M is the mutual inductance and L_p and L_s are the primary and secondary inductances respectively. As can be seen, in the equivalent model the mutual inductance is shown as a current dependant voltage source. In small airgap transformers this mutual inductance takes up more than 90% of the entire primary and secondary inductance. However in IPT systems the airgap between primary and secondary is often very large, resulting in a very small mutual inductance and large leakage. This high leakage inductances, induces circulating currents which do not contribute to power transfer. This creates additional losses and higher voltages are needed in order to transfer the same amount of power[3]. In order to still achieve high efficiencies, compensation capacitors are used. These capacitors compensate for the impedance of the inductances and create a resonance.
There exist multiple topologies to do this (series, parallel and combinations of these). However for a parallel compensated primary circuit a current source behaviour is needed at the input. This further complicates the system and introduces extra losses due to the extra inductor needed [4][5]. Therefor only series primary resonant circuits are considered and discussed in the next section.

2.3.1 COMPENSATION

The equivalent circuits of a series-series and series parallel compensated transformer are shown in Figure 2.3.2 (including source and load). As said, the goal of the capacitors is to compensate for the large leakage inductances, this induces an AC resonance current which creates an alternating magnetic field. In order to maximize the power transfer capability the primary and secondary resonance frequency should be equal such that the impedance seen from the source has zero phase angle, minimizing VA rating of the supply and maximizing power transfer capability [6].

$$C_{p,series} = \frac{1}{\omega_0^2 L_p} \qquad C_{p,parallel} = \frac{1}{\omega_0^2 \left(L_p - \frac{M^2}{L_s}\right)} \tag{2.3.1}$$

To achieve this the primary capacitor should be able to compensate for the primary reactance as well as the reflected secondary reactance. In [6] it is shown that a series resonant secondary has zero reflected reactance, whereas a parallel resonant secondary has a capacitive reflected reactance $\left(\frac{j\omega_0 M^2}{L_s}\right)$. Because of this the value

of the primary capacitor needed for the correct compensation is dependant on the mutual inductance for parallel resonance. This of course is not a desired characteristic for a system which should be misalignment tolerant and which should thus be at resonance for a large variety of mutual inductance. Furthermore, the series-parallel circuit is not a symmetrical system and therefor also not ideal for a bidirectional system. Because of these reasons a series-series compensated system will be used. In the next section an mathematical analysis of a series-series resonant tank is done.

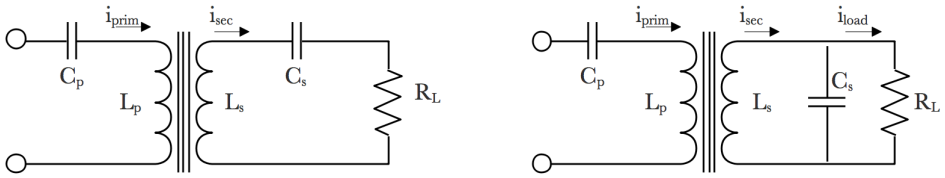

Figure 2.3.2: Series-series and Series-Parallel compensated transformer

2.4 Series Series Resonant Tank Analysis

In order to design an inductive power transfer system, first the dynamics of the resonant tank have to be investigated. To do this the equivalent circuit of the resonant tank shown in Figure 2.4.1 is analysed. Here V_p is the output of the inverter, which is a square wave and R_L is the AC equivalent load resistor modelling the rectifier and load resistance, which from [5] is known to be $\frac{8}{\pi}R_L$.

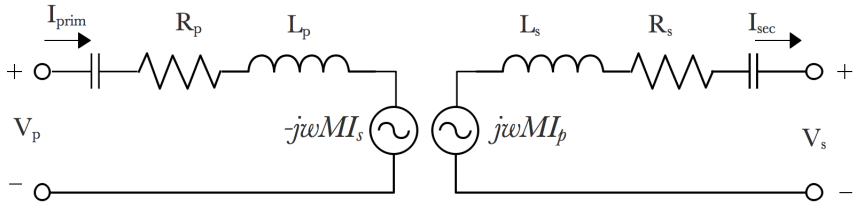

Figure 2.4.1: Series-series compensated system

In this analysis first harmonic approximation (FHA) is used. This means that all currents are assumed to be pure sinusoids, this is a reasonable assumption since in a series series resonant system power is only transferred in the first harmonic [7]. By applying Kirchoff's Law to both primary and secondary side the voltage equations can be obtained. These are given in equations (2.4.1) and (2.4.2).

$$V_p - \left(R_p + j\omega L_p + \frac{1}{j\omega C_p}\right)I_p + j\omega M I_s = 0 \tag{2.4.1}$$

$$-V_s - \left(R_s + j\omega L_s + \frac{1}{j\omega C_s}\right)I_s + j\omega M I_p = 0 \tag{2.4.2}$$

From these equations the input impedance seen by the voltage source inverter (VSI) and voltage gain can be determined. Both are good quantities to analyze the frequency behaviour of a resonant system. First the input impedance will be derived. To obtain the input impedance, the secondary side impedance is tranformed to the primary side using the reflected impedance Z_R. The input impedance is then:

$$Z_{in} = R_p + j\omega L_p + \frac{1}{j\omega C_p} + Z_R \tag{2.4.3}$$

Where,

$$Z_R = \frac{\omega^2 M^2}{(R_L + R_s) + j(\omega L_s - \frac{1}{\omega C_s})} \tag{2.4.4}$$

Then by multiplying Z_R with its complex conjugate and substituting that into equation 2.4.4, the following formula for the input impedance is obtained:

$$Z_{in} = \underbrace{R_p + \frac{\omega^2 M^2 \left(R_L + R_s\right)}{\left(R_s + R_L\right)^2 + \left(\omega L_s - \frac{1}{\omega C_s}\right)^2}}_{\mathrm{Re}(Z_{in})} + \underbrace{j\left(\omega L_p - \frac{1}{\omega C_p} - \frac{\left(\omega L_s - \frac{1}{\omega C_s}\right)\omega^2 M^2}{\left(R_L + R_s\right)^2 + \left(\omega L_s - \frac{1}{\omega C_s}\right)^2}\right)}_{\mathrm{Im}(Z_{in})} \tag{2.4.5}$$

This impedance can be split up into its input resistance $\mathrm{Re}(Z_{in})$ and input reactance $\mathrm{Im}(Z_{in})$, which describe the active and reactive power flow respectively. In order to achieve maximum power transfer it is desired to operate the system at the zero phase angle frequency, since at this frequency the phase is zero and the reactive power flow is zero. This decreases the VA rating of the components and increases the power transfer capability and efficiency. [6] Figure 2.4.2b shows the phase angle of Z_{in} for multiple load resistances and multiple coupling factors. As can be seen for resistances below 20Ω and coupling factors higher than 0.2 the phase angle shows multiple zero crossings and the system thus has multiple zero phase angle (ZPA) frequencies. This phenomena is called pole-splitting or bifurcation and will be discussed in the next section.

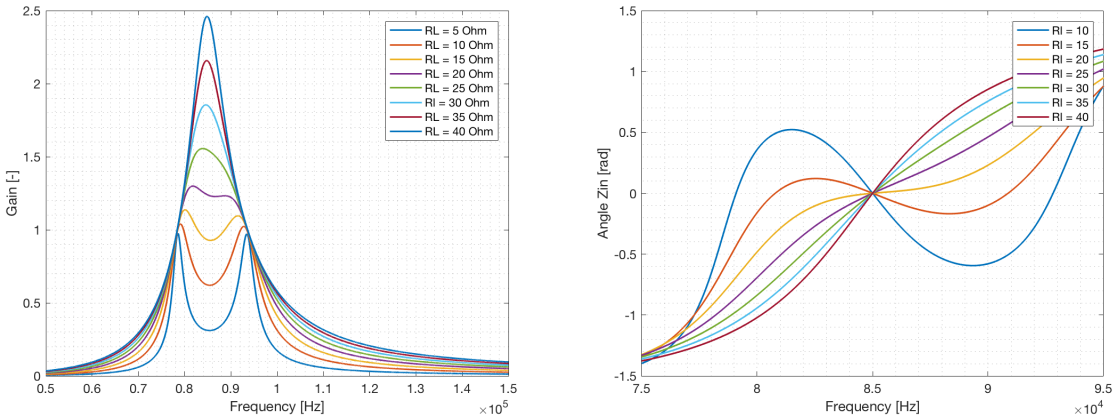

(a) Voltage gain over frequency for multiple load resitances (b) Input impedance phase

Figure 2.4.2: Individual effect of displacement in the x- and y-direction.

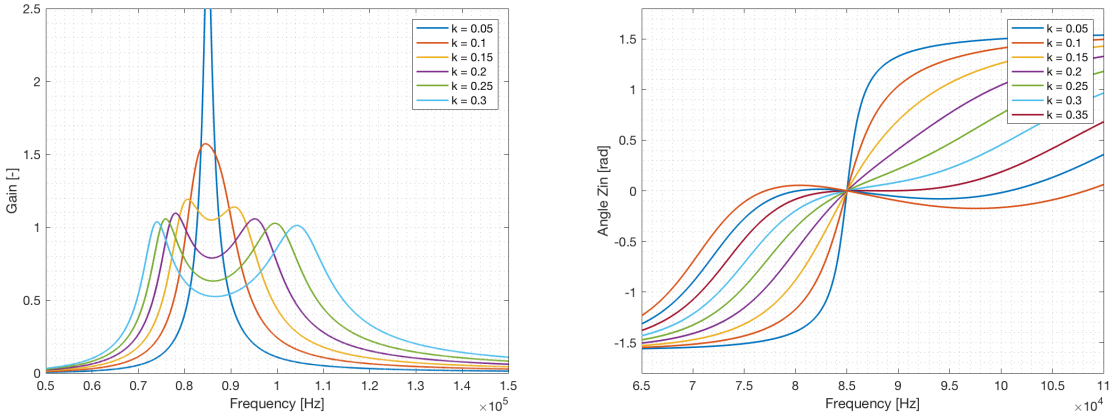

(a) Voltage gain over frequency for multiple coupling factors (b) Input impedance phase for multiple coupling factors

Figure 2.4.3: Individual effect of displacement in the x- and y-direction.

Next the voltage gain G will be determined, since the secondary side acts as a current source the output voltage equals $I_s R_L$. The voltage gain then equals:

$$G = \frac{I_s R_L}{V_p} \tag{2.4.6}$$

where,

$$V_p = Z_p I_p - j\omega M I_s \tag{2.4.7}$$

and

$$I_s = \frac{j\omega M I_p}{Z_s} \tag{2.4.8}$$

Here Z_p and Z_s are the primary and secondary side impedances which equal

$$Z_p = R_p + j\omega L_p + \frac{1}{j\omega C_p} \tag{2.4.9}$$

$$Z_s = R_s + R_L + j\omega L_s + \frac{1}{j\omega C_s} \tag{2.4.10}$$

Equations 2.3.7-2.3.10 are then substituted into equation 2.3.6 to obtain the following:

$$G = \frac{\frac{j\omega M I_p}{Z_s} R_L}{Z_p I_p - j\omega M \frac{j\omega M I_p}{Z_s}} = \frac{j\omega M R_L}{Z_p Z_s + \omega^2 M^2} \tag{2.4.11}$$

Figure 2.4.2a Shows the voltage gain for multiple load resistances, because of the current source behaviour of the secondary side a higher load resistance gives a higher output voltage. Furthermore, since there exist three zero phase angle frequencies for $R_L < 16\Omega$ wile $k = 0.15$ or for $k > 0.3$ while $R_L = 16$ there also exist three min/maxima in the voltage gain. The initial resonant frequency is now a local minimum next to which two resonant frequencies exist. This shows where the name pole splitting comes from; below a certain limit multiple real positive eigenvalues exist, while above this limit only one positive eigenvalue has a real value. This is discussed in the next section.

2.5 BIFURCATION

Pole splitting or bifurcation is defined as the phenomena where a change in parameter value, changes the stability properties of an equilibrium. In a series-series resonance tank, physically this occurs when the quality factor of the resonance tanks increases above a certain limit, such that the dynamics of both primary and secondary are reflected to each other and the system becomes a fourth order system. Given the quality factors of the primary and secondary tank shown in eq. (2.5.1) and eq. (2.5.2), it can be seen that this can occur due to an increased coupling or decreasing load resistance. Since the coupling has a quadratic effect on the quality factor while it has a linear relationship with the load resistance, the system reacts differently on a change of k or R_L. This is also seen in Figures 2.4.2 and 2.4.3.

$$Q_p = \frac{L_p(R_L + R_s)}{\omega_0 M^2} \tag{2.5.1}$$

$$Q_s = \frac{\omega_0 L_s}{R_L + R_s} \tag{2.5.2}$$

This can be seen in Figure 2.4.1, where increasing the coupling factor changes the voltage gain and resonant frequencies as it becomes a fourth order system, with multiple resonant frequencies. This can also be seen in Figure 2.4.2 and 2.4.3, where changing the load resistance bifurcates the system.

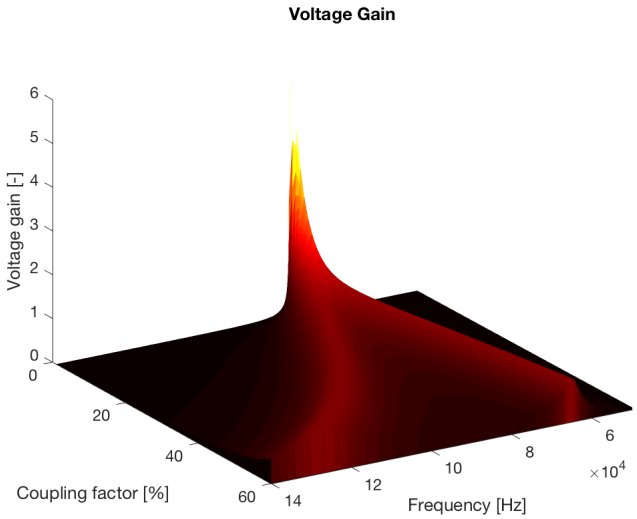

Figure 2.5.1: Pole splitting or bifurcation

Usually it is desired to avoid bifurcation, because of the reduced power transfer capability and the added complexity in control [6]. Therefor the limits of the bifurcation free operating range need to be determined. To do this the region where the input phase angle only has a single zero crossing is called the bifurcation free region, while with three zero crossings the system is bifurcated. Thus in order to find the limits at which bifurcation occurs, it needs to be determined under which conditions more than one eigenvalue has a real value. By calculating $\mathrm{Im}(\hat{Z_{in}}) = 0$ these eigenvalues can be found.
Following the procedure done by Wang et al. [6][8], first the input impedance will be normalized with respect to the reflected impedance during resonance, given in equation (2.5.4). This is then also normalized with respected to the resonance frequency, as done in equation (2.5.5).

$$\hat{Z_n} = \frac{\hat{Z_{in}}}{Z_{R0}} \tag{2.5.3}$$

where,

$$Z_{R0} = \frac{\omega_0^2 M^2}{R_s + R_L} \tag{2.5.4}$$

$$u = \frac{\omega}{\omega_0} \tag{2.5.5}$$

The result of these normalizations can be divided into a real part, $\mathrm{Re}(\hat{Z_n})$, and an imaginary part $\mathrm{Im}(\hat{Z_n})$. The results according to [4] are given in equations (2.5.6) and (2.5.7).

$$\mathrm{Re}(\hat{Z_n}) = \frac{R_p}{\mathrm{Re}(Z_{R0})} + \frac{u^4}{(u^2-1)^2 Q_2^2 + u^2} \tag{2.5.6}$$

$$\mathrm{Im}(\hat{Z_n}) = \frac{(u^2-1)[(Q_1 Q_2^2 - Q_2)u^4 + (Q_1 - 2Q_1 Q_2^2)u^2 + Q_1 Q_2]}{u(u^2-1)^2 Q_2^2 + u^3} \tag{2.5.7}$$

Here Q_p and Q_s are the primary and secondary quality factors respectively, which for a series series compensated system are defined by equation (2.5.1) and (2.5.2). It should be noted that the primary coil resistance is not incorporated in the imaginary part of the normalized impedance, and because it has no effect on bifurcation it can be left out in this analysis [8].
Next by equating (2.5.7) to zero, the ZPA frequencies can be found and also under which conditions the results have multiple real values. Solving $\mathrm{Im}(\hat{Z_n}) = 0$ for u gives 6 solutions of which 3 are negative, these are ignored since the operating frequency can not be negative. The positive solutions are given in equation (2.5.8-10).

$$u_1 = 1 \tag{2.5.8}$$

$$u_2 = \sqrt{\frac{2Q_pQ_s^2 - \sqrt{Q_p(4Q_s^3 - 4Q_pQ_s^2 + Q_p} - Q_p}{2Q_pQ_s^2 - Q_s}} \tag{2.5.9}$$

$$u_3 = \sqrt{\frac{2Q_pQ_s^2 + \sqrt{Q_p(4Q_s^3 - 4Q_pQ_s^2 + Q_p} - Q_p}{2Q_pQ_s^2 - Q_s}} \tag{2.5.10}$$

The solution $u_1 = 1$ corresponds to the original resonant frequency, since for $f = f_0$ resonance will always occur and the input phase angle will thus always be zero at this frequency. The higher order ZPA frequencies are determined by $u_{2,3}$, and for these frequencies to exist (and thus for the system to be bifurcated) these should have a real value, and the numerator and denominator of $u_{2,3}$ should thus both be positive. For the denominator this means:

$$2(Q_pQ_s^2 - Q_s) > 0 \qquad \Rightarrow \qquad Q_p > \frac{1}{Q_s} \tag{2.5.11}$$

Now, since $L_p = L_s$ and k can never be bigger than 1, this equation will always hold (for this system). Furthermore, for $u_{2,3}$ to be larger than zero the numerator should also be larger than zero:

$$num_{2,3} = 2Q_pQ_s^2 \pm \sqrt{Q_p(4Q_s^3 - 4Q_pQ_s^2 + Q_p} - Q_p > 0 \tag{2.5.12}$$

This adds the following condition for bifurcation free operation:

$$Q_1 < \frac{4Q_2^3}{4Q^2 - 1} \tag{2.5.13}$$

The limits given in eq. (2.5.11) and (2.5.13) correspond with the limits found in [6][8][9]. Plotting these limits in the Q_p-Q_s plane results in Figure 2.5.2. Here the third region shows the bifurcation free region.

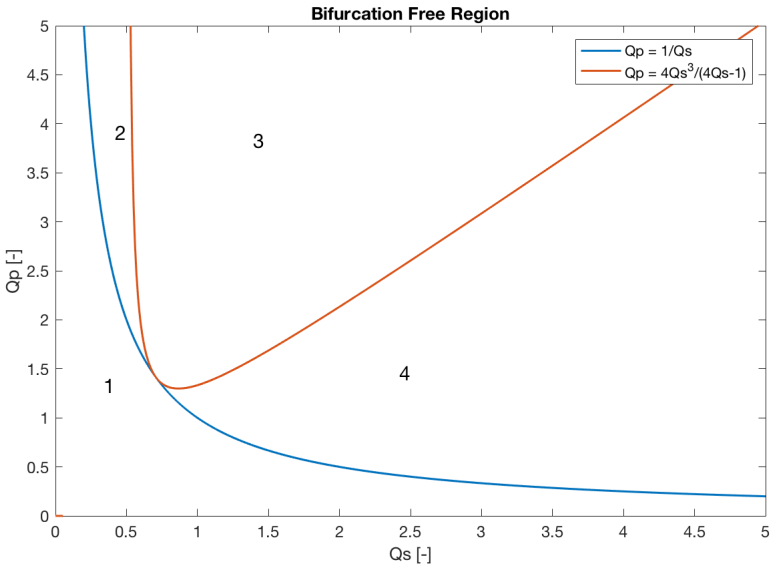

Figure 2.5.2: Bifurcation (free) region

Next the conditions stated in equations (2.5.11) and (2.5.13) should be rewritten in terms of circuit parameters and k such that practical bifurcation limits can be determined for the control system. This is done by substituting equations (2.5.1) and (2.5.2) and solving for k. This results in equation 2.5.14.

$$k = \sqrt{\frac{4\omega^2 L_s^2(R_L + R_s)^2 - (R_L + R_s)^4}{4\omega^4 L_s^3 L_p}} \tag{2.5.14}$$

Plotting this results in Figure 2.5.2. Which shows that for a decreasing coupling also the minimum output resistance for bifurcation free operation decreases.

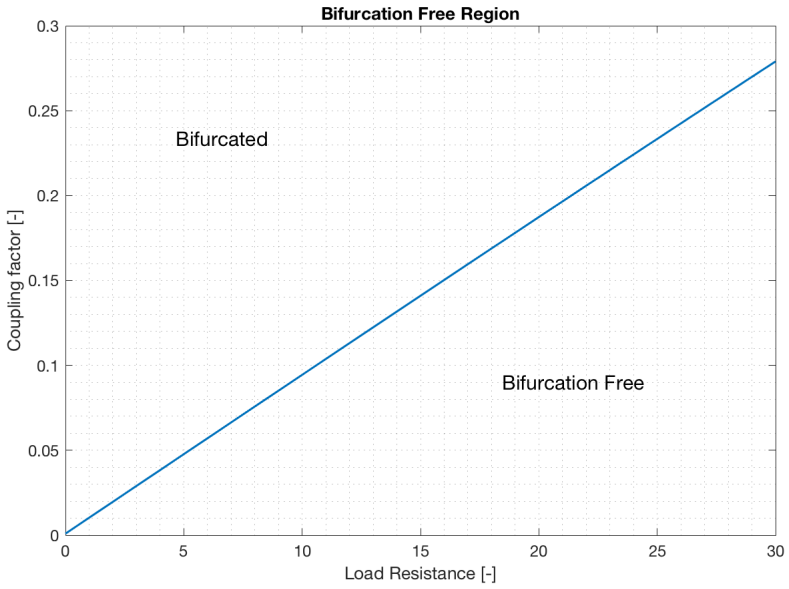

Figure 2.5.3: Bifurcation (free) region

2.6 Effect of Bifurcation On Resonant Tank

Using the Psim package in Simulink the effects of bifurcation can be simulated. This is done using the model given in Appendix A. A square wave inverter with a duty cycle of 50% was used including a passive rectifier and a resistive load. To verify the simulations the same measurements are performed on the setup as well.

The following simulations and measurements are performed:

1. First the coupling is kept constant at 0.15 while the load resistance is varied from 1Ω to 16Ω, which is just outside bifurcation region of 15Ω. The effect of decreasing the output resistance on the primary and secondary currents is investigated. This is discussed in section 2.6.1 and 2.6.2.

2. Next the effect of varying the coupling factor on primary and secondary currents is investigated. This is done while maintaining an output resistance of 16Ω. The results of this is discussed in section 2.6.3 and 2.6.4.

Effect of varying load resistance on primary current

From Figure 2.5.3 it can be seen that when the system starts to bifurcate for $R_L < 15\Omega$. The resonant frequency starts increasing, because the non bifurcated resonant frequency now corresponds to the minimum in between the two peaks shown in the voltage gain graph (Figure 2.4.2a). After performing the measurements and simulation multiple times it turns out the frequency always increases under these circumstances. The reason for this is not found in literature, but might be due to the energy stored in the transformer (eq. (2.6.1) and the reflected impedance eq. (2.6.2).

$$W_{trans} = \frac{1}{2}L_1 I_1^2 + M_{12} I_1 I_2 + \frac{1}{2}L_2 I_2^2 \tag{2.6.1}$$

$$Z_R 0 = \frac{\omega_0^2 M^2}{R_s + R_L} \qquad for \qquad f = f_0 \tag{2.6.2}$$

The reflected impedance increases quadractically with frequency, therefor at higher frequencies the loading effect of the transformer on the primary side increases, this decreases the voltage gain of the system and

causes the primary current to decrease. Which in turn decreases the energy stored in the magnetic field. Therefore a possible explanation for why the frequency is increasing instead of decreasing might be that the magnetic field has the tendency to reduce the amount energy stored in it, by increasing its frequency. However, literature does not treat this subject and therefore this can not be said with absolute certainty.

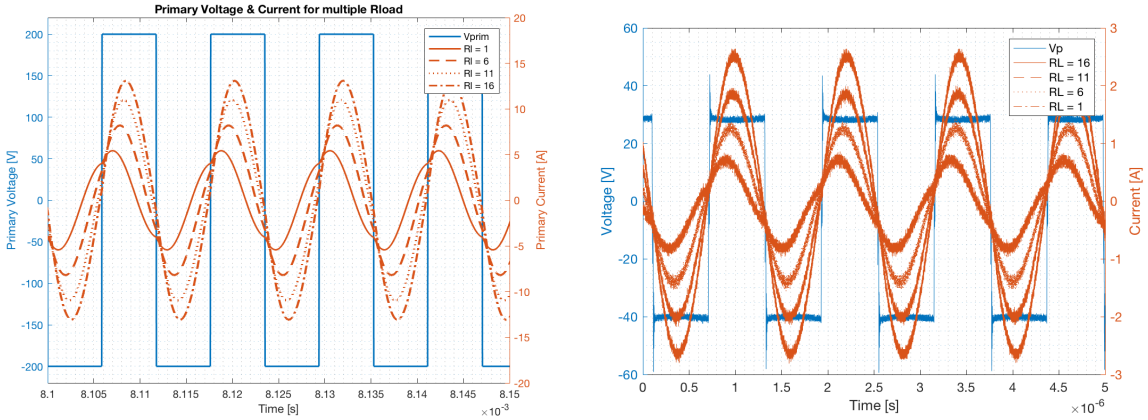

(a) Simulation

(b) Experimental

Figure 2.6.1: Effect of varying load resistance on primary current

Effect of varying load resistance on secondary current

Figure 2.6.2 shows the effect of changing R_L on the secondary current. Since the secondary side acts as a current source and because the secondary quality factor is high (in between 6.6 and 106 for $1 < R_L < 16$), the dampening effect of the load resistor on the resonant tank is fairly small (<5%). Furthermore, because of this current source characteristic and since the secondary side is only loaded by an AC equivalent resistance (compared to a reflected impedance for the primary side) there is no change in resonant frequency as well. This difference in frequency between primary and secondary is causing the reduced voltage gain when the system is bifurcated, since they don't share the same fundamental harmonic which is the only harmonic which transfers power in a series-series resonant tank.

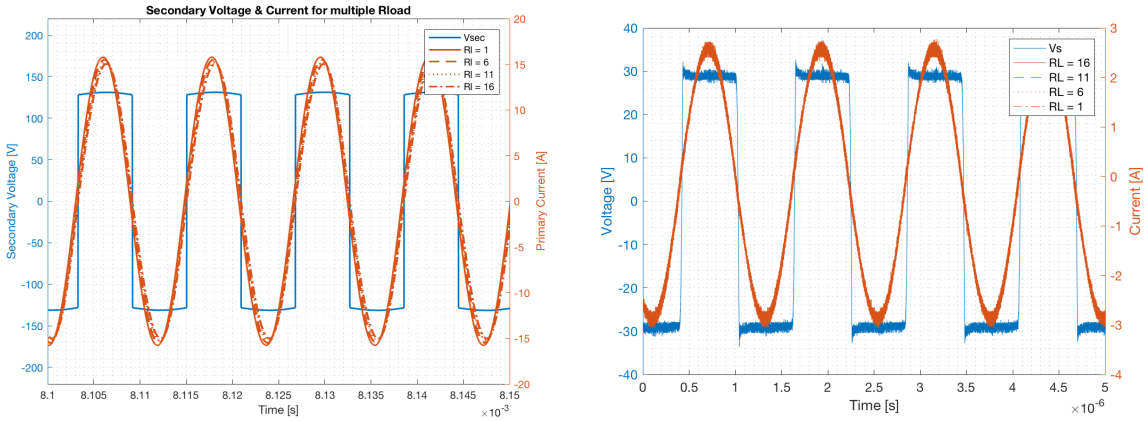

(a) Simulation

(b) Experimental

Figure 2.6.2: Effect of varying load resistance on secondary current

Effect of varying coupling factor on primary current

Besides changing the load resistance, bifurcation can also occur when the coupling is increased. The output resistance is now kept constant at 16Ω and the coupling factor is increased from 0.1 to 0.4. For this resistance

bifurcation occurs for a coupling factor of 0.16-0.17 or higher. As Figure 2.5.4. shows the resonant frequency increases as the system starts to bifurcate. Furthermore the amplitude decreases since the loading effect on the transformer increases for higher coupling factors.

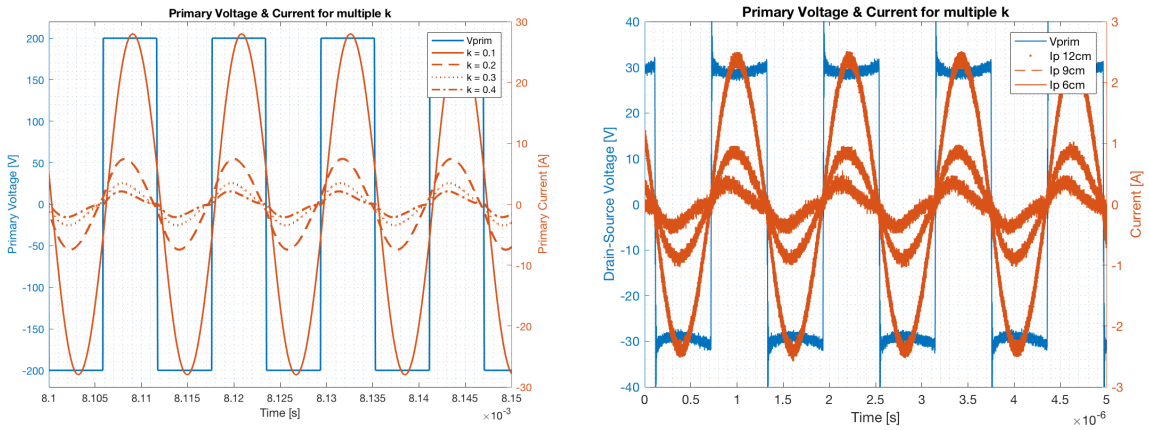

(a) Simulation

(b) Experimental

Figure 2.6.3: Effect of varying the coupling on primary current

Effect of varying coupling factor on secondary current

Finally the effect of varying the coupling factor on the secondary side is shown in Figure 2.6.4. Note that the secondary voltage is only plotted once, for k = 0.1. In contrast to varying the output resistance, changing the coupling does have an effect on the secondary side. This is because the voltage induced in the secondary equals $V_{ind,sec} = j\omega M I_p$ and is thus dependant on the coupling. Again the resonant frequency increases and the amplitude decreases, since the primary current also decreases. However, due to the increased coupling, the decrease in amplitude of the secondary is less than the decrease of primary current.

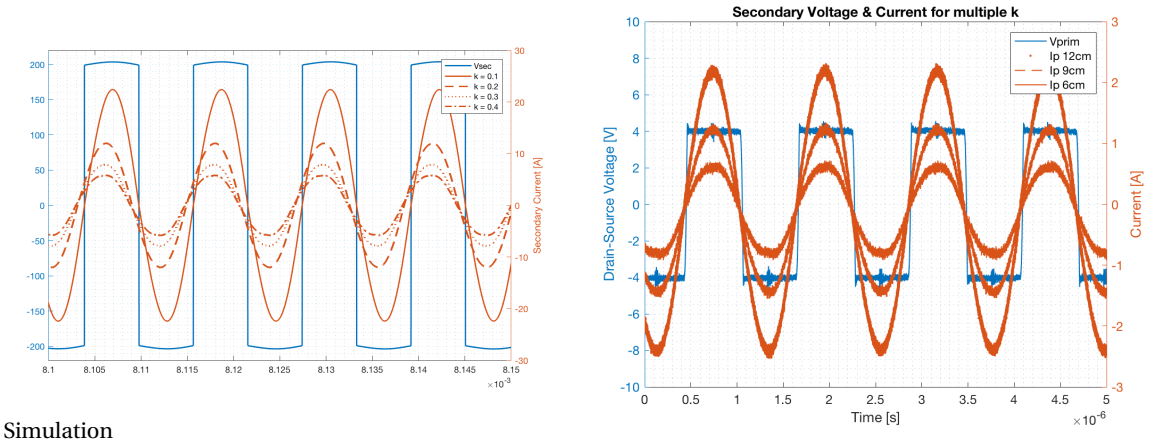

(a) Simulation

(b) Experimental

Figure 2.6.4: Effect of varying the coupling on secondary current

To summarize

Overall, bifurcation leads to an increase in resonant frequency and a reduced gain. However the reduced gain is also due to other effects, such as an increased in input impedance which comes along with e.g. an increasing coupling factor. An overview of the cause and effects of bifurcation are given in Table 2.6.1

Table 2.6.1: Summary bifurcation dependance on k and R_L

	Effect on Bifurcation		Remarks
	Primary current	Secondary current	
R_L	Increase in frequency and decrease in amplitude	negligible	The reduction in primary amplitude is due to the increased amplitude of the input impedance. This however can not be tested seperately without bifurcation occuring.
k	Increase in frequency and decrease in amplitude	Small increase in frequency and decrease in amplitude	Amplitude of primary current changes due to loading effect on transformer Secondary amplitude decreases due to decrease in the induced voltage

2.7 CONCLUSION

In this chapter Maxwell-Ampere Law and Faraday's law were used to set up an electrical equivalent circuit of a transformer. Then the need for compensation capacitors in inductive power transfer is discussed followed by the best compensation topology for a misalignment tolerant control scheme. The resulting series series resonant tank is then analyzed and the bifurcation phenomena is seen under certain values of resonant tank quality factor. Since bifurcation adds complexity and reduces transfer efficiency, the bifurcation limit and bifurcation effects were analyzed such that this can be taken into account later when the control system is designed. In order to design the control system, a review of the most common control methods for inductive power transfer is discussed in the next chapter. From this chapter the best power control method will be derived for the proposed control scheme.

CHAPTER 3

CONTROL METHODS FOR INDUCTIVE POWER TRANSFER

3.1 INTRODUCTION

Before a new control scheme can be proposed, first a review of existing control methods should be done in order to investigate the best most suitable solution for a bidirectional misalignment tolerant control scheme. Therefore in this chapter a review of the most common methods for controlling the output power in IPT systems is given. For static IPT systems, control strategies can be divided into four categories

1. Variable frequency control
2. Fixed Frequency control
3. Dual Control
4. Voltage Control.

For each type of control an example will be explained and compared using simulations in simulink, the model and parameters used for this are given in Appendix A. In this analysis the MOSFETs were replaced by ideal switches, such that gatedrivers could be avoided and the random access memory (RAM) needed to perform the simulations could be held within the limits of the computers. However, because of this switching losses could not be taken into account in the analysis.

3.2 VARIABLE FREQUENCY CONTROL

One of the most earliest methods for controlling the output power in resonant converters is frequency control. Here the duty cycle of the inverter is kept at 50% while the switching frequency is controlled around the resonant frequency, such that it operates in the inductive ($f > f_0$) or capacitive region ($f < f_0$). However usually the system is operated in the inductive region, such that ZVS is possible. By changing the frequency the magnitude of the input impedance $|Z_{in}|$ is increased and thus the primary current and power is decreased [10]. The change of input impedance over frequency can be seen in Figure 3.2.1.
The advantage of this method is its low component count. A mayor downside of this control scheme is that the output power can only be regulated by introducing reactive power, which in turn creates additional losses due to the circulating currents it induces. This control method is also very sensitive to load and coupling variations, because if the system bifurcates the input impedance characteristic changes, as shown in Figure 3.1.1. Therefore, if the system should be able to handle large load and coupling variations, it should only be operated above the third ZPA frequency [11] which results in high values of $|Z_{in}|$.
Now, using the simulink model shown in Appendix A. the efficiency of the system is analyzed at 250W, 500W and 925W. The parameters are are chosen in such a way that bifurcation does not occur, see appendix A. Figures 3.2.2-4 show the result of switching at 92, 94 and 96kHz. From this it can be seen that the relative losses in the primary capacitor and inductor increase for a decreasing load. This is due to the increase of reactive power flowing throught the primary as a result of the increasing input impedance.

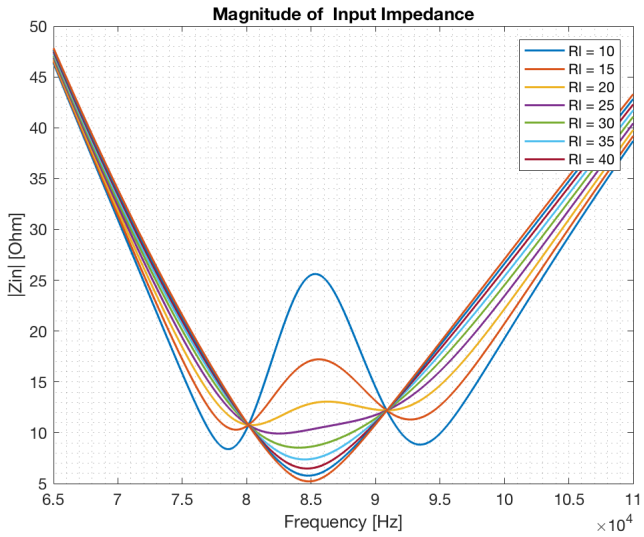

Figure 3.2.1: Magnitude of input impedance over frequency

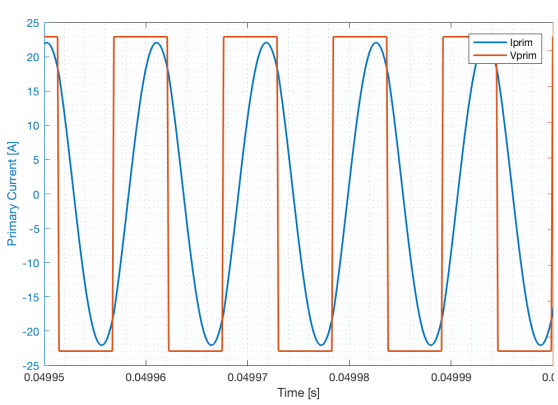

(a) Primary voltage and current at 92kHz

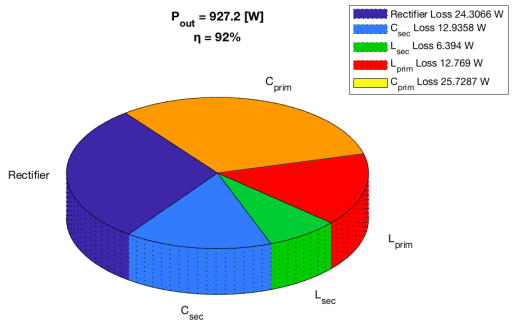

(b) System losses at around 900W

Figure 3.2.2: Losses at 92 kHz

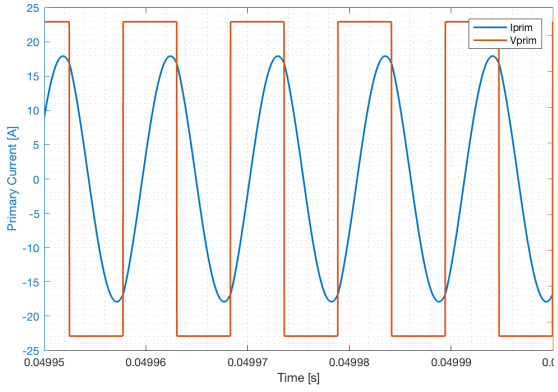

(a) Primary voltage and current at 94kHz

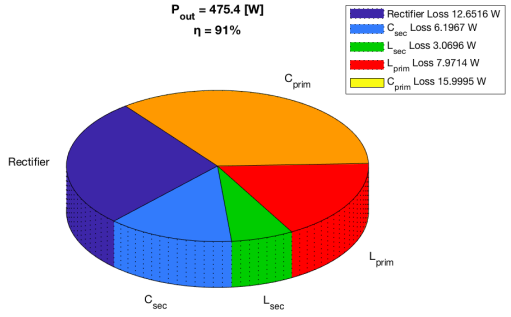

(b) System losses at 475W

Figure 3.2.3: Losses at 94 kHz

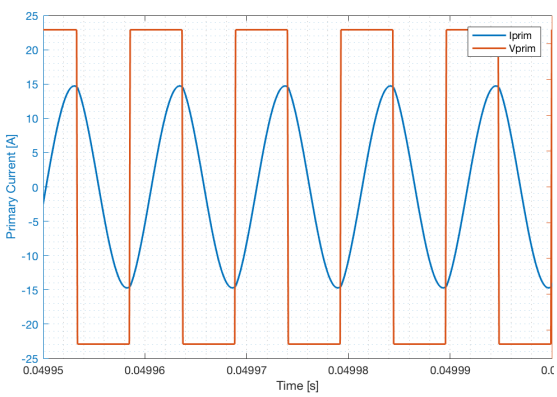

(a) Primary voltage and current at 96kHz

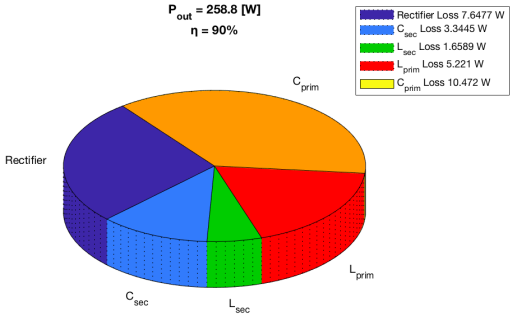

(b) System losses at 258W

Figure 3.2.4: Losses at 96 kHz

3.3 Fixed Frequency Control

Besides variable frequency control it is also possible to control the power with a fixed frequency, the advantage of this is better electromagnetic interference (EMI) performance, since the noise spectrum is less wide, so the needed filters can be more efficient and easier to design [12][13]. Now that the frequency is fixed, the power can be controlled by varying the pulsewidth or dutycycle of the inverter. Multiple modulation techniques exist but the most common one, phase shift modulation, will be discussed.

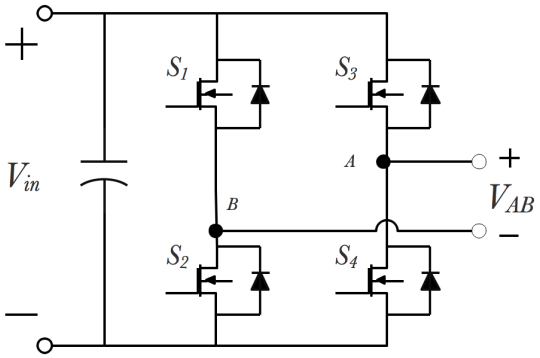

(a) Switches $S_{1,4}$ in a full bridge

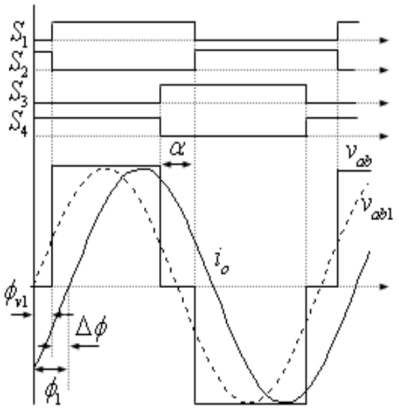

(b) Phase Shift modulation [7]

Figure 3.3.1: Phase shift modulation

Phase shift modulation (PSM) also known as the voltage cancellation method [3] or clammed mode control [13], is a control scheme where the angle between the inverter legs is modulated such that the bridge output voltage has a varying pulse width. This is shown in Figure 3.3.1. The amplitude of the fundamental component of the voltage V_{ab} is then controlled by the amount overlap between the inverter legs, see equation 3.3.1 [14]. Therefor by controlling this angle, the power can be controlled.

$$\hat{V}_{ab1} = \frac{4V_{in}}{\pi} cos(\alpha/2) \tag{3.3.1}$$

Here V_{in} is the DC input voltage of the inverter and α is the overlap angle between the inverter legs. As said above the advantage of a fixed frequency is narrower noise spectrum. Furthermore, soft switching is possible in this control scheme during turn on, if the frequency is above the resonant frequency. Since then the current is lagging the voltage and therefor the body diodes will carry the current before the switch is turned

on, such that the switch can turn on with zero voltage. During turn off, the switches are switched with losses since they are carrying a current at the moment of turn off. See Figure 3.3.1.
If the switching frequency is below the resonant frequency and the current is leading the voltage, soft switching can not occur because during turn on the current is not equal to zero, and during the turn off the current is already negative (leading current), the body diodes can not take over the current and the switches are switched off hard. Because of this the operating frequency is often chosen to be in the inductive region, however for ZVS under all load conditions the frequency should be substanstially above the resonant frequency, which again induces circulating currents and therefor always a trade off between zero voltage turn on and reactive power has to be made.
Figures 3.3.2-4 show the results of the simulations using phase shift modulation. Eventhough the switching losses could not have been taken into account, the switching frequency has been chosen to be 93 kHz so that soft switching would occur at all values of load resistance. Comparing the efficiencies with frequency control it is clear that at lower powers this control method gives better results (+ 1%). This is because there is less circulating current in the primary. Furthermore, almost all losses are decreasing with respect to the load (the relative amount stays the same), except for the rectifier which relative loss increases for lower loads due to the fixed forward voltage of the diode.

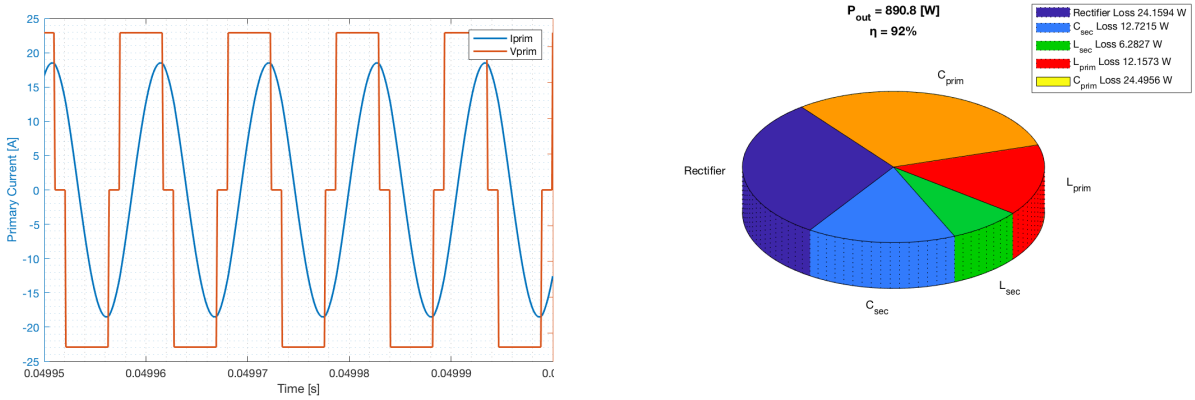

(a) Primary voltage and current using PSC at 890W (b) System losses at 890W

Figure 3.3.2: Phase shift modulation at 890W

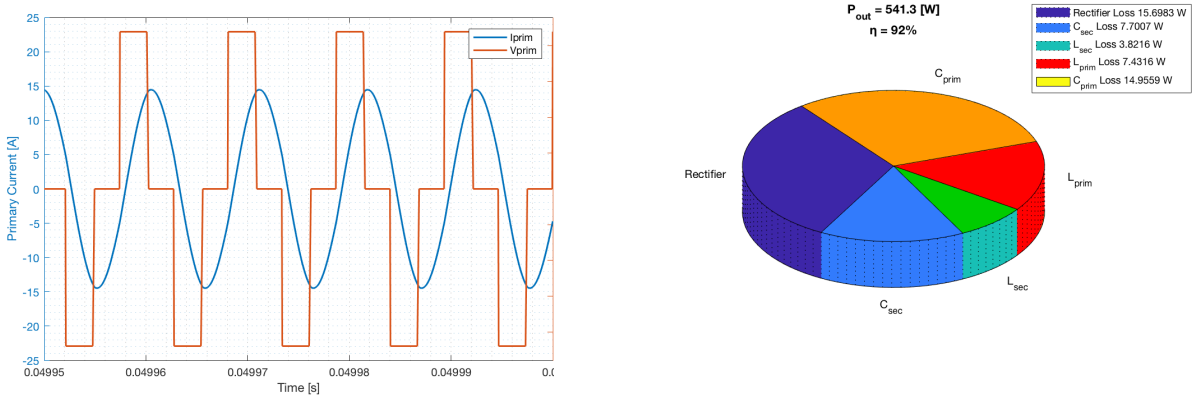

(a) Primary voltage and current using PSC at 500W (b) System losses at 500W

Figure 3.3.3: Phase shift modulation at 500W

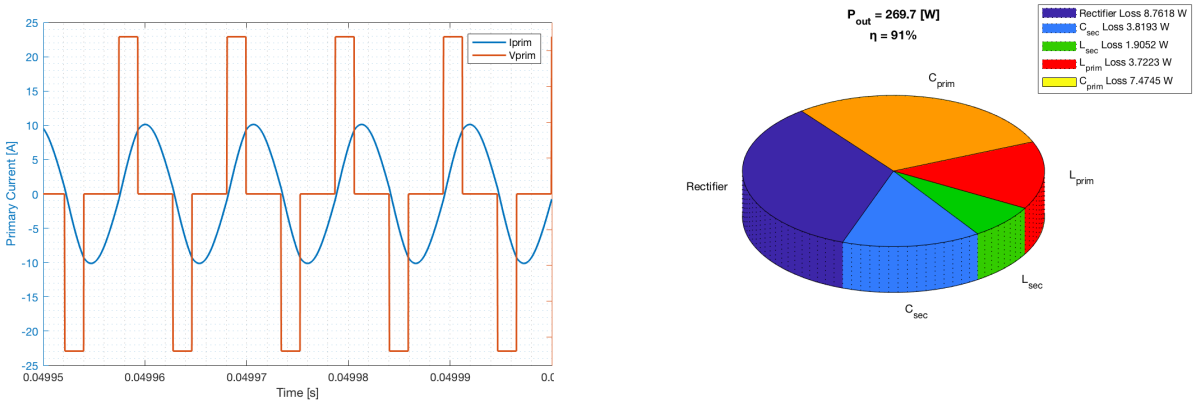

(a) Primary voltage and current using PSC at 250W

(b) System losses at 250W

Figure 3.3.4: Phase shift modulation at 250W

Other fixed frequency control methods include Asymmetrical Duty Cycle Control (ADCC) and Asymmetrical Clammed Mode Control (ACMC). Figure 3.3.2 shows the waveforms belonging to these control schemes. With ADCC the duty cycle is varied per inverter leg while the phase shift is kept at 90°. With ACMC the phase shift is also kept constant, while the duty cycle of only one inverter bridge leg is modulated. The advantage of this is that the switching frequency can be kept constant at the resonant frequency, while still maintaining ZVS during turn on for all powers[13][14]. Besides soft switching this also results in higher power transfer capabilities/no circulating currents and thus higher efficiencies.

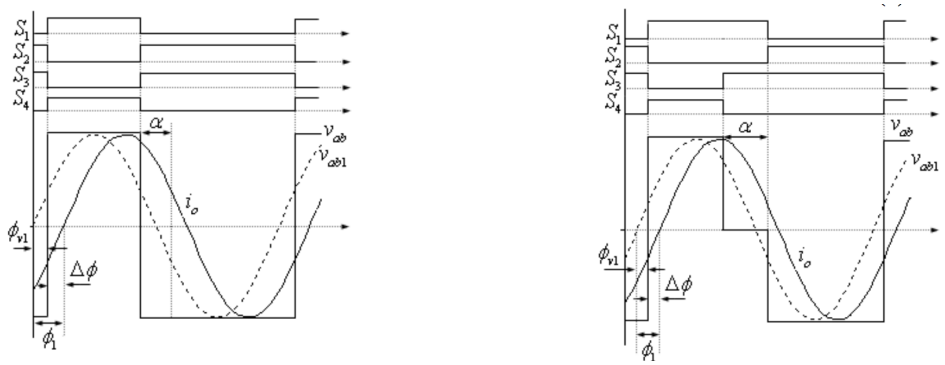

(a) Asymmetrical duty cycle control [7]

(b) Asymmetrical clammed mode control [7]

Figure 3.3.5: ADCC and ACMC waveforms.

3.4 Dual Control

As the name suggest, dual control is a combination of two methods: a fixed frequency control method while also controlling the frequency such that the system is always tracking the resonant current. The advantage of this is that the frequency does not has to be fixed at a frequency far above the resonance frequency in order for soft switching to occur. This results in better efficiencies at higher loads since the frequency can be closer to the resonance frequency and also decreases the VA rating of the components needed [10][15]. Furthermore, deviations in resonant frequency caused by temperature drift or component tolerances are always accounted for. The disadvantage of this method is that it adds components en complexity to the circuit, since a circuit for tracking the resonance is needed.
In this case the simulation results do not show any variation with PSM, this is because the switching losses were not taken into account. Besides this a small improve in efficiency may be because of the fact that the frequency is closer to the resonant frequency.

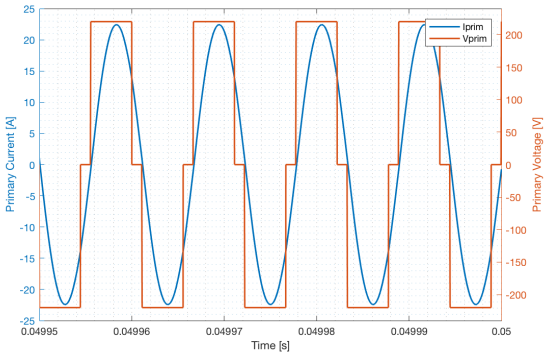

(a) Primary voltage and current using dual control at 939W

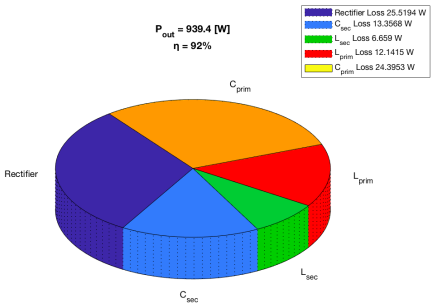

(b) System losses at 939W

Figure 3.4.1: Dual control at 939W

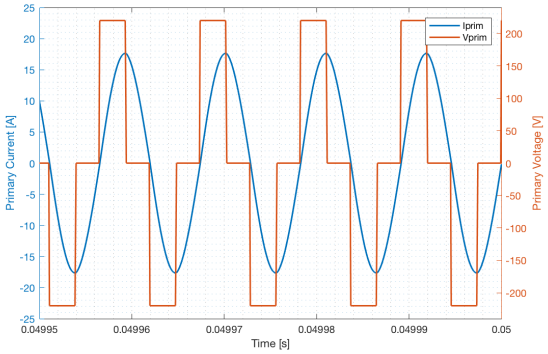

(a) Primary voltage and current using dual control at 500W

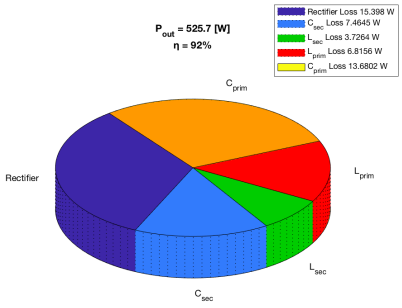

(b) System losses at 500W

Figure 3.4.2: Dual control at 526W

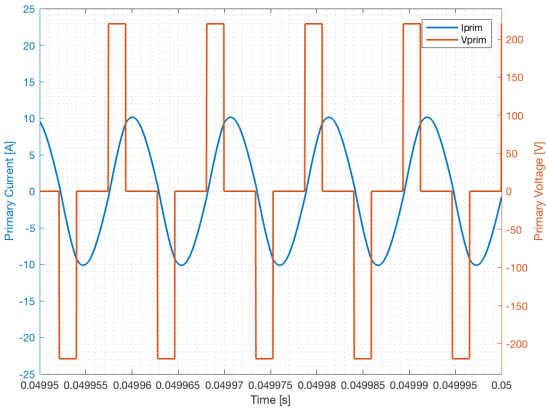

(a) Primary voltage and current using dual control at 250W

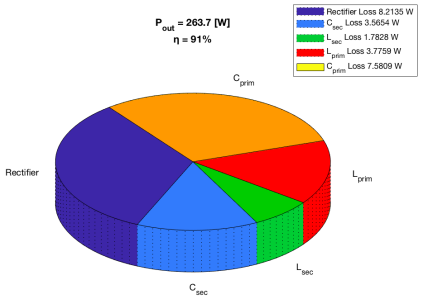

(b) System losses at 250W

Figure 3.4.3: Dual control at 263W

3.5 Voltage Control

The final method which will be discussed here is voltage control. Here the power is controlled by controlling the input voltage of the inverter. The inverter duty cycle is then kept at 50% and the frequency can be kept constant or a dual form can be made if resonance tracking is also performed. The advantage of this method is that ZVS can occur at both turn on and turn off switching instants since the duty cycle is kept at 50% and the frequency just above resonance. This also optimizes the power transfer capability of the resonance tank and because of this the VA rating of the components is also kept minimal.
The disadvantage of this method is that an additional dc/dc converter is needed to control the input voltage. This introduces additional losses and reduces the power density of the whole system. Therefor for this system to be beneficial compared to the above methods the dc/dc converter should have an efficiency as shown in equation (3.5.1) [15].

$$\eta_{dc/dc} \geqslant \frac{\max[\eta_{FC}, \eta_{FFC}, \eta_{DC}]}{\eta_{VC}} \tag{3.5.1}$$

Here FC stands for frequency control, FFC stands for fixed frequency control (any method), DC stands for dual control and VC stands for voltage control. The simulink model to simulate the voltage control method is shown in Appendix B. The results show that voltage control gives the best results, since the system can operate at the resonant frequency. As can be seen from figures 3.5.1a-3a this results in lower values of primary current.However the switching losses were not taken into account and therefor the efficiency will be a bit less in an actual situation.

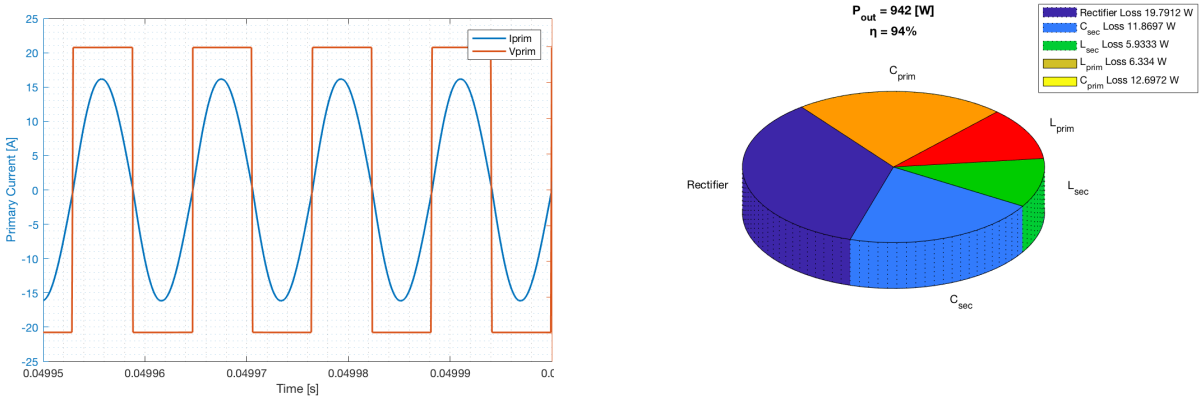

(a) Primary voltage and current using dual control at 939W (b) System losses at 939W

Figure 3.5.1: Dual control at 939W

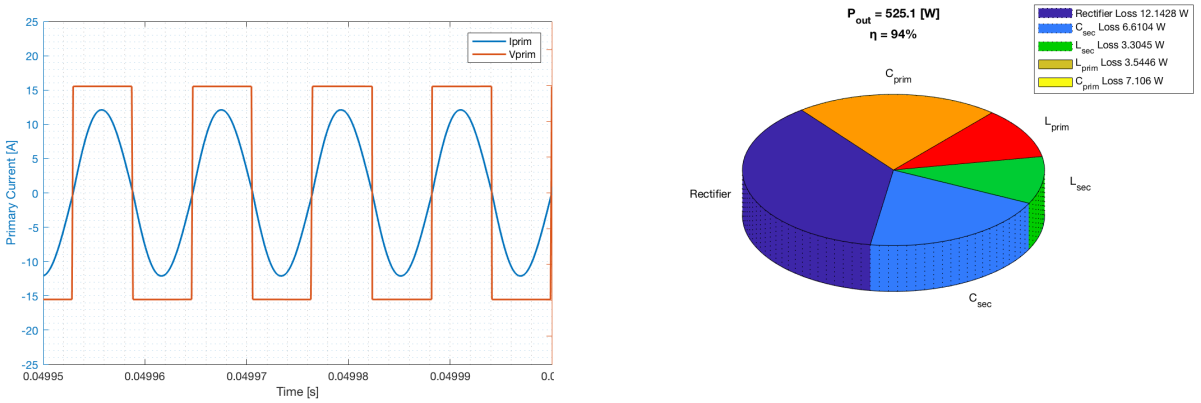

(a) Primary voltage and current using dual control at 500W (b) System losses at 500W

Figure 3.5.2: Dual control at 526W

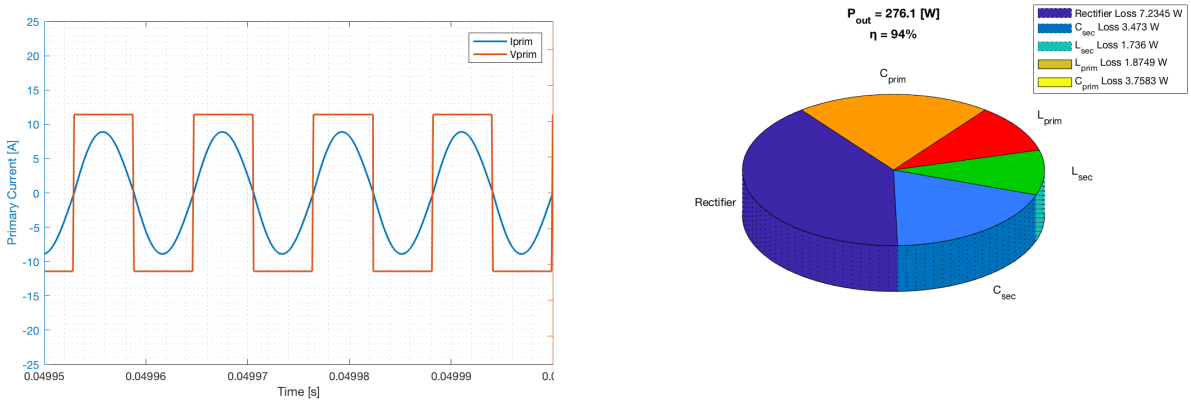

(a) Primary voltage and current using dual control at 250W (b) System losses at 250W

Figure 3.5.3: Dual control at 263W

3.6 Conclusion

From the above analyses it could be seen that best control method for controlling the output power, is the voltage control method. The reason for this is that the system can operate at exactly the resonant frequency and thus does not have circulating currents inside and therefore maximum power transfer efficiency can be achieved. Furthermore, the inverter switching losses are reduce compared to other methods since now soft switching can occur at both turn on and turn off, compared to only turn on using other control strategies. The drawback of this method is that it comes at the cost of an additional dc/dc converter in front of the inverter which creates additional losses. However, such a dc/dc converter is often already needed between the rectifier and battery (in order convert the rectifier output voltage to the battery voltage) and since the system will be designed for bidirectional power flow, this dc/dc converter is already needed for when the vehicle is delivering power to the DC grid. Because of this the voltage control method is the best method for power control in a bidirectional system. Now that the power control scheme is determined, the next step is to determine how the system can be controlled such that the coils can be misaligned while maintaining the maximum power transfer efficiency. This will be discussed in the next chapter.

CHAPTER 4

PROPOSED MISALIGNMENT TOLERANT CONTROL SCHEME

4.1 INTRODUCTION

In practical situations the vehicle coil will often not be fully alligned with the stationary coil. This reduces the coupling which decreases the efficiency of the system. Therefor it is desired to have a system which can achieve the maximum achievable transfer efficiency also when the primary and secondary coils are misaligned. In this chapter an analysis on the effect of coupling on efficiency is done, after which a control scheme is discussed such that maximum power transfer efficiency is always maintained. This includes methods for coupling factor estimation and resonance tracking.

4.2 MAXIMUM EFFICIENCY POINT TRACKING

Lets consider the series-series compensated system, such as the one shown in Figure 4.2.1. Here R_p and R_s are non linear series resistances, representing transformer core losses, ohmic losses and eddy current losses in the shielding and ESR of the capacitors. Using FEM these are determined to be around 0.5Ω [16]. However, actually these are non linear depending on the current (since the core losses depent exponentially on the fluxdensity/current) But for now these are assumed to be constant. Furthermore, R_L is an equivalent AC resistor, modeling the rectifier and load after the system and V_P is a square wave voltage similar to the output of a full-bridge inverter.

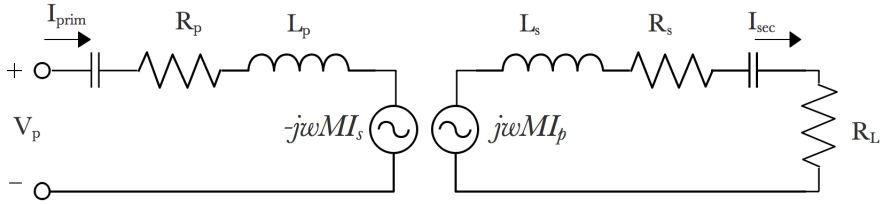

Figure 4.2.1: Series-series compensated system

Next the circuit is considered to be in full resonance, thus when the compensating capacitors cancel the total inductance of the coils and thus $f_0 = \frac{1}{2\pi\sqrt{C_p L_p}} = \frac{1}{2\pi\sqrt{C_s L_s}}$. This means both primary and secondary capacitance and inductance can be neglected. The resulting voltage equations are then given in equation (4.2.1).

$$\begin{bmatrix} V_p \\ V_s \end{bmatrix} = \begin{bmatrix} R_p & -j\omega_0 M \\ j\omega_0 M & -(R_s + R_L) \end{bmatrix} \begin{bmatrix} I_p \\ I_s \end{bmatrix} \tag{4.2.1}$$

Using equation (4.2.1) the voltage and current ratio's A_V and A_I can be determined[17]:

$$A_V = \frac{V_s}{V_p} = \frac{\omega_0 M R_L}{R_p(R_s + R_L) + (\omega_0 M)^2} \tag{4.2.2}$$

$$A_I = \frac{I_s}{I_p} = \frac{\omega_0 M}{R_s + R_L} \tag{4.2.3}$$

The inductive link transfer efficiency η_{link} is then equal to the product of these two.

$$\eta_{link} = A_V A_I = \frac{(\omega_0 M)^2 R_L}{(R_s + R_L)(R_p(R_s + R_L) + (\omega_0 M)^2} \tag{4.2.4}$$

From this equation it can be seen that the coupling and the load have a direct effect on the efficiency of the link. Since for a changing mutual inductance (in resonant operation), the impedance of the transformer changing, which changes the impedance ratio between the load and transformer. Therefore the amount of power transferred to the load can be changed by changing the coupling, as well as changing the load resistance. This is known as the maximum power transfer theorem and is part of basic circuit/thevenin theory, which states that in a thevenin equivalent circuit (such as the one given in figure 4.2.2) maximum power is transferred when the load resistor equals the thevenin equivalent resistor.

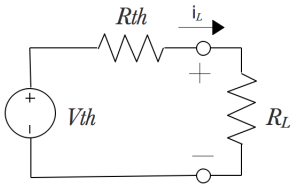

Figure 4.2.2: Thevenin equivalent circuit

The same thing holds for the equivalent circuit of Figure 4.2.1, maximum power is transferred when the equivalent load resistor R_L equals the impedance of the receiver side [18], :

$$\omega_0 M + R_s = R_{L,eq}, \quad \text{for} \quad f = f_0 \tag{4.2.5}$$

The same result is obtained when equation (4.1.3) is differentiated with respect the R_L, this results in:

$$R_{L,\eta_{max}} = \sqrt{R_s\left(\frac{(\omega_0 M)^2}{R_p} + R_s\right)} \tag{4.2.6}$$

Which for a symmetrical system, where $R_s = R_p$, results in the same as equation 4.1.5. This effect is also seen in Figure 4.2.3. It can be clearly seen that for different coupling the load resistance needed to accomplish maximum transfer efficiency differs as well. The effect of changing the load resistance on the efficiency of the inductive link is shown in Figure 4.1.3. Here it can be seen that the load resistance to obtain maximum inductive link efficiency changes when the coupling changes.

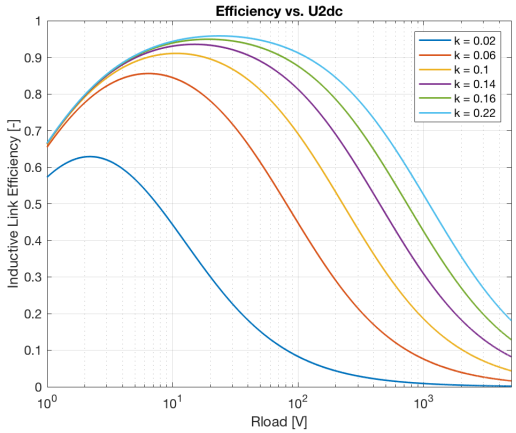

Figure 4.2.3: Effect of changing R_{load} with respect to the transfer efficiency

Therefor in order to make a system which performs maximum efficiency point tracking (MEPT), it is thus needed to have system which can vary the equivalent load resistor seen by the transformer. In the setup this equivalent load resistor equals the rectifier and the load resistor, then from [18] it is known that

$$R_{L,eq} = \frac{8}{\pi^2 \eta_{rect}} R_L = \frac{8}{\pi^2} \frac{U_2^2}{P_2} \tag{4.2.7}$$

Here η_{rect} is the efficiency of the rectifier, R_L is the load resistance U_2 is the rectifier output voltage and P_2 is the rectifier output power. From this it is clear that by regulating the rectifier output voltage MEPT can be done. By equating equation (4.2.5) and (4.2.7), the voltage needed for maximum power point tracking can be derived as shown in equation (4.2.8) and (4.2.9). The control of this voltage is done using a dc/dc converter in between the rectifier and the load. Often this converter is already needed to convert the output voltage of the rectifier to the desired battery voltage, therefor it does not introduce additional losses.

$$\begin{aligned} \omega_0 M + R_s = R_{L,eq} = \frac{8}{\pi^2} \frac{U_{2,dc}^2}{P_2} \\ \Rightarrow U_{2,dc} = \sqrt{\frac{\pi^2 \eta_{rect}}{8} \Big(\omega_0 M + R_s\Big) P_2} \end{aligned} \tag{4.2.8}$$

or in terms of coupling factor and output power:

$$U_{2,dc} = \sqrt{\frac{\pi^2 \eta_{rect}}{8} \Big(\omega_0 k \sqrt{L_p L_s} + R_s\Big) \frac{P_{out}}{\eta_{dc/dc}}} \tag{4.2.9}$$

Here $\eta_{dc/dc}$ is the efficiency of the secondary side dc/dc converter and k is the coupling factor. From this it is thus clear that once the output power setpoint, the mutual inductance and the losses in the rectifier and dc/dc converter, the MEPT voltage can be calculated. For the efficiencies an estimate based on the power setpoint can be used. The calculation of these losses is done in Appendix G. This principal will be verified in the experimental validation section at the end of this chapter. Since the MEPT control scheme affects the equivalent resistor seen by the secondary resonant tank, its effect on bifurcation should be investigated. This is done in the next section.

4.2.1 MEPT AND BIFURCATION

From the previous chapter it is known that bifurcation needs to be avoided since it degrades power transfer capability and efficiency and also complicates the control of the system. Therefor in order to check whether the MEPT control strategy interferes with the bifurcation limit, equation (4.2.5) is rewritten to single out k, such that:

$$k = \frac{R_L - R_s}{\omega_0 L_s} \tag{4.2.10}$$

This is then compared with the bifurcation boundary, given by eq. (2.5.14). This results in Figure 4.2.4. and it shows that bifurcation is always avoided when the maximum efficiency point is tracked.

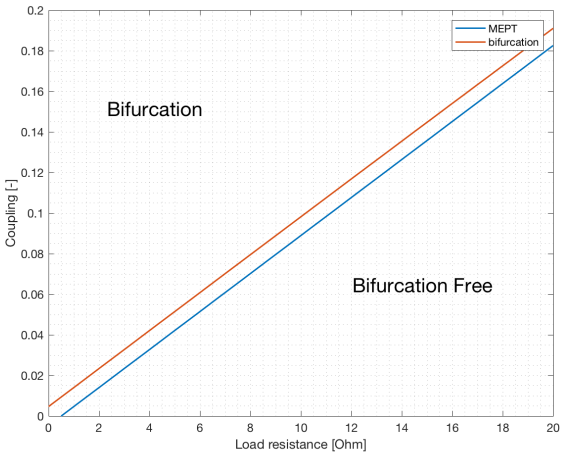

Figure 4.2.4: Bifurcation limit compared to maximum efficiency point

4.3 Power Control

From chapter 3 it is clear that controlling the input voltage gives the best results for controlling the output power of the system. Then from [18] it is known that for a series-series compensated IPT system the output power of the rectifier equals

$$P_2 = \frac{8U_{1,dc}U_{2,dc}}{\pi^2\omega_0 M} \tag{4.3.1}$$

Here $U_{1,2,dc}$ are the DC link voltages, ω_0 is the resonant frequency and M is the mutual inductance. From this it is clear that given a certain power setpoint P_2^*, with a known mutual inductance, the MEPT voltage $U_{2,dc}$ can be determined according to equation (4.2.9). After which $U_{1,dc}$ can be controlled to control the power, and since the transformer inductances are equal, the following setpoint for $U_{1,dc}$ holds:

$$U_{1,dc}^* = \frac{1}{\eta_{dc-dc}}\sqrt{\frac{L_p}{L_s}}U_{2,dc}^* \qquad \Rightarrow \qquad U_{1,dc}^* = \frac{1}{\eta_{dc-dc}}U_{2,dc}^* \tag{4.3.2}$$

Here $\eta_{dc/dc}$ is the dc to dc efficiency of the system (input of the inverter to output of the rectifier), and is determined experimentally. U_{1dc} is controlled using an additional dc/dc converter in front of the inverter.
From this section and the section above it is clear that by using two dc/dc converters MEPT and Power control can be performed. Using this information the total proposed control scheme can be designed, this will be discussed in the next section.

4.4 Misalignment Tolerant Proposed Setup & Control Scheme

In this section an overview of the proposed setup for a bidirectional misalignment tolerant IPT system is shown. From section 4.1 and 4.2 it is known that by controlling the primary and secondary dc link voltages the power can be controlled and MEPT can be performed. In order to determine the setpoints for these controllers the coupling factor of the transformer coils needs to be determined. The method used for this will be discussed in the next section.
Furthermore, from the experimental setup at the beginning of this thesis it was seen that for large misalignments (7 cm or more) the primary and secondary resonance frequency changes. This is because the spatial variation changes the self inductance of both coils which changes the resonance frequency of the tank. From the previous chapter it is known that when the switching frequency deviates from the resonance frequency, this decreases the power transfer efficiency. Therefor two frequency controllers also need to be implemented which track the resonance frequency of the tank. The process of desiging these controllers will be discussed in section 4.4. This results in the overview of the complete control scheme shown in Figure 4.4.1. Using the control equations the DC link voltages can be determined, these are given in table 4.4.1.

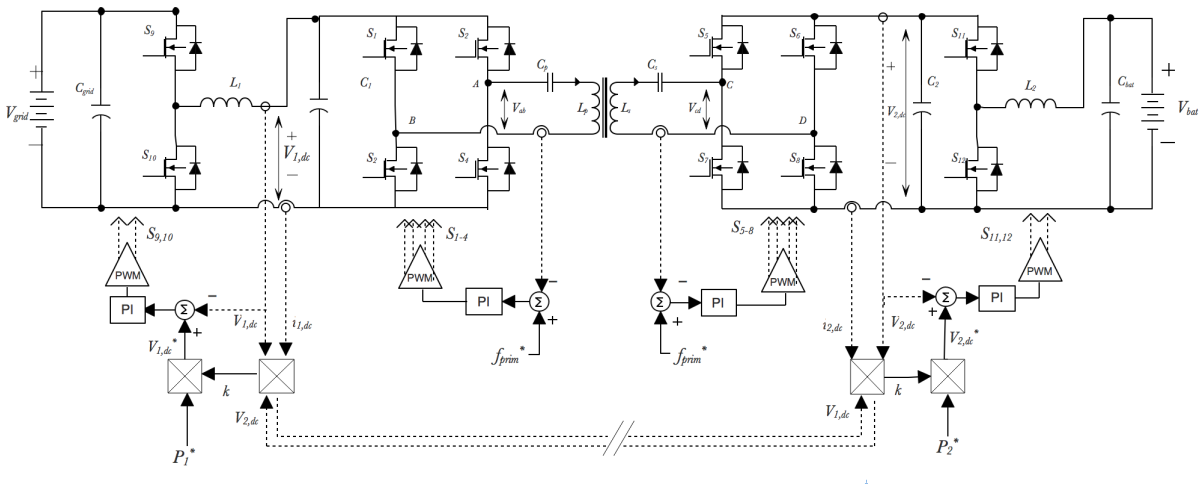

Figure 4.4.1: Misalignment Tolerant IPT setup and control scheme

Table 4.4.1: IPT system specifications

Parameter	Value
V_{grid}	350V
$U_{1,dc}$	30-120V
$U_{2,dc}$	30-120V
U_{bat}	48V
$P_{out,max}$	500W

4.5 COUPLING FACTOR ESTIMATION

In literature several ways of coupling factor estimation have been presented, for example, methods based on the voltage and current harmonics [19], using the voltages and currents from primary side [20], using the voltages and currents from secondary side [17][20] and from both primary as well as secondary side [21][22], also distinctions between stationary and dynamic charging are made [21][22]. In this thesis the charging will always be done stationary. Furthermore, since the system will be designed to be bidirectional, both primary and secondary side dc/dc converters will be used for MEPT (and power control, depending on the direction of power) therefor both sides have to be able to perform the measurements to estimate the coupling factor.

To do this, again the voltage equations given in equation (4.2.1) are used. Using the fact that $M = k\sqrt{L_p L_s}$ and not taking into account the load resistance for now, the voltage equations can be rewritten to:

$$\begin{bmatrix} V_p \\ V_s \end{bmatrix} = \begin{bmatrix} R_p & -j\omega_0 k\sqrt{L_p L_s} \\ j\omega_0 k\sqrt{L_p L_s} & -R_s \end{bmatrix} \begin{bmatrix} I_p \\ I_s \end{bmatrix} \tag{4.5.1}$$

From the primary voltage equation, the following equation can be derived for I_p:

$$I_p = \frac{V_p + j\omega_0 k\sqrt{L_p L_s} I_s}{R_p} \tag{4.5.2}$$

If equation (3.1.1) is then substituted in the secondary voltage equation a quadratic equation for k is obtained. If this is solved the following formula for k is obtained:

$$k = \frac{V_p + \sqrt{V_p^2 - 4R_p I_s\left(V_s + R_s I_s\right)}}{2I_s\omega_0\sqrt{L_p L_s}} \tag{4.5.3}$$

Here $V_{p,s}$ and $I_{p,s}$ are the RMS values of the fundamental primary and secondary voltages and currents, $R_{p,s}$ are the coil resistances, $L_{p,s}$ are the coil inductances and ω_0 is the resonant/operating frequency.

Next the fundamental values of the voltages and currents are replaced by their dc equivalents, this way no high bandwidth measurement equipment is needed to get accurate results [21]. The fundamental components are now replaced by their Fourier series expanded dc equivalents:

$$V_p = \frac{2\sqrt{2}}{\pi} V_{dc,1}, \qquad V_s = \frac{2\sqrt{2}}{\pi} V_{dc,2}, \qquad I_2 = \frac{\pi}{2\sqrt{2}} I_{dc,2} \tag{4.5.4}$$

If these are substituted in equation (3.1.2), the formula for k given in equation (3.1.3) is obtained.

$$k = \frac{4V_{dc,2} + \sqrt{16V_{dc}^2 - \pi R_1 i_{dc,2}\left(8V_{dc,2} + \pi^2 R_2 i_{dc,2}\right)}}{\pi^2 i_{dc,2} \omega_0 \sqrt{L_p L_s}} \tag{4.5.5}$$

In experimental validation section at the end of this chapter the accuracy of both the DC and AC estimation formulas will be investigated.

4.6 Resonance tracking

As said earlier, for large values of coil displacement the system tunes out of resonance. In theory this should not happen to a series-series compensated system, since the capacitor value is indepedant of mutual inductance and is compensating for the whole primary inductance.
However, at displacements higher than 7 cm (x- or y-direction) the change in self inductance of the coils is such, that the resonance frequency noticably starts to change. Since the formulas used above are only valid and because the losses increase when the system is out of resonance, it is necessary to ensure that the system stays in resonance. Therefore a resonance tracking system is needed which adapts the switching frequency accordingly.

There exist multiple ways of doing this, often phase locked loops (PLL's) are used for these kind of applications, however the output of a PLL is a frequency, which requires a high sample rate analog to digital converter (ADC) in order to read out the frequency at the micro controller. This makes the system more fault prone and more complex. Another method is to use a self oscillating circuit [18], here the zero crossings of the current are detected and used as a trigger to drive the switches. This way the system always operates at the resonance frequency, however additional start up circuitry are needed in order for the resonance current to start up. For this reason a third method was used [23]. Here the phase between the gate voltage and the zero crossing of the current is detected and converted to a dc value, such that the micro controller can read this value and compare and control it to a reference voltage to enable ZVS. Figure 4.6.1 shows a block diagram of this system.

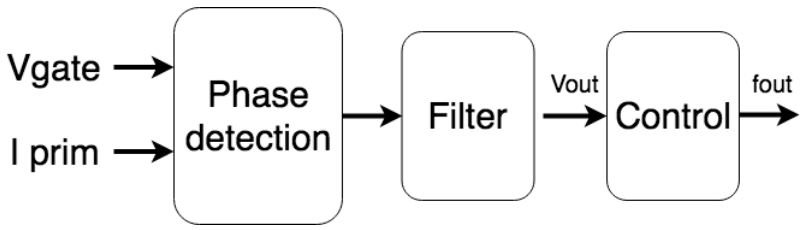

Figure 4.6.1: Block diagram of phase detection circuit

In order for this resonance tracker to work also for the synchronous rectifier, its gate voltages need to be synchronized to the inverter. Since otherwise the phase between the gate voltage and current will be a constantly varying, which makes it uncontrollable. Therefor the microcontroller of the rectifier is triggered by an external trigger signal of the inverter microcontroller with a 90° phase shift. This way only one controller is controlling the frequency, while the other is following this frequency which also makes the system more stable. In the next section the method of detecting the phase is discussed.

4.6.1 Phase Detection

The circuit used for detecting the phase is shown in Figure 4.6.2. Here the current is routed through a current transformer with a resistor on its secondary side. This voltage voltage is measured using a high speed op

amp (60MHz gain bandwidth product, in order to minimize the delay and get an accurate reading of the zero crossing of the current). The voltage over this shunt resitor is then lifted by 2.5V in order to make it a positive voltage, since the comparator can not handle negative voltages. This voltage is then compared to the same 2.5V reference in order to obtain a square wave voltage with the same zero crossings as the original current.

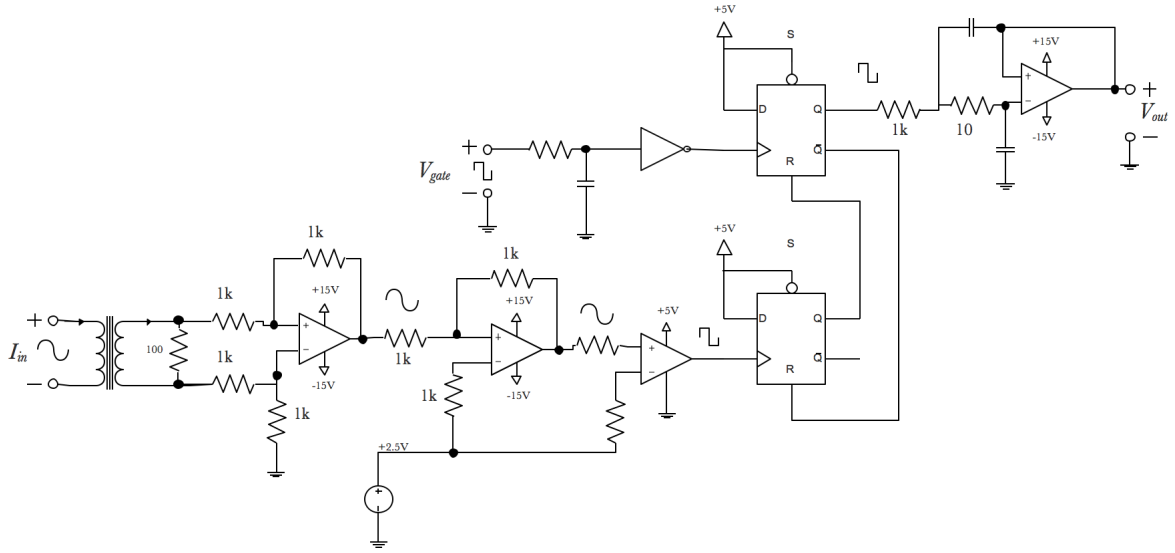

Figure 4.6.2: Phase detection circuit

This square wave is then connected to the CLK of the first D flip flop, while the NOT SET and DATA inputs are pulled high. The output of this flip flop is then connected to the reset of the second. The second flip flop is configured in the same way, with the inverted gate voltage (why it is inverted will be discussed later) at the CLK input and NOT Q connected to the reset of the first flip flop. Note that the gate voltage is first filtered using an RC filter with a cut of frequency of 1.5 MHz. This is done to eliminate switching noise, which could lead to false switching of the inverter IC.

By routing the flip flops in this way, the output of the second one toggles to high when the gate voltage gets high and is reset by the first flip flop when the current gets positive. This gives an output square wave with a duty cycle equal to the amount of phase between the current and voltage. This waveform is then filtered using a Chebyshev filter to obtain a dc value.

The gate voltage is inverted such that when the system is at resonance the system detects a phase of 180°, while for leading currents the system detects a phase of 0° – 180° and 180° – 360° for a lagging currents. This way a linear voltage to phase relationship is obtained for phases ranging from leading to lagging currents. This is shown in Figure 4.6.3.

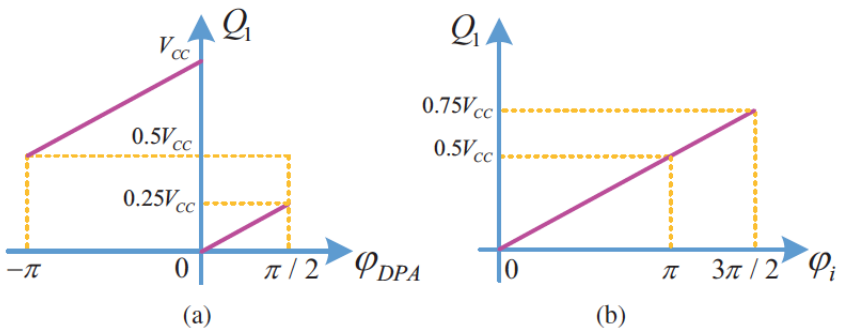

Figure 4.6.3: Output voltage vs phase

Simulation Results

In order to verify the operation of the circuit it is simulated in LT Spice. The results of this are shown in Figure 4.6.4a-b. Here the blue area is the output of the second flip flop, which is the input to the Chebyshev filter. The yellow waveform is the output of the comparator, the red waveform is the inverted gate voltage and the purple waveform is the voltage measured over the shunt resistor at the output of the current transformer. As said above, a rising edge of the gate voltage toggles the output of the flip flop to high, which is reset by a rising edge of the comparator. Because the gate voltage is inverted, the duty cycle of the output of the flip flop is 50% when the phase between the actual gate voltage and current is zero. For a leading current this duty cycle then increases, while for a lagging current it decreases.

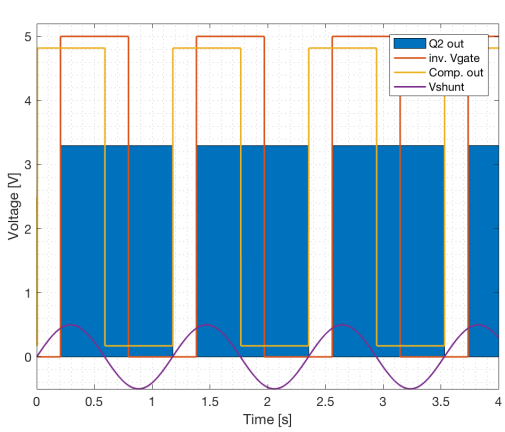

(a) Leading Current

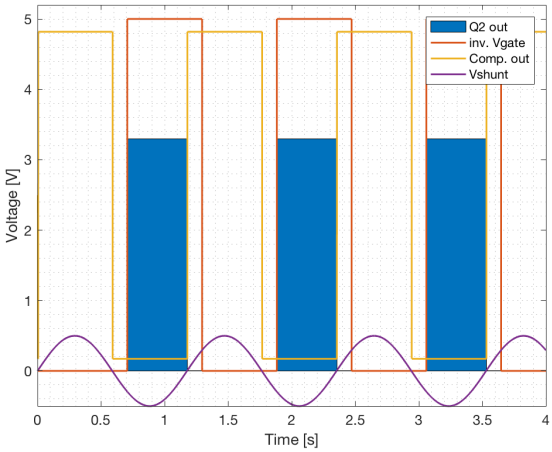

(b) Lagging Current

Figure 4.6.4: Simulation results for leading and lagging current

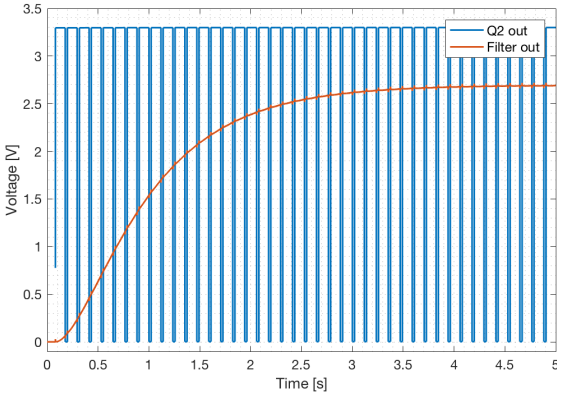

(a) Leading Current

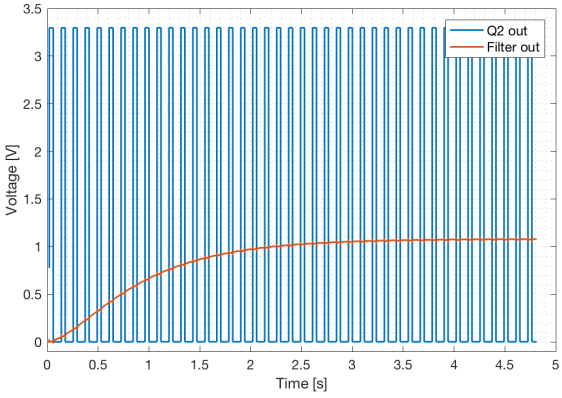

(b) Lagging Current

Figure 4.6.5: Filter in- and output voltages

4.7 Experimental Validation

In this section the proposed misalignment tolerant control setup will be validated on the setup. This is done using measurements performed on the setup, therefore this section does not discuss the experimental results of the control loop. This is done in Chapter 6.

4.7.1 Maximum Power point tracking

First the concept of MPPT is verified. An electronic load in constant voltage mode is used to change the output voltage of the (passive) rectifier. This is done at an output power of 150W, while changing the output voltage from 10 till 140V for multiple displacements in the x-direction (which is the lateral direction with respect to the DD-coil). The results of this are shown in Figure 4.7.1b. This can be compared to the simulation results of Figure 4.2.1a, here the relation between inductive link efficiency and output voltage is shown. This was calculated by combining eq. (4.2.4) and eq. (4.2.8).

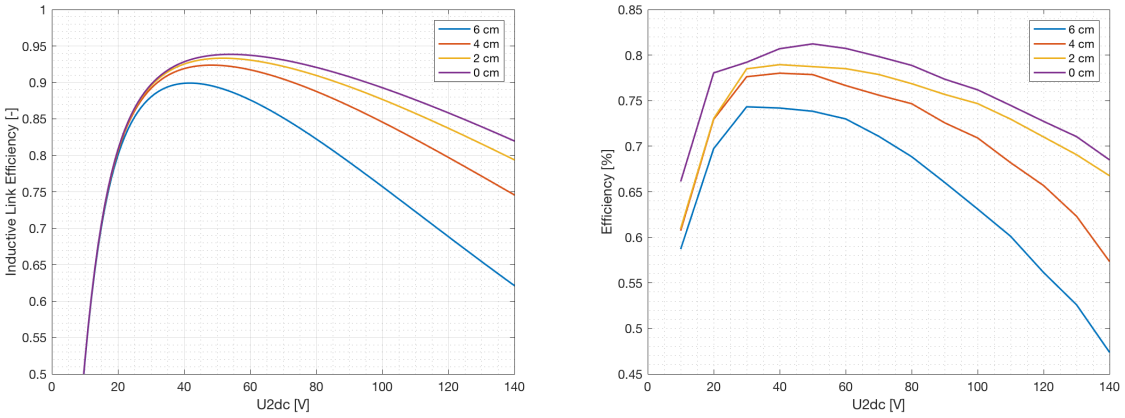

(a) simulation

(b) measurement

Figure 4.7.1: Efficiency vs. output voltage

The biggest difference between the measurements and the simulations is the achievable efficiency. This is because in the simulation all semiconductor losses were not taken into account. For this same reason the measured efficiencies also do not converge to the same line as in the simulation. However in both the simulation and the experimental results it can be seen that for different values of coupling/displacement, the voltage needed to achieve maximum efficiency differs and thus MPPT is possible.

4.7.2 Coupling Factor Estimation

Measurements are performed in order to validate the formula's mentioned in section 4.3 and to get an estimate on the accuracy of them. Here the coupling factor will be calculated using the measured AC values and DC values. As a base line the coupling factor will be measured using an open circuited secondary, using the setup as shown in Figure 4.6.6. (an additional resistance is placed in the primary circuit to prevent short circuiting the transformer). This way only the induced voltage ($j\omega_0 M I_p$) is measured on the secondary side and the mutual inductance will be easy to derive from this.

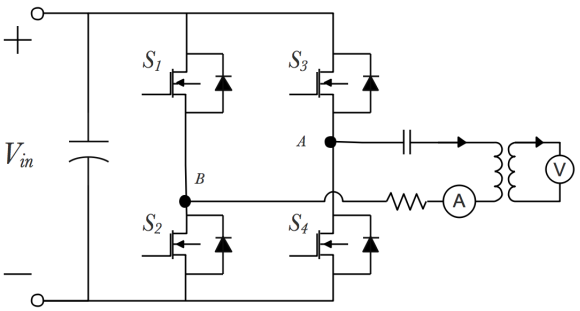

Figure 4.7.2: Coupling factor measurement setup

The measurements are performed using a 100MHz current probe to measure the primary current, a 100MHz differential voltage probe to measure the induced voltage on the secondary side and the input voltage. A hundred measurements will be performed on a 10 by 10 cm grid, where (0,0) indicates the fully alligned position. The results of the baseline measurements are shown in Figure 4.6.7.

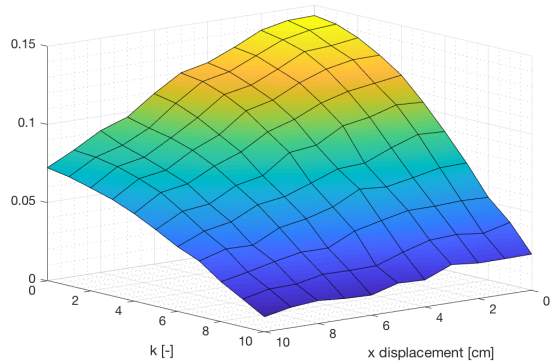

Figure 4.7.3: Baseline coupling factor measurement.

Next, the coupling is measured using the voltages and currents. This is done both offline and online (using probes and on the converter). The measurements are first performed offline such that the accuracy of both the AC and DC formula can be assest. This is done using the same probes as described above. The setup used for this is shown in Figure 4.6.8. Here V_2 and A_2 are the RMS values of the AC voltages and currents, while V_{in}, V_{dc} and A_{dc} are the DC voltages and currents (The RMS of a square wave equals its amplitude, therefor V_{in} is used in both AC and DC measurements).

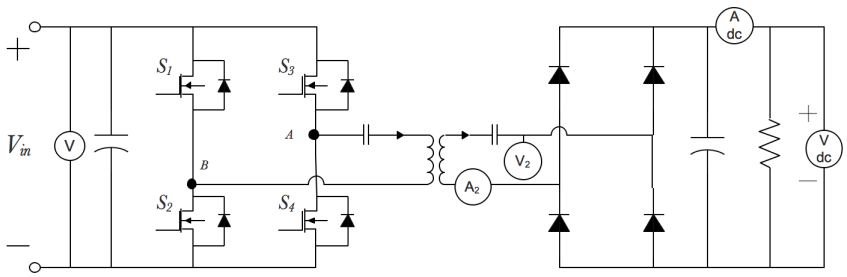

Figure 4.7.4: Measurement setup to perform AC and DC measurements

The results of the measurements are shown in Figure 4.6.9. The AC measurements show an average deviation from the baseline measurement of approximately 0.027 [-]. The average DC deviation equals approximately 0.016 [-]. As expected the DC measurements are more precise since these are easier to measure accurately, because the required bandwidth is much smaller. For this reason the dc formula will be used to estimate k. In the next chapter the design of the dc/dc converters and modeling of the entire system is discussed. Based on these models the gains of the voltage controllers are determined.

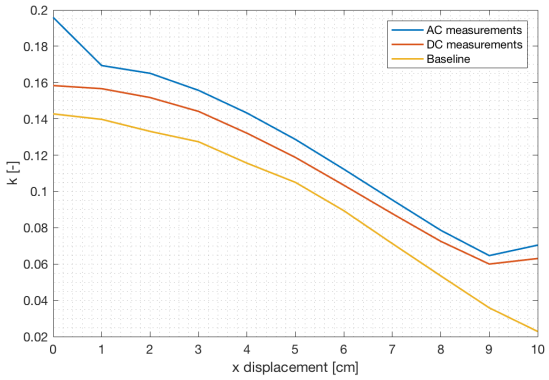

Figure 4.7.5: K measured offline, x = [0-10] cm, y = 0 cm

4.8 Conclusion

From Chapter 3 it is known that voltage control is the best control method for a bidirectional IPT system. In this chapter it was determined that by changing the output voltage of the rectifier the maximum efficiency point could be tracked. Then using this information a misalignment tolerant control scheme was proposed. Using two voltage controllers which estimate the coupling of the transformer and calculate and control the dc link voltages accordingly. Furthermore two frequency controllers are used to account for the change in resonance frequency under coil misalignment. The next step in the design of the control scheme is to determine the gains of the controllers. For the frequency controller this can not be based on an analytical model and will be done experimentally and is thus discussed in the experimental results chapter. The gains of the voltage controllers can be based on the frequency response of the system. In order to determine this response a dynamic model is made, which will be discussed in the next section.

CHAPTER 5

DYNAMIC MODELING

5.1 INTRODUCTION

In order to gain insight in the transient behaviour of the system and to determine the gains of the voltage controllers, a small signal model can be made. This model consists of 3 parts: a series series compensated inductive link, including inverter and rectifier and 2 dc/dc converters which operate as a buck or boost depending on the direction of power transfer. See Figure 5.1.1. For the design and parameter calculation of the dc/dc converters see Appendix C. An overview of all parameters of the system is given in table 5.1.1.

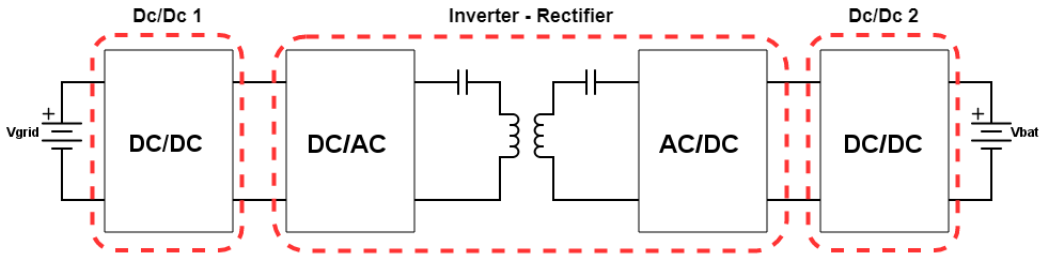

Figure 5.1.1: Complete inductive power transfer system

Table 5.1.1: Setup parameters

Symbol	Quantity	Value
V_{in}	Input Voltage	350V
V_{bat}	Battery Voltage	48V
L_P	Primary Inductance	200 μH
L_S	Secondary Inductance	200 μH
C_P	Primary Capacitance	18.9 nF
C_S	Secondary Capacitance	18.9 nF
L_1	Dc/dc 1 Inductor	2 μH
L_2	Dc/dc 2 Inductor	1 μH
C_1	Grid side DC link capacitance	300 μF
C_2	Vehicle side DC link capacitance	300 μF
C_{grid}	Grid side capacitor	15 μF
$C_{battery}$	Battery side capacitor	15 μF

All three models are linearized around an operating point of 500W (the choice of operating point has negligible effect on dynamic performace). The dc/dc converters are linearized using the state space averaging technique. For linearizing the inductive link a different technique has to be used, since the switching frequency is equal or near the natural resonance frequency and thus far above the Nyquist frequency, furthermore the small ripple approximation is not valid. In literature multiple methods for describing the dynamic behaviour

of series resonant converters are proposed, for example generalized state space averaging (GSSA)[24],time domain analysis (TDA)[25], and the concept of extended describing functions (EDF)[26][27][28] among other things. All of these are based on the principle of Fundamental Harmonic Approximation (FHA), here the signals are approximated to be (a sum of) sinusoids according to their Fourier expansion. However, the output of the GSSA method are complex quantities and is therefore unsuitable for the design of PI controller. Furthermore, eventhough the TDA concept has proven that the FHA concept can be inaccurate under certain conditions, it it is still far more complex. Therefor the extended describing functions method is chosen since it provides a good trade off between accuracy and complexity and is proven to be accurate for series-series compensated IPT system.[26][27][28].

During the modeling process following assumptions are made

1. All switches are lossless and do not have any parasitic capacitance or inductance
2. Primary and secondary resonant currents are pure sinusoidal
3. Deadtime is neglected
4. The in- and output of the dc/dc converters are without ripple
5. The dc/dc converters operate in continous conduction mode and the small ripple approximation is valid inside the dc/dc model

The final model is comprised of the three models by equating the in- and outputs of each seperate model and expressing them in state variables. Now first the inductive link will be discussed.

5.2 Inductive Link

Any (series) resonant converter is a strongly non-linear system, unfortunately conventional control techniques are based upon linear systems. In order to linearize the system the EDF method is used. This method replaces the linear terms with their sinusoidal approximations and the non linear terms are replaced by the so called 'describing functions'[27].
Using this method two models were made, where one reflects all secondary side variables to the primary side and thus reduces the order of the system [5], the other does not. By verifying the models using PLECS 4.1.1 it turned out the reduced model was not accurate enough (the bode plot of this can be seen in Appendix D.). Therefor the full system model was used and will be further explained in this section. To do this the equivalent circuit shown in Figure 2. is used.

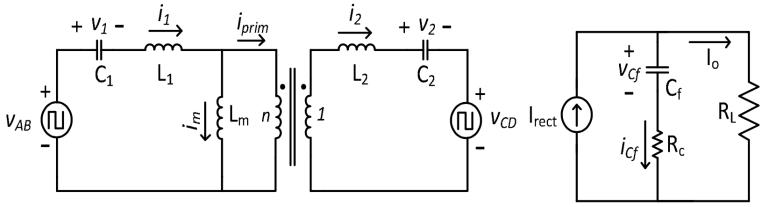

Figure 5.2.1: Equivalent circuit of inductive link

Following the method proposed in [4] the state space equations are as follows:

$$\frac{di_1}{dt} = \frac{1}{L_{eq2}} v_{ab} - \frac{1}{L_{eq2}} v_1 - \frac{1}{L_{eqm}} v_2 - \frac{1}{L_{eqm}} v_{cd} \tag{5.2.1}$$

$$\frac{di_2}{dt} = \frac{1}{L_{eqm}} v_{ab} - \frac{1}{L_{eqm}} v_1 - \frac{1}{L_{eq1}} v_2 - \frac{1}{L_{eq1}} v_{cd} \tag{5.2.2}$$

$$\frac{dv_1}{dt} = \frac{i_1(t)}{C_1} \tag{5.2.3}$$

$$\frac{dv_2}{dt} = \frac{i_2(t)}{C_2} \tag{5.2.4}$$

$$\frac{dv_{cf}(t)}{dt} = \frac{i_{rect}R_L - v_{cf}(t)}{(1+\frac{R_c}{R_L})R_L C_f} \tag{5.2.5}$$

Where,

$$L_{eq1} = \frac{(L_1+L_M)(L_2+L_M)-L_m^2}{L_1+L_M} \tag{5.2.6}$$

$$L_{eq2} = \frac{(L_1+L_M)(L_2+L_M)-L_m^2}{L_2+L_M} \tag{5.2.7}$$

$$L_{eqm} = \frac{(L_1+L_M)(L_2+L_M)-L_m^2}{L_M} \tag{5.2.8}$$

Here $i_{1,2}$ are the primary and secondary capacitor currents comprising of the magnetizing current i_m and primary inductor current i_{prim}, $v_{1,2}$ are the primary and secondary capacitor voltages, i_{Cf} is the output capacitor current and I_{out} is the output current through R_L the load resistor. Furthermore $C_1,2$ are primary and secondary capacitors, C_f is the rectifier filter capacitor and $L_{1,2,M}$ are the primary, secondary and mutual inductance.
Now through Taylor series expansion, the voltages V_{AB} and V_{CD} can be described in terms of terms of (co)sinuses, as shown in equation 5.2.9, here $f_{1,2}(v_{dc})$ are called the describing function. This results in the following voltages:

$$V_{AB} = f_1(v_{dc})sin(\omega_s t) + f_2(v_{dc})cos(\omega_s t) = \frac{4V_{dc}}{\pi}sin(\omega_s t) \tag{5.2.9}$$

$$V_{CD} = \frac{4i_{2s}v_{Cf}}{\pi I_S}sin(\omega_s t) + \frac{4i_{2c}v_{Cf}}{\pi I_S}cos(\omega_s t) \tag{5.2.10}$$

V_{AB} only consists of a sinus term with amplitude $\frac{4}{\pi}$ (which is the amplitude of the fundamental wave from square wave). V_{CD} consists of sinus and cosinus terms because it is phase shifted with respect to V_{AB}.
Next, all voltages and currents can be approximated to be sinusoidal (apart from the output of the rectifier), since a series series compensated resonant circuit acts as a bandpass filter and active power is only transferred via the first harmonic [25][27]. If this approximation is applied to equations (5.2.1)-(5.2.4), while substituting (5.2.9) and (5.2.10) and seperating sine and cosine terms. The following equations are obtained for the sine terms:

$$\frac{di_{1s}}{dt} = \frac{v_e}{L_{eq2}} - \frac{v_{1s}}{L_{eq2}} - \frac{v_{2s}}{L_{eqm}} + \omega_s i_{1c} - \frac{4i_{2s}v_{cf}}{\pi L_{eqm} I_S} \tag{5.2.11}$$

$$\frac{di_{2s}}{dt} = \frac{v_e}{L_{eqm}} - \frac{v_{1s}}{L_{eqm}} - \frac{v_{2s}}{L_{eq1}} + \omega_s i_{2c} - \frac{4i_{2s}v_{cf}}{\pi L_{eq1} I_S} \tag{5.2.12}$$

$$\frac{dv_{1s}}{dt} = \frac{i_{1s}}{C_1} + \omega_s v_{1c} \tag{5.2.13}$$

$$\frac{dv_{2s}}{dt} = \frac{i_{2s}}{C_2} + \omega_s v_{2c} \tag{5.2.14}$$

and for the cosine terms:

$$\frac{di_{1c}}{dt} = -\frac{v_{1c}}{L_{eq2}} - \frac{v_{2c}}{L_{eqm}} - \omega_s i_{1s} - \frac{4i_{2c}v_{cf}}{\pi L_{eqm} I_S} \tag{5.2.15}$$

$$\frac{di_{2c}}{dt} = -\frac{v_{1c}}{L_{eqm}} - \frac{v_{2c}}{L_{eq1}} - \omega_s i_{2s} - \frac{4i_{2c}v_{cf}}{\pi L_{eq1} I_S} \tag{5.2.16}$$

$$\frac{dv_{1c}}{dt} = \frac{i_{1c}}{C_1} + \omega_s v_{1s} \tag{5.2.17}$$

$$\frac{dv_{2s}}{dt} = \frac{i_{2c}}{C_2} + \omega_s v_{2s} \tag{5.2.18}$$

Next the DC terms are:

$$C_f\frac{dv_{cf}}{dt} = \frac{2R_L i_S}{\pi(R_L+R_c)} - \frac{v_{cf}}{R_L+R_c} \tag{5.2.19}$$

In the above equations i_S is defined as $i_S^2 = i_{2s}^2 + i_{2c}^2$. These equations represent the large signal model of the

inductive link. In order to get the linearized small signal model, every state variable can be expressed in its steady state value and its small signal perturbation according to:

$$\bar{x} = X + \hat{x} \tag{5.2.20}$$

After doing this the equations contain steady state components and small signal components. From this set of equations the steady state matrix equation can be obtained, the results of solving this equation can then be used in the small signal matrix equation, obtained from the same set of equations. The steady state matrix equation is given in equation (5.2.21)

$$\begin{bmatrix} V_e \\ V_e \\ 0 \\ 0 \\ 0 \\ 0 \\ 0 \\ 0 \end{bmatrix} = \begin{bmatrix} 0 & 0 & 1 & 0 & \Omega C_1 & 0 & 0 & 0 \\ -\Omega C_1 & 0 & 0 & 0 & 0 & 0 & 1 & 0 \\ 0 & 0 & 0 & 1 & 0 & \Omega C_2 & 0 & 0 \\ 0 & -\Omega C_2 & 0 & 0 & 0 & 0 & 0 & 1 \\ 1 & \frac{L_{eq2}}{L_{eqm}} & 0 & \frac{L_{eq2}R_e}{L_{eqm}} & 0 & 0 & -\Omega L_{eq2} & 0 \\ 0 & 0 & \Omega L_{eq2} & 0 & 1 & \frac{L_{eq2}}{L_{eqm}} & 0 & \frac{L_{eq2}R_e}{L_{eqm}} \\ 1 & \frac{L_{eqm}}{L_{eq1}} & 0 & \frac{L_{eqm}R_e}{L_{eq1}} & 0 & 0 & 0 & -\Omega L_{eqm} \\ 0 & 0 & 0 & \Omega L_{eqm} & 1 & \frac{L_{eqm}}{L_{eq1}} & 0 & \frac{L_{eqm}R_e}{L_{eq1}} \end{bmatrix} 0 \begin{bmatrix} I_{1s} \\ I_{1c} \\ I_{2s} \\ I_{2c} \\ V_{1s} \\ V_{1c} \\ V_{2s} \\ V_{2c} \end{bmatrix} \tag{5.2.21}$$

Furthermore:

$$V_{Cf} = \frac{2}{\pi} I_s R_L \tag{5.2.22}$$

and

$$V_e = \frac{4}{\pi} V_{dc} \tag{5.2.23}$$

By solving this equation the steady state values are found. These are then used in the small signal state space model. $\frac{d\hat{x}}{dt} = A\hat{x} + B\hat{u}$ and $y = C\hat{x} + D\hat{u}$

$$A = \begin{bmatrix} 0 & \Omega_s & -A_1 & A_2 & \frac{-1}{L_{eq2}} & 0 & \frac{-1}{L_{eqm}} & 0 & -A_3 \\ -\Omega_s & 0 & A_4 & A_5 & 0 & -\frac{-1}{L_{eq2}} & 0 & \frac{-1}{L_{eqm}} & A_6 \\ 0 & 0 & -A_7 & \Omega_s + A_8 & \frac{-1}{L_{eqm}} & 0 & \frac{-1}{L_{eq1}} & 0 & -A_9 \\ 0 & 0 & -\Omega + A_{10} & -A_{11} & 0 & -\frac{-1}{L_{eqm}} & 0 & \frac{-1}{L_{eq1}} & -A_{12} \\ \frac{1}{C_1} & 0 & 0 & 0 & 0 & \Omega_s & 0 & 0 & 0 \\ 0 & \frac{1}{C_1} & 0 & 0 & \Omega_s & 0 & 0 & 0 & 0 \\ 0 & 0 & \frac{1}{C_2} & 0 & 0 & 0 & 0 & \Omega_s & 0 \\ 0 & 0 & 0 & \frac{1}{C_2} & 0 & 0 & -\Omega_s & 0 & 0 \\ 0 & 0 & A_{13} & A_{14} & 0 & 0 & 0 & 0 & -A_{15} \end{bmatrix} B = \begin{bmatrix} B_1 \\ 0 \\ B_2 \\ 0 \\ 0 \\ 0 \\ 0 \\ 0 \\ 0 \end{bmatrix}. \tag{5.2.24}$$

$$C = \begin{bmatrix} 0 & 0 & C_{11} & C_{12} & 0 & 0 & 0 & 0 & C_{13} \end{bmatrix}. \tag{5.2.25}$$

$$\hat{D} = 0 \tag{5.2.26}$$

$$\hat{x} = \begin{bmatrix} \hat{i}_{1s} & \hat{i}_{1c} & \hat{i}_{2s} & \hat{i}_{2c} & \hat{v}_{1s} & \hat{v}_{1c} & \hat{v}_{2s} & \hat{v}_{2c} & \hat{v}_{cf} \end{bmatrix}^T. \tag{5.2.27}$$

$$\hat{u} = \hat{V}_{dc} \tag{5.2.28}$$

Here the following matrix entries are used:

$$A_1 = \frac{4I_{2c}^2 V_{Cf}}{\pi L_{eqm} I_S^3} \qquad A_4 = \frac{4I_{2c} I_{2s} V_{Cf}}{\pi L_{eqm} I_S^3} \qquad A_7 = \frac{4I_{2c}^2 V_{Cf}}{\pi L_{eq1} I_S^3}$$

$$A_2 = \frac{4I_{2c} I_{2s} V_{Cf}}{\pi L_{eqm} I_S^3} \qquad A_5 = \frac{4I_{2s}^2 V_{Cf}}{\pi L_{eqm} I_S^3} \qquad A_8 = \frac{4I_{2c} I_{2s} V_{Cf}}{\pi L_{eq1} I_S^3}$$

$$A_3 = \frac{4I_{2s}}{\pi L_{eqm} I_S} \qquad A_6 = \frac{4I_{2c}}{\pi L_{eqm} I_S} \qquad A_9 = \frac{4I_{2s}}{\pi L_{eq1} I_S}$$

$$A_{10} = \frac{4I_{2c}I_{2s}V_{Cf}}{\pi L_{eq1}I_S^3} \qquad A_{13} = \frac{2R_L I_{2s}}{\pi C_f(R_L+R_c)I_S} \qquad B_2 = \frac{4}{\pi L_{eqm}}$$
$$A_{11} = \frac{4I_{2s}^2 V_{Cf}}{\pi L_{eq1}I_S^3} \qquad A_{14} = \frac{2R_L I_{2c}}{\pi C_f(R_L+R_c)I_S} \qquad C_1 = \frac{2R_c R_L I_{2s}}{\pi(R_L+R_c)I_S}$$
$$A_{12} = \frac{4I_{2c}}{\pi L_{eq1}I_S} \qquad A_{15} = \frac{1}{C_f(R_L+R_c)} \qquad C_2 = \frac{2R_c R_L I_{2c}}{\pi(R_L+R_c)I_S}$$
$$B_1 = \frac{4}{\pi L_{eq2}} \qquad C_3 = \frac{R_L}{R_L+R_c}$$

For the case that $V_{DC} = 100V$ and $R_L = 17\Omega$ the $\frac{\hat{V_{in}}}{\hat{V_{out}}}$ bode plot is shown in Figure 5.2.2a. The result was verified using PLECS 4.1.1 (see Appendix E.. Figure 5.2.2b shows the magnitude plot of the PLECS model versus the small signal model. From this it is clear that the small signal is very accurate over the entire frequency range.

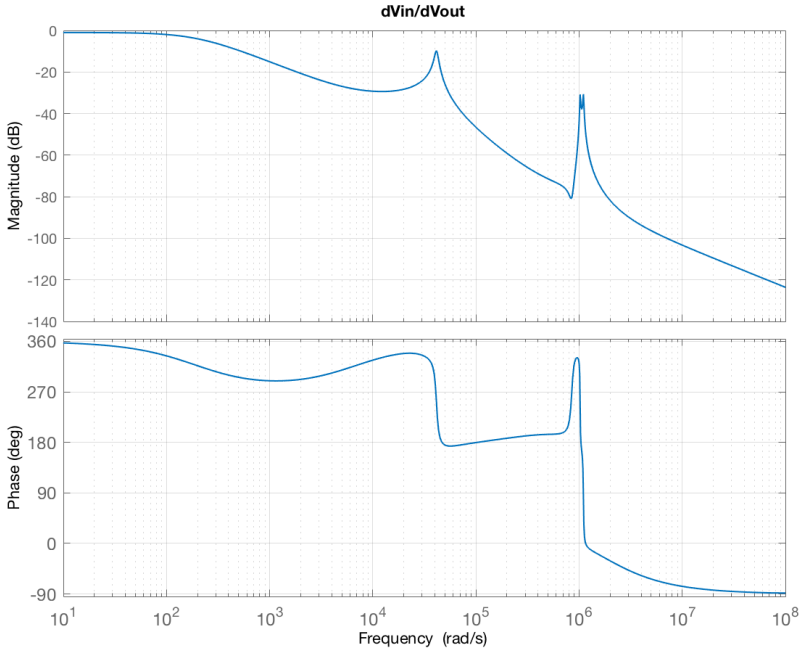

(a) Bode plot of small signal model

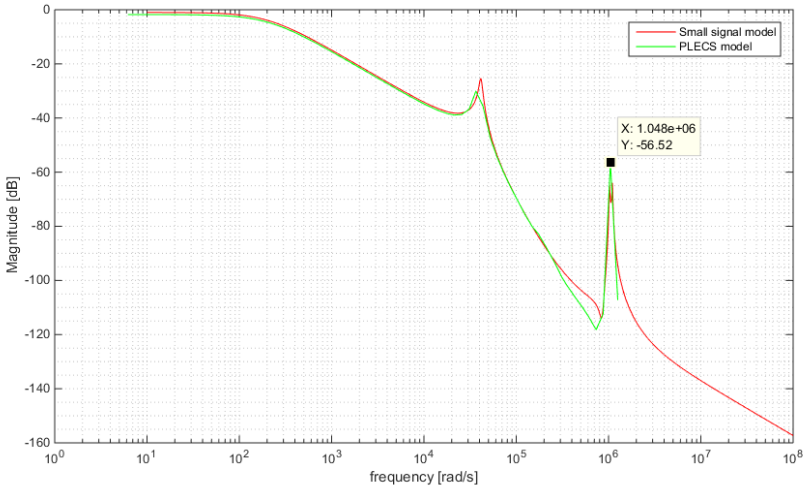

(b) Magnitude plot model vs PLECS

Figure 5.2.2: Bode plots

5.3 DC/DC 1

Depending on the direction of power transfer, power is transferred from grid to vehicle (G2V) or vehicle to grid (V2H). For G2V transfer the dc/dc converters are operating as buck converters, for V2H the converters are operating as boost converters. Note that in the following analysis, when talking about duty cycles, the duty cycle of the switch corresponding to a conventional 1-switch buck or boost converter is ment (Eventhough the diode is replaced by a second switch, since it are half bridge converters). First the G2V case is discussed.

5.3.1 BUCK MODE

Figure 5.3.1a and 5.3.1b show the equivalent circuits of a continuous conduction mode (CCM) buck converter for $0 \leqslant t \leqslant dT_s$ and $dT_s \leqslant t \leqslant (1-d)T_s$ respectively. As mentioned above, here d is the duty cycle of the top switch.

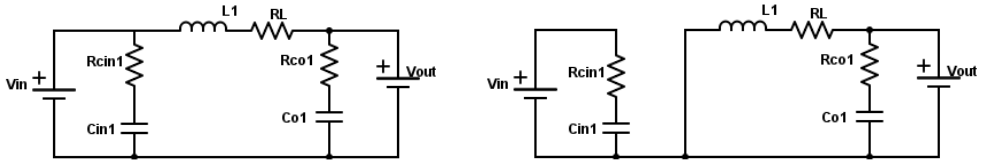

(a) Buck equivalent circuit during dTs (b) Buck equivalent circuit during (1-d)Ts

Figure 5.3.1: Buck converter equivalent circuits

For the period $0 \leqslant t \leqslant dT_s$:

$$\frac{dI_L}{dt} = \frac{1}{L}(V_{in} - I_L R_L - V_{out}) \tag{5.3.1}$$

$$\frac{dV_{Ci}}{dt} = \frac{1}{R_{Ci}C_i}(V_{in} - V_{ci}) \tag{5.3.2}$$

$$\frac{dV_{Co}}{dt} = \frac{1}{C_o}(I_L - I_{out}) \tag{5.3.3}$$

For the period $dT_s \leqslant t \leqslant T_s$:

$$\frac{dI_L}{dt} = \frac{1}{L}(-I_L R_L - V_{out}) \tag{5.3.4}$$

$$\frac{dV_{Ci}}{dt} = \frac{1}{R_{Ci}C_i}(V_{in} - V_{ci}) \tag{5.3.5}$$

$$\frac{dV_{Co}}{dt} = \frac{1}{C_o}(I_L - I_{out}) \tag{5.3.6}$$

Here $V_{in} = V_{grid}$ and $V_{out} = U_{1dc}$. Since U_{1dc} is not an input it should be expressed in state variables (Only the DC grid voltage, battery voltage and the duty cycles of the switches are inputs). Therefor V_{out} is expressed as $V_{Co1} + R_{Co1}(I_{L1} - I_{out})$,I_{out} will later be expressed in terms of primary current.
The next step is to average the equations over the time interval for which they are valid. So for the equations for the period $0 \leqslant t \leqslant dT_s$, this means multiplying them with d_1 and for the equations valid during $dT_s \leqslant t \leqslant T_s$ this means multiplication with $(1-d_1)$. Finally the averaged equations of each time period are added in order to form the averaged state space model (5.3.7-9):

$$\frac{dI_{L1}}{dt} = \frac{d_1}{L}(V_{in}) + \frac{1}{L1}(-I_{L_1}R_{L_1} - (V_{Co1} + R_{Co1}(I_{L1} - I_{out}))) \tag{5.3.7}$$

$$\frac{dV_{Ci}}{dt} = \frac{1}{R_{Ci}C_i}(V_{in} - V_{ci}) \tag{5.3.8}$$

$$\frac{dV_{Co}}{dt} = \frac{1}{C_o}(I_L - I_{out}) \tag{5.3.9}$$

Next the small signal model is obtained by replacing the averaged large signal terms by their steady state value and small signal perturbation as in equation (5.2.20). Since only the AC perturbation terms are of interest, the DC terms are left out of the equation. Furthermore, the second order AC terms are neglected in order to get a linear system. This is possible since the second order terms have negligible values. After doing this the following small signal equations are obtained:

$$\frac{d\hat{i}_{L1}}{dt} = \frac{D_1}{L}(\hat{v}_{in}) + \frac{\delta_1}{L}(V_{in}) + \frac{1}{L1}(-\hat{i}_{L_1}R_{L_1} - (\hat{v}_{Co1} + R_{Co1}(\hat{i}_{L1} - \hat{i}_{out}))) \tag{5.3.10}$$

$$\frac{d\hat{v}_{Ci}}{dt} = \frac{1}{R_{Ci}C_i}(\hat{v}_{in} - \hat{v}_{ci}) \tag{5.3.11}$$

$$\frac{d\hat{v}_{Co}}{dt} = \frac{1}{C_o}(\hat{i}_L - \hat{i}_{out}) \tag{5.3.12}$$

Then using these small signal equations the state space model of the converter in buck mode can be made and is shown in eq. (5.3.13) and .(5.3.14).

$$\dot{x} = \begin{bmatrix} \frac{-R_{Co1}-R_{L_1}}{L_1} & 0 & \frac{-1}{L_1} \\ 0 & \frac{-1}{R_{Ci1}C_{i1}} & 0 \\ \frac{1}{C_{o1}} & 0 & 0 \end{bmatrix} \begin{bmatrix} \hat{i_{L1}} \\ \hat{v}_{Ci1} \\ \hat{v}_{Co1} \end{bmatrix} + \begin{bmatrix} \frac{D_1}{L_1} & \frac{R_{Co1}}{L_1} & \frac{V_{in}}{L_1} \\ \frac{1}{R_{Co1}C_{o1}} & 0 & 0 \\ 0 & \frac{1}{C_{o1}} & 0 \end{bmatrix} \begin{bmatrix} \hat{V}_{in} \\ \hat{i}_{out} \\ \delta \end{bmatrix} \tag{5.3.13}$$

$$y = V_{out} = \begin{bmatrix} R_{Co1} & 0 & 1 \end{bmatrix} \begin{bmatrix} \hat{i_{L1}} \\ \hat{v}_{Ci1} \\ \hat{v}_{Co1} \end{bmatrix} + \begin{bmatrix} 0 & -R_{Co1} & 0 \end{bmatrix} \begin{bmatrix} \hat{V}_{in} \\ \hat{i}_{out} \\ \delta_1 \end{bmatrix} \tag{5.3.14}$$

The transfer function of $\frac{V_{out}}{d_1}$ results in the bode plot of figure 1.6, here $V_{out} = V_{Co1} + R_c(I_{L1} - i_{out}$. The result is a similar to what one would expect from a $\frac{V_{out}}{d}$ bode plot of a buck converter: showing the response of a LC low pass filter with an additional phase increase due to the zero induced by the equivalent series resistance (ESR) of the output capacitor. Physically this resistance can be seen as a damper, since the power dissipated by the resistor helps with avoiding oscillations. Next dc/dc 1 operating in boost mode will be discussed.

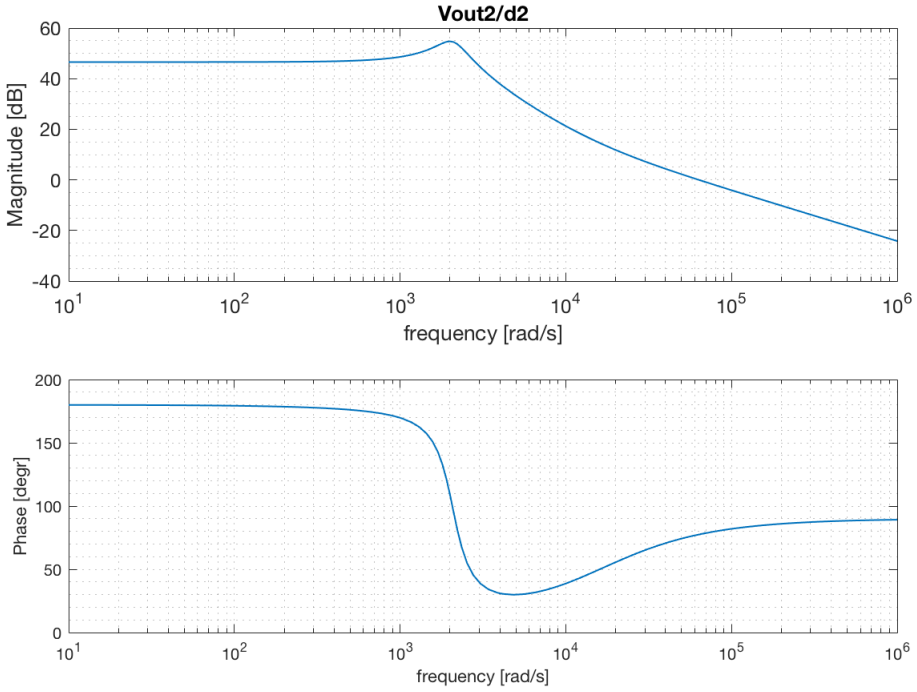

Figure 5.3.2: $\frac{V_{out1}}{d1}$ Bode plot for dc/dc operating in buck mode

5.3.2 Boost Mode

Figure 5.3.3a and b show the equivalent circuits of a boost converter during dTs and $(1-d)Ts$ respectively. The converter operates in continuous conduction mode (CCM).

For the period $0 \leqslant t \leqslant dT_s$:

$$\frac{dI_L}{dt} = \frac{1}{L}(V_{in} - I_L R_L) \tag{5.3.15}$$

$$\frac{dV_{Ci}}{dt} = \frac{1}{C_i}(I_{in} - I_L) \tag{5.3.16}$$

$$\frac{dV_{Co}}{dt} = \frac{1}{R_{Co}C_o}(V_o - V_{Co}) \tag{5.3.17}$$

$$\frac{dV_{Ci}}{dt} = \frac{1}{C_i}(I_{in} - I_L) \tag{5.3.19}$$

for the period $dT_s \leqslant t \leqslant T_s$:

$$\frac{dV_{Co}}{dt} = \frac{1}{R_{Co}C_o}(V_o - V_{Co}) \tag{5.3.20}$$

$$\frac{dI_L}{dt} = \frac{1}{L}(V_{in} - I_L R_L - V_{out}) \tag{5.3.18}$$

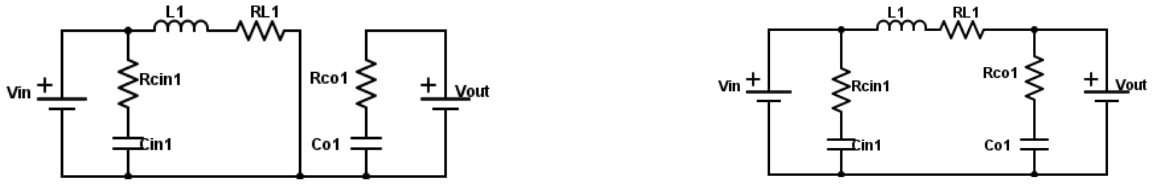

(a) boost converter during dTs

(b) Boost converter during period (1-d)Ts

Figure 5.3.3: Individual effect of changing the controller parameters

Now, since the power flow is reversed, the input voltage is $U_{1,dc}$ and the output voltage is V_{grid}. Therefor V_{in} is expressed as: $V_{ci1} + R_c(I_{in1} - I_L 1)$, so that I_{in1} later can be replaced by I_S, which is the rectifier output current specified by the inductive link model. This results in the following averaged state space equations:

$$\frac{dI_L}{dt} = \frac{1}{L}((V_{ci} + R_{ci}(I_{in1} - I_L) - I_L R_L) - \frac{1-d}{L}(V_{grid}) \tag{5.3.21}$$

$$\frac{dV_{Ci}}{dt} = \frac{1}{C_i}(\frac{\pi}{2\sqrt{2}} I_{in1} - I_L) \tag{5.3.22}$$

$$\frac{dV_{Co}}{dt} = \frac{1}{R_{Co}C_o}(V_o - V_{Co}) \tag{5.3.23}$$

Note here that C_i for the boost case is the same capacitor as C_o in the buck case. Furthermore d_{boost} is the duty cycle of the bottom switch in order to be coherent with a single switch boost converter model. This results in the small signal equations (5.3.24)-(5.3.26) and state space equations of eq. (5.3.27)and (5.3.28)

$$\frac{d\hat{i}_L}{dt} = \frac{1}{L}(\hat{v}_{ci} + R_{ci}(\hat{i}_{in1} - \hat{i}_L) - \hat{i}_L R_L) - \frac{1-D}{L}(\hat{v}_{grid}) + \frac{\delta}{L} V_{grid} \tag{5.3.24}$$

$$\frac{d\hat{v}_{Ci}}{dt} = \frac{1}{C_i}(\hat{i}_{in} - \hat{i}_L) \tag{5.3.25}$$

$$\frac{d\hat{v}_{Co}}{dt} = \frac{1}{R_{Co}C_o}(\hat{v}_o - \hat{v}_{Co}) \tag{5.3.26}$$

$$\dot{x} = \begin{bmatrix} \frac{-R_{Co1}-R_{L1}}{L_1} & \frac{-1}{L_1} & 0 \\ \frac{-1}{C_{i1}} & 0 & 0 \\ 0 & 0 & \frac{1}{R_{Co1}C_{o1}} \end{bmatrix} \begin{bmatrix} \hat{i_{L1}} \\ \hat{v}_{Ci1} \\ \hat{v}_{Co1} \end{bmatrix} + \begin{bmatrix} \frac{-1+D_1}{L_1} & \frac{R_{Ci1}}{L_1} & \frac{V_{grid}}{L_1} \\ 0 & \frac{1}{C_{i1}} & 0 \\ \frac{1}{R_{Co1}C_{o1}} & 0 & 0 \end{bmatrix} \begin{bmatrix} \hat{V}_{in} \\ \hat{i}_{out} \\ \delta \end{bmatrix} \tag{5.3.27}$$

$$y = V_{in} = \begin{bmatrix} -R_{Ci1} & 1 & 0 \end{bmatrix} \begin{bmatrix} \hat{i_{L1}} \\ \hat{v}_{Ci1} \\ \hat{v}_{Co1} \end{bmatrix} + \begin{bmatrix} 0 & -R_{Ci1} & 0 \end{bmatrix} \begin{bmatrix} \hat{V}_{in} \\ \hat{i}_{out} \\ \delta_1 \end{bmatrix} \tag{5.3.28}$$

These equations result in the $\frac{V_{in1}}{d_1}$ bode plot shown in Figure 1.8 is, again showing the frequency response of LC filter (now at the input of the converter) including the zero due to ESR. Note here that there is no phase shift due to a right half plane zero (RHPZ), which one would normally expect in the output voltage to duty cycle bode plot of a boost converter. However, this RHPZ is caused by the fact that for an increasing duty cycle, the inductor is connected to the load for a shorter amount of time. Therefor the output voltage initially drops

before it starts to increase. However, the output of the model here is the input voltage, which is connected to the inductor during the whole period. Therefor the bode plot is similar to one of a buck converter ($\frac{V_{out,buck}}{d_{buck}}$.

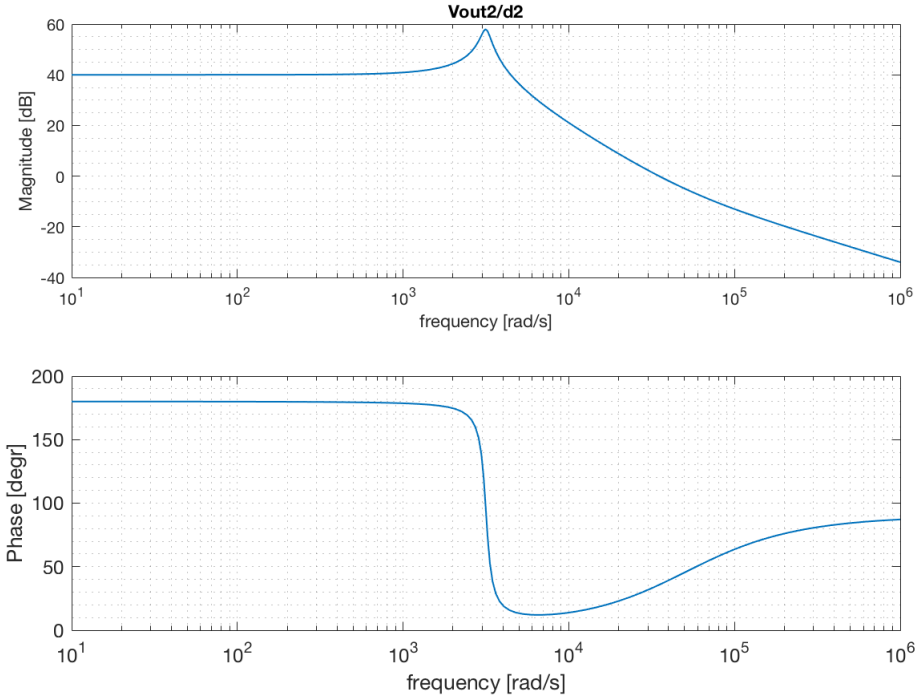

Figure 5.3.4: Bode plot of CCM Boost converter

5.4 Dc/Dc 2

The same method is now used for modeling the second dc/dc converter. Again the G2V (buck) case is discussed first.

5.4.1 Buck Mode

Now the output voltage is equal to the battery voltage and is an input of the system, while the input voltage of this converter is expressed in state variables using: $V_{in} = V_{ci} + R_{Ci}(I_{in} - I_L)$. This results in the following small signal equations and state space model:

$$\frac{d\hat{i}_{L2}}{dt} = \frac{D_2}{L}(\hat{v}_{Ci2} + R_c(\hat{i}_{in2} - \hat{i}_L)) + \frac{\delta_2}{L}(V_{Ci2} + R_c(I_{in2} - I_L)) - \frac{1}{L2}(\hat{v}_{bat} + \hat{i}_{L_2}R_{L_2}) \tag{5.4.1}$$

$$\frac{d\hat{v}_{Ci2}}{dt} = \frac{1}{C_{i2}}(\hat{i}_{in2}) - \frac{D_2}{C_{i2}}(\hat{i}_{L2}) - \frac{\delta}{C_{i2}}(\hat{i}_{L2}) \tag{5.4.2}$$

$$\frac{d\hat{v}_{Co2}}{dt} = \frac{1}{C_{o2}}(\hat{i}_{L2} - \frac{\hat{v}_{bat}}{R_{Load}}) \tag{5.4.3}$$

$$\dot{x} = \begin{bmatrix} \frac{-D_2R_{C_{o2}} - R_{L_2}}{L_2} & \frac{D_2}{L_2} & 0 \\ \frac{-D_2}{C_{i2}} & 0 & 0 \\ \frac{1}{C_{o2}} & 0 & 0 \end{bmatrix} \begin{bmatrix} \hat{i_{L2}} \\ \hat{v}_{Ci2} \\ \hat{v}_{Co2} \end{bmatrix} + \begin{bmatrix} \frac{D_2}{L_2} & \frac{-1}{L_2} & \frac{V_{Ci2}+R_{Ci2}(I_{in2}+I_{L2})}{L_2} \\ \frac{-D_2}{C_{i2}} & 0 & 0 \\ \frac{1}{C_{o2}} & 0 & 0 \end{bmatrix} \begin{bmatrix} \hat{I}_{in} \\ \hat{V}_{bat} \\ \delta_2 \end{bmatrix} \tag{5.4.4}$$

$$y = V_{in} = \begin{bmatrix} -R_{Ci2} & 1 & 0 \end{bmatrix} \begin{bmatrix} \hat{i_{L2}} \\ \hat{v}_{Ci2} \\ \hat{v}_{Co2} \end{bmatrix} + \begin{bmatrix} -R_{Co1} & 0 & 0 \end{bmatrix} \begin{bmatrix} \hat{I}_{in} \\ \hat{V}_{bat} \\ \delta_2 \end{bmatrix} \tag{5.4.5}$$

This results in the frequency response of $\frac{V_{in2}}{d_2}$ shown in figure 5.4.1. The difference with dc/dc1 is that now an additional 180° phase shift is introduced by the fact that increasing the duty cycle leads to decreasing the output (which is the input voltage of the converter). Therefor instead of a 90° increase in phase due to the ESR of the output capacitor, a decline of 90° is seen.

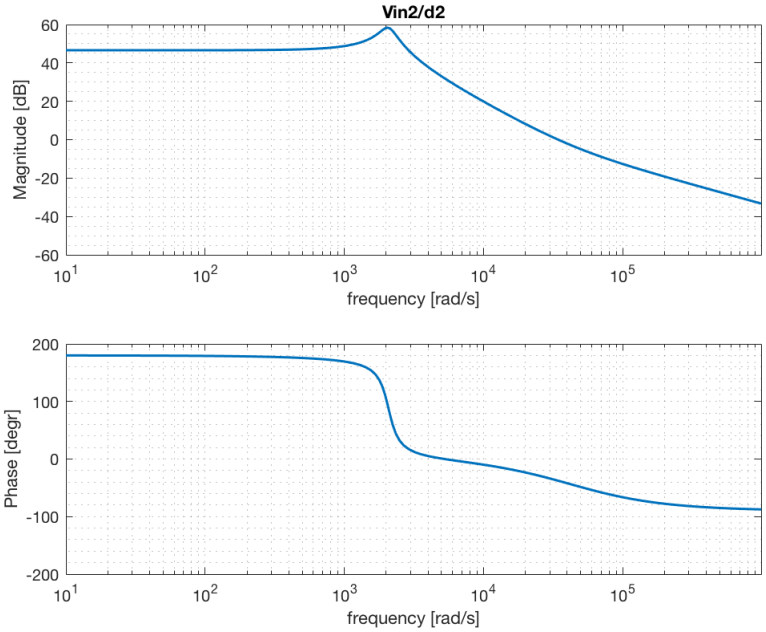

Figure 5.4.1: PLECS model

5.4.2 Boost

For the boost converter case, $V_{in} = V_{bat}$. Furthermore, for the V2G (boost) case equations (5.4.6-8) are obtained which result in the state space model of eq. (5.4.9) and eq. (5.4.10) and and the bode plot $\frac{V_{out}}{d_2}$ shown in Figure 5.4.2. Now that the output voltage of the converter is controlled, both the RHPZ and ESR zero can be seen in the figure.

$$\frac{d\hat{i}_{L_2}}{dt} = \frac{1}{L_2}(\hat{v}_{bat} - \hat{i}_{L2}R_{L2}) - \frac{1-d_2}{L_2}(\hat{v}_{C_{o2}} + R_c(\hat{i}_L - \hat{i}_{out2})) + \frac{\delta_2}{L_2}(V_{C_{o2}} + Rc(I_{L_2} - I_{out2}) \tag{5.4.6}$$

$$\frac{d\hat{v}_{C_{bat}}}{dt} = \frac{1}{R_c C_{bat}}(\hat{V}_{bat} - \hat{V}_{C_{bat}}) \tag{5.4.7}$$

$$\frac{d\hat{v}_{C_{o2}}}{dt} = \frac{1-d_2}{C_{o2}}(\hat{i}_L) - \frac{\delta)}{C_{o2}}(\hat{i}_L) - \frac{1}{C_{o2}}(\hat{i}_{out2}) \tag{5.4.8}$$

$$\dot{x} = \begin{bmatrix} \frac{-((1-D_2)R_{C_{o2}}+R_{L_2})}{L_2} & 0 & \frac{-1+D_2}{L_2} \\ 0 & \frac{-1}{R_{Ci2}C_{i2}} & 0 \\ \frac{1-D_2}{C_{o2}} & 0 & 0 \end{bmatrix} \begin{bmatrix} \hat{i_{L2}} \\ \hat{v}_{Ci2} \\ \hat{v}_{Co2} \end{bmatrix} + \begin{bmatrix} \frac{1}{L_2} & \frac{(1-D_2)R_{Co2}}{L_2} & \frac{V_{Co2}+R_{Ci2}(I_{L_2}-I_o ut)}{L_2} \\ \frac{1}{R_{Ci2}C_{i2}} & 0 & 0 \\ 0 & \frac{-1}{C_{o2}} & \frac{-I_{L2}}{C_{o2}} \end{bmatrix} \begin{bmatrix} \hat{I}_{in} \\ \hat{V}_{bat} \\ \delta_2 \end{bmatrix} \tag{5.4.9}$$

$$y = V_{in} = \begin{bmatrix} (1-D_2)R_{Ci2} & 0 & 1 \end{bmatrix} \begin{bmatrix} \hat{i_{L2}} \\ \hat{v}_{Ci2} \\ \hat{v}_{Co2} \end{bmatrix} + \begin{bmatrix} 0 & -R_{Co1} & 1 \end{bmatrix} \begin{bmatrix} \hat{I}_{in} \\ \hat{V}_{bat} \\ \delta_2 \end{bmatrix} \tag{5.4.10}$$

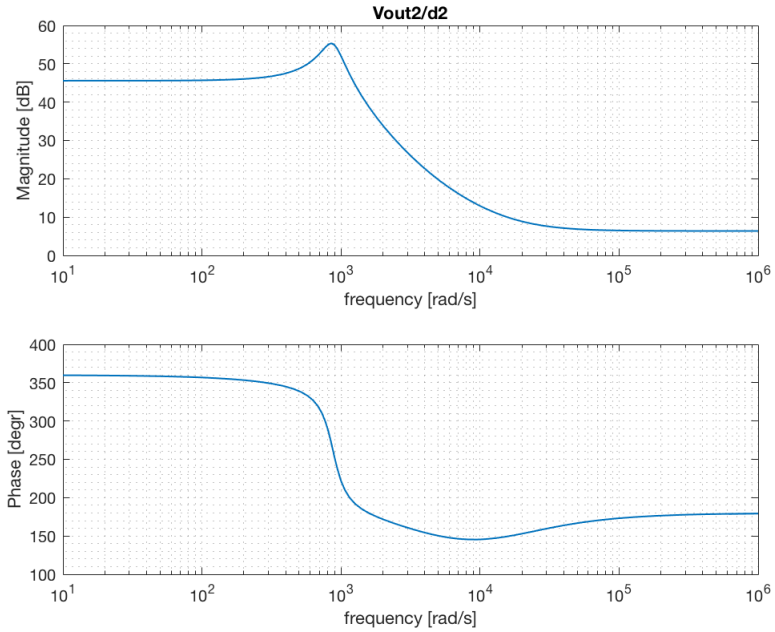

Figure 5.4.2: PLECS model

5.5 Complete Model

Finally, all three models are combined in order to make the small signal model of the whole system. This is done by equating the output of dc/dc1 to the input of the inductive link model, and equating the input of dc/dc2 to the output of the inductive link model. This complete model can then be used to determine the controller gains. As above, the G2V case will be discussed first.

5.5.1 Grid to Vehicle Power Transfer - Buck Mode

As said above the models can be combined by expressing the in/output variables ($I_{out,1}$ and $I_{in,2}$ in terms of state variables. Using Fourier analysis the DC link currents can be expressed in terms of the primary and secondary currents of the resonant tank. Furthermore, what is now $\hat{u}_{1,dc}$ was once $\hat{v}_{dc}$, which is an input to the system. Therefor the dynamics related to the change of input voltage, specified in the B matrix of the inductive link model, should also be incorporated in the model. For the G2V case this results in equations (5.5.1-5), the subscript 1 or 2 stand for dc/dc 1 or 2 respectively.

$$\hat{i}_{out,1} = \hat{i}_{dc,1} = \frac{\pi}{2\sqrt{2}}\hat{i}_P = \frac{\pi}{2\sqrt{2}}\left(\frac{I_{1s}}{I_p}\hat{i}_{1s} + \frac{I_{1c}}{I_p}\hat{i}_{1c}\right) \tag{5.5.1}$$

$$\hat{i}_{in,2} = \hat{i}_{dc,2} = \frac{\pi}{2\sqrt{2}}\hat{i}_S = \frac{\pi}{2\sqrt{2}}\left(\frac{I_{2s}}{I_S}\hat{i}_{2s} + \frac{I_{2c}}{I_S}\hat{i}_{2c}\right) \tag{5.5.2}$$

$$\frac{d\hat{i}_{1s}}{dt} = \Big(...\Big)x + \frac{4}{\pi L_{eq2}}\hat{u}_{1,dc} \tag{5.5.3}$$

$$\frac{d\hat{i}_{2s}}{dt} = \Big(...\Big)x + \frac{4}{\pi L_{eqm}}\hat{u}_{1,dc} \tag{5.5.4}$$

$$\hat{u}_{1,dc} = V_{Co1} + R_{Co1}(I_L 1 - I_P) \tag{5.5.5}$$

This results in the state space matrices A_{buck}, B_{buck}, C_{buck}, $\hat{x}$ and $\hat{u}$. Here the same matrix entries as in the inductive model are used.

$$A_{buck} = \begin{bmatrix} \frac{-R_c-R_{L1}}{L_p} & 0 & \frac{-1}{L_1} & \frac{\pi I_{1s} R_c}{2\sqrt{2}L_1 I_p} & \frac{\pi I_{1c} R_c}{2\sqrt{2}L_1 I_p} & 0 & 0 & 0 & 0 & 0 & 0 & 0 & 0 & 0 \\ 0 & \frac{-1}{R_c C_{grid}} & 0 & 0 & 0 & 0 & 0 & 0 & 0 & 0 & 0 & 0 & 0 & 0 \\ \frac{1}{C_{o1}} & 0 & 0 & \frac{-\pi I_{1s}}{2\sqrt{2}C_{o1} I_p} & \frac{\pi I_{1c}}{2\sqrt{2}C_{o1} I_p} & 0 & 0 & 0 & 0 & 0 & 0 & 0 & 0 & 0 \\ ;0 & 0 & \frac{4}{\pi L_{eq2}} & \frac{4R_c I_{1s}}{\pi L_{eq2} I_p} & \frac{(\Omega_s+4)R_c I_{1c}}{\pi L_{eq2} I_p} & -A13 & A14 & \frac{-1}{L_{eq2}} & 0 & \frac{-1}{L_{eqm}} & 0 & -A19 & 0 & 0 \\ 0 & 0 & 0 & -\Omega_s & 0 & A23 & -A24 & 0 & \frac{-1}{L_{eq2}} & 0 & \frac{-1}{L_{eqm}} & -A29 & 0 & 0 \\ 0 & 0 & \frac{4}{\pi L_{eqm}} & \frac{4R_c I_{1s}}{\pi L_{eqm} I_p} & \frac{4R_c I_{1c}}{\pi L_{eqm} I_p} & -A33 & \Omega_s + A34 & \frac{-1}{L_{eqm}} & 0 & \frac{-1}{L_{eq1}} & 0 & -A39 & 0 & 0 \\ 0 & 0 & 0 & 0 & 0 & \Omega_s + A43 & -A44 & 0 & \frac{-1}{L_{eqm}} & 0 & \frac{-1}{L_{eq1}} & -A49 & 0 & 0 \\ 0 & 0 & 0 & \frac{1}{C_1} & 0 & 0 & 0 & 0 & Ws & 0 & 0 & 0 & 0 & 0 \\ 0 & 0 & 0 & 0 & \frac{1}{C_1} & 0 & 0 & \Omega_s & 0 & 0 & 0 & 0 & 0 & 0 \\ 0 & 0 & 0 & 0 & 0 & \frac{1}{C_2} & 0 & 0 & 0 & 0 & \Omega_s & 0 & 0 & 0 \\ 0 & 0 & 0 & 0 & 0 & 0 & \frac{1}{C_2} & 0 & 0 & -\Omega_s & 0 & 0 & 0 & 0 \\ 0 & 0 & 0 & 0 & 0 & \frac{2I_{2s}}{\pi I_S C_f} & \frac{2I_{2c}}{\pi I_S C_f} & 0 & 0 & 0 & 0 & 0 & \frac{-d_2}{C_f} & 0 \\ 0 & 0 & 0 & 0 & 0 & \frac{\pi d_2 R_c I_{2s}}{2\sqrt{2} I_S L_2} & \frac{\pi d_2 R_c I_{2c}}{2\sqrt{2} I_S L_2} & 0 & 0 & 0 & 0 & \frac{d_2}{L_2} & \frac{-d_2 R_c - R_{L2}}{L_2} & 0 \\ 0 & 0 & 0 & 0 & 0 & 0 & 0 & 0 & 0 & 0 & 0 & 0 & \frac{1}{C_b at} & 0 \end{bmatrix} \tag{5.5.6}$$

$$B_{buck} = \begin{bmatrix} \frac{d_1}{L_1} & \frac{V_{grid}}{L_1} & 0 & 0 \\ \frac{1}{L_1} & 0 & 0 & 0 \\ 0 & 0 & 0 & 0 \\ 0 & 0 & 0 & 0 \\ 0 & 0 & 0 & 0 \\ 0 & 0 & 0 & 0 \\ 0 & 0 & 0 & 0 \\ 0 & 0 & 0 & 0 \\ 0 & 0 & 0 & 0 \\ 0 & 0 & 0 & 0 \\ 0 & 0 & 0 & 0 \\ 0 & 0 & 0 & \frac{-I_{L2}}{C_f} \\ 0 & 0 & \frac{-1}{L_2} & \frac{V_{Cf} + R_c(\frac{2}{\pi} I_S - I_{L2})}{L_2} \\ 0 & 0 & \frac{-1}{R_L C_{bat}} & 0 \end{bmatrix} \tag{5.5.7}$$

$$C_{buck} = \begin{bmatrix} R_c & 0 & 1 & \frac{-R_c I_{1s}}{I_P} & \frac{-R_c I_{1c}}{I_p} & 0 & 0 & 0 & 0 & 0 & 0 & 0 & 0 \\ 0 & 0 & 0 & 0 & 0 & \frac{2R_c I_{2s}}{\pi I_S} & \frac{2R_c I_{2c}}{\pi I_S} & 0 & 0 & 0 & 0 & 1 & -R_c & 0 \end{bmatrix} \tag{5.5.8}$$

$$D_{buck} = 0 \tag{5.5.9}$$

$$\hat{x} = \begin{bmatrix} \hat{i}_{L1} & \hat{v}_{Cgrid} & \hat{v}_{Co1} & \hat{i}_{1s} & \hat{i}_{1c} & \hat{i}_{2s} & \hat{i}_{2c} & \hat{v}_{1s} & \hat{v}_{1c} & \hat{v}_{2s} & \hat{v}_{2c} & \hat{v}_{Co2} & \hat{i}_{L2} & \hat{v}_{Cbat} \end{bmatrix}^T \tag{5.5.10}$$

$$\hat{u} = \begin{bmatrix} \hat{v}_{grid} & \delta_1 & \hat{v}_{bat} & \delta_2 \end{bmatrix} \tag{5.5.11}$$

Using the matrices given in eq. (5.5.6-9) the frequency response for $\frac{V_{out1}}{\delta_1}$ and $\frac{V_{out2}}{\delta_2}$ can be determined. The results of this are shown in Figure 5.5.1. The results are similar to bode plots of buck converter in continuous conduction mode (CCM). Unfortunately, doing a frequency sweep over the plecs model results in unusable results with mostly NaN's.

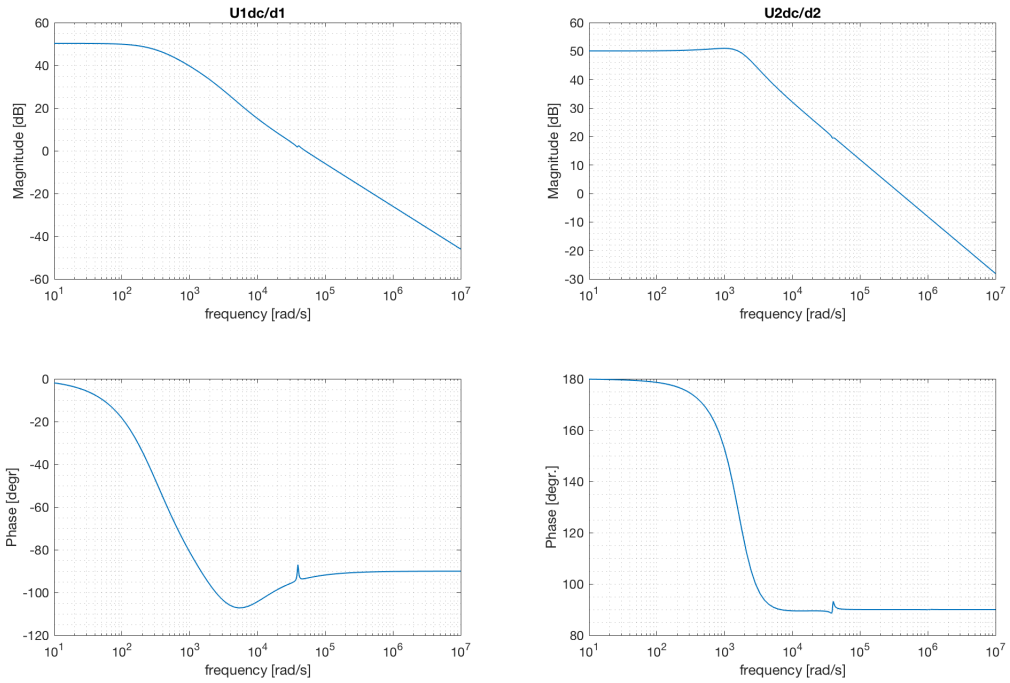

Figure 5.5.1: frequency response for $\frac{V_{out1}}{\delta_1}$ and $\frac{V_{out2}}{\delta_2}$

5.5.2 Vehicle to Grid Power Transfer - Boost Mode

For the V2G case , eq. (5.5..12-16) are used to equate the in- and outputs. This results in the matrices and vectors given in equation (5.5.17-22). The bode plot of this state space system is shown in Figures 5.5.2-3. The results for $U_{1,dc}$ are similar to the bode plot a boost converter of which the input voltage is controlled, however there are some deviations due to the inductive link model. The same holds for $U_{2,dc}$, the phase drops below zero for at higher frequencies, possibly due to the RHPZ. However the exact dynamics are now very hard to tell from the bode plots, since it is comprised of multiple models. Again a frequency sweep in Plecs resulted in inaccurate results.

$$\hat{i}_{in,1} = \hat{i}_{dc,1} = \frac{\pi}{2\sqrt{2}}\hat{i}_S = \frac{\pi}{2\sqrt{2}}\left(\frac{I_{ss}}{I_S}\hat{i}_{ss} + \frac{I_{sc}}{I_S}\hat{i}_{sc}\right) \tag{5.5.12}$$

$$\hat{i}_{out,2} = \hat{i}_{dc,2} = \frac{\pi}{2\sqrt{2}}\hat{i}_P = \frac{\pi}{2\sqrt{2}}\left(\frac{I_{ps}}{I_P}\hat{i}_{ps} + \frac{I_{pc}}{I_P}\hat{i}_{pc}\right) \tag{5.5.13}$$

$$\frac{d\hat{i}_{ps}}{dt} = \Big(...\Big)x + \frac{4}{\pi L_{eq2}}\hat{u}_{2,dc} \tag{5.5.14}$$

$$\frac{d\hat{i}_{ss}}{dt} = \Big(...\Big)x + \frac{4}{\pi L_{eqm}}\hat{u}_{2,dc} \tag{5.5.15}$$

where,

$$\hat{u}_{2,dc} = V_{Co2} + R_{Co2}((1-D_2)I_{L2} - I_P) \tag{5.5.16}$$

$$A_{boost} = \begin{bmatrix} \frac{-(1-d_2)R_c-R_{L2}}{L_s} & 0 & \frac{-(1-d_2)}{L_2} & \frac{(1-d2)R_{Co1}\pi I_{1s}}{2\sqrt{2}L_2 I_p} & \frac{(1-d2)R_{Co1}\pi I_{1s}}{2\sqrt{2}L_2 I_p} & 0 & 0 & 0 & 0 & 0 & 0 & 0 & 0 & \\ 0 & \frac{-1}{R_{Cbat}C_{bat}} & 0 & 0 & 00 & 0 & 0 & 0 & 0 & 0 & 0 & 0 & 0 & \\ \frac{1-d_2}{C_{o2}} & 0 & 0 & \frac{-(\pi I_{1s})}{2\sqrt{2}C_{o2}I_p} & \frac{-(\pi I_{1c})}{2\sqrt{2}C_{o2}I_p} & 0 & 0 & 0 & 0 & 0 & 0 & 0 & 0 & 0 \\ \frac{4(1-d_2)R_{Co1}}{\pi L_{eqm}} & 0 & \frac{4}{\pi L_{eq2}} & \frac{-4R_c I_{1s}}{\pi L_{eq2} I_p} & \frac{(\Omega_s+4)R_c I_{1c}}{\pi L_{eq2} I_p} & -A13 & A14 & \frac{-1}{L_{eq2}} & 0 & \frac{-1}{L_{eqm}} & 0 & -A19 & 0 & 0 \\ \frac{4(1-d_2)R_{Co1}}{\pi L_{eqm}} & 0 & 0 & -\Omega_s & 0 & A23 & -A24 & 0 & \frac{-1}{L_{eq2}} & 0 & \frac{-1}{L_{eqm}} & -A29 & 0 & 0 \\ 0 & 0 & \frac{4}{\pi L_{eqm}} & \frac{4R_c I_{1s}}{\pi L_{eqm} I_p} & \frac{4R_c I_{1c}}{\pi L_{eqm} I_p} & -A33 & \Omega_s + A34 & \frac{-1}{L_{eqm}} & 0 & \frac{-1}{L_{eq1}} & 0 & -A39 & 0 & 0 \\ 0 & 0 & 0 & 0 & 0 & \Omega_s + A43 & -A44 & 0 & \frac{-1}{L_{eqm}} & 0 & \frac{-1}{L_{eq1}} & -A49 & 0 & 0 \\ 0 & 0 & 0 & \frac{1}{C_1} & 0 & 0 & 0 & 0 & Ws & 0 & 0 & 0 & 0 & 0 \\ 0 & 0 & 0 & 0 & \frac{1}{C_1} & 0 & 0 & \Omega_s & 0 & 0 & 0 & 0 & 0 & 0 \\ 0 & 0 & 0 & 0 & 0 & \frac{1}{C_2} & 0 & 0 & 0 & 0 & \Omega_s & 0 & 0 & 0 \\ 0 & 0 & 0 & 0 & 0 & 0 & \frac{1}{C_2} & 0 & 0 & -\Omega_s & 0 & 0 & 0 & 0 \\ 0 & 0 & 0 & \frac{2R_c I_{1s}}{\pi I_p L_2} & frac2(1-d2)R_c I_{1c}\pi I_p L_2 & 0 & 0 & 0 & 0 & 0 & 0 & \frac{-(1-d2)R_c+R_{L2}}{L_2} & 0 & \frac{-1-d2}{L_2} \\ 0 & 0 & 0 & 0 & 0 & 0 & 0 & 0 & 0 & 0 & 0 & 0 & \frac{-1}{R_c C_{bat}} & 0 \\ 0 & 0 & 0 & \frac{-2I_{1s}}{\pi I_p C_{o2}} & \frac{-2I_{1c}}{\pi I_p C_{o2}} & 0 & 0 & 0 & 0 & 0 & 0 & \frac{1-d_2}{C_{o2}} & 0 & 0 \end{bmatrix} \tag{5.5.17}$$

$$B_{boost} = \begin{bmatrix} \frac{1}{L_2} & \frac{V_{Co2}+R_{Co2}(I_{L2}-I_S}{L_2} & 0 & 0 \\ \frac{1}{R_{Cbat}C_{bat}} & 0 & 0 & 0 \\ 0 & \frac{-I_{L2}}{C_{o2}} & 0 & 0 \\ 0 & 0 & 0 & 0 \\ 0 & 0 & 0 & 0 \\ 0 & 0 & 0 & 0 \\ 0 & 0 & 0 & 0 \\ 0 & 0 & 0 & 0 \\ 0 & 0 & 0 & 0 \\ 0 & 0 & 0 & 0 \\ 0 & 0 & 0 & 0 \\ 0 & 0 & 0 & 0 \\ 0 & 0 & \frac{1-d_1}{L_1} & \frac{V_{grid}}{L_1} \\ 0 & 0 & \frac{-1}{R_{grid}C_{grid}} & 0 \end{bmatrix} \tag{5.5.18}$$

$$C_{boost} = \begin{bmatrix} (1-d_2)R_c & 0 & 1 & 0 & \frac{-\pi R_c I_{1s}}{2\sqrt{2}I_p} & \frac{-\pi R_c I_{1c}}{2\sqrt{2}I_p} & 0 & 0 & 0 & 0 & 0 & 0 & 0 & 0 \\ 0 & 0 & 0 & 0 & 0 & \frac{\pi R_c I_{2s}}{2\sqrt{2}I_S} & \frac{\pi R_c I_{2c}}{2\sqrt{2}I_S} & 0 & 0 & 0 & 0 & 1 & -Rc & 0 \end{bmatrix} \tag{5.5.19}$$

$$D_{boost} = 0 \tag{5.5.20}$$

$$\hat{x} = \begin{bmatrix} \hat{i}_{L1} & \hat{v}_{Cgrid} & \hat{v}_{Co1} & \hat{i}_{1s} & \hat{i}_{1c} & \hat{i}_{2s} & \hat{i}_{2c} & \hat{v}_{1s} & \hat{v}_{1c} & \hat{v}_{2s} & \hat{v}_{2c} & \hat{v}_{Co2} & \hat{i}_{L2} & \hat{v}_{Cbat} \end{bmatrix}^T \tag{5.5.21}$$

$$\hat{u} = \begin{bmatrix} \hat{v}_{grid} & \delta_1 & \hat{v}_{bat} & \delta_2 \end{bmatrix} \tag{5.5.22}$$

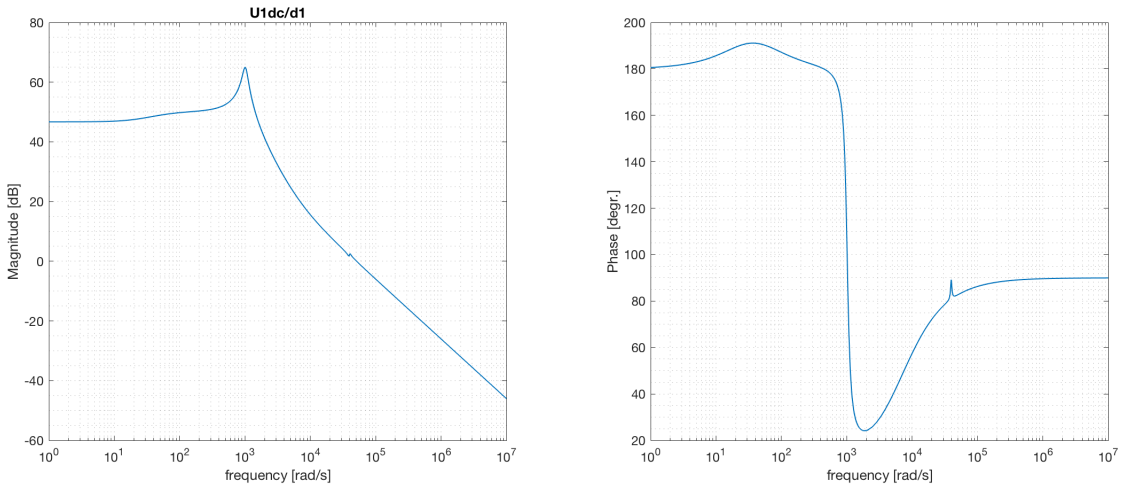

Figure 5.5.2: frequency response for $\frac{V_{out1}}{\delta_1}$

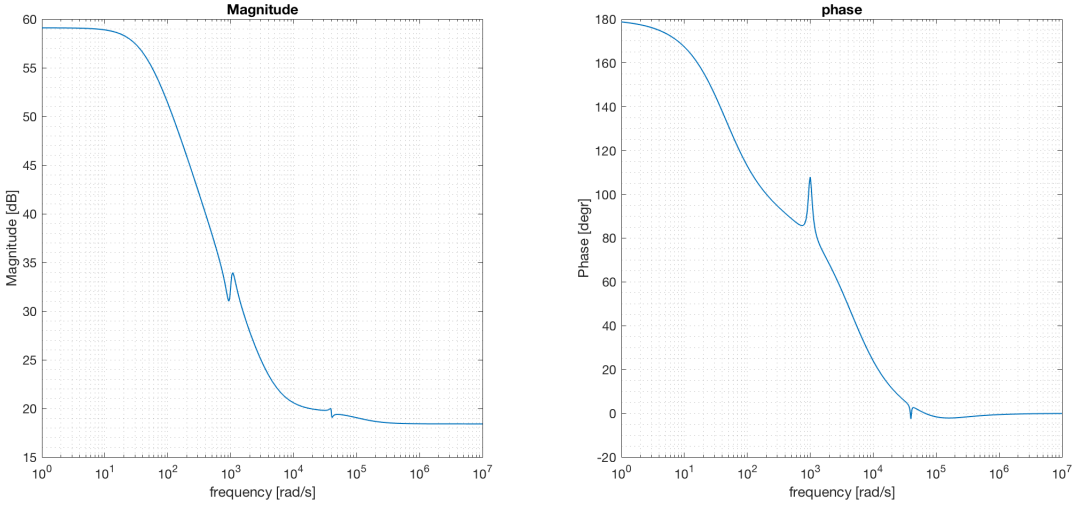

Figure 5.5.3: frequency response for and $\frac{V_{out2}}{\delta_2}$

5.6 Conclusion

In this chapter a dynamic model of the proposed bidirectional setup was made. Output of these models are the control to dc link voltage frequency response. From this the phase and gain margins of the system can be determined and using these margins the gains of the voltage controllers can be determined. The design of these controllers will be discussed in the next chapter.

CHAPTER 6

CONTROLLER DESIGN

6.1 INTRODUCTION

In the previous chapter the control to DC link voltages frequency response was determined. Fro m this voltage controller gains can be determined and this will be discussed in this chapter. Figure 6.1.1. shows an overview of the overall control scheme. In total three different controllers were designed: two voltage controllers and one for resonance tracking. For the resonance tracker it was not possible to design the controller based on analytical models, and was therefore tuned by hand in the lab and will thus not be discussed in chapter. The implementation of this controller in simulink can be found in Appendix H. The design of the voltage controllers is discussed in next two sections.

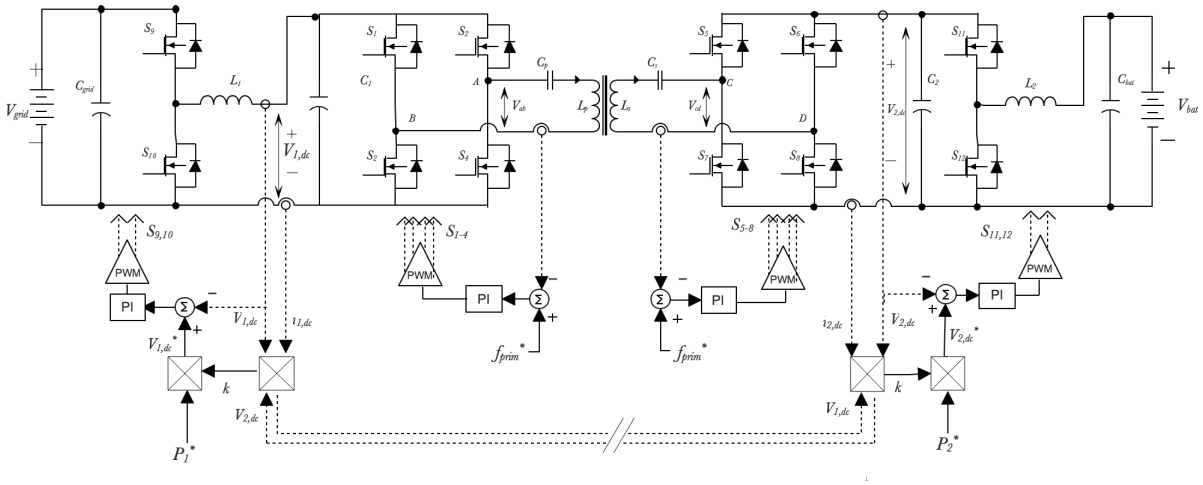

Figure 6.1.1: Complete inductive power transfer system

For the voltage controllers, both controllers are given the setpoint for the output power. Then after determining the coupling factor as discussed in Chapter 4 section 1, the dc link voltages $U_{1,dc}$ and $U_{2,dc}$ can be determined according to eq. (4.2.9) and (4.3.2) respectively. In order to avoid interference between the controllers, the resonance tracking controllers should be the fasted controller, then MPPT should be performed and finally the power should be controlled to the desired setpoint. This is shown in the flowchart in Figure 6.1.2.

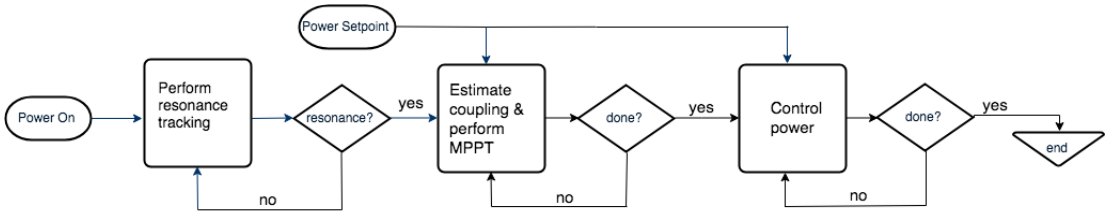

Figure 6.1.2: Control scheme flowchart

6.2 Buck Controller Design

Based on the output voltages and current, the coupling is estimated and used to calculate the reference voltage, as explained in Chapter 4. In the previous chapter the frequency response of the entire system is determined, using the derived bode plots the controller gains can be determined. In this section the buck converter controller is discussed and therefor the bode plots of Figure 5.5.1 are needed (Since the design process is equal for both dc/dc converters they will be discussed simultaneously) For both dc/dc 1 and 2 it can be seen that the frequency response below 200 rad/s and 2 krad/s respectively, has a slope of 0 dB/dec and because the in- and output of the converters are DC, it means that a type 1 PI controller can be used [11]. Therefor the controller transfer function has the following form:

$$C(s) = K\frac{1+\tau s}{\tau s} \tag{6.2.1}$$

Here K is the controller gain and τ is the time constant of the controller. In order to determine these values the gain margin, phase margin and bandwidth of the controller have to be determined. To keep the controller as fast as possible the cross over frequencies/bandwidths are chosen as high as possible while still being on the 0 dB/dec slope, resulting in: $\omega_{c1} = 200$ rad/s and $\omega_{c2} = 2000$ rad/s. The larger bandwidth for dc/dc 2 coincides with the idea that the impedance matching controller should be faster than the power controller in order to avoid interference between the controllers (Also an additional delay is implemented to make sure that the controllers don't interfere).
A closed loop phase margin of 60 degrees is selected for both controllers such that the system is critically damped [29]. The phase margin is defined as

$$PM_{CL} = 360^\circ - \angle\phi_{loop} \tag{6.2.2}$$

Here ϕ_{loop} is the loop phase delay. However since a negative feedback loop is used, which induces a phase shift 180°, the closed loop system is only allowed to have a phase shift of 120° in order for the system to be critically damped [29]. To achieve this the controller has to give a phase lead of [11]:

$$\phi = PM_{CL} - (180^\circ + \angle H_p(f_c)) \tag{6.2.3}$$

For dc/dc 1 ($\angle H_{p1}(f_c)) = -35^\circ$ this gives a phase lead of -95°, for dc/dc 2 ($\angle H_{p2}(f_c)) = 117^\circ$) the phase lead equals -237° or $-237^\circ + 360^\circ = 123^\circ$ since phase has a circular characteristic [30]. The required phase boost for each converter equals $\phi + 90$ [11], which equals 55° and -147° for dc/dc 1 and 2 respectively. From the phase lead τ can be determined according to:

$$\tau = \frac{tan(\phi + 90^\circ)}{\omega_c} \tag{6.2.4}$$

This results in $\tau_1 = 0.0071$ and $\tau_2 = 8.0017x10^{-4}$. The final thing to do is to determine the gain K. K is determined by the fact that the closed loop system should have a 0 dB magnitude at its cross over frequency. Therefore:

$$20\log(H_p) = -20\log(H_c) \Rightarrow H_c = 10^{-\log(H_p(f_c))} \tag{6.2.5}$$

Here $20\log(H_p)$ is the gain of the plant at the crossover frequency, this results in the controller parameter values given in table 6.2.1. $K_1 = 10^{50/-20} = 0.0032$ and $K_1 = 10^{50/-20} = 0.0032$. The closed loop bode plots are shown in figure 6.2.1, which show the cut off frequencies at 200 and 2000 rad/s.

Table 6.2.1: Buck mode controller gains

Symbol	Quantity	Value
K_1	Controller 1 gain	0.0032
τ_1	Controller 1 time constant	0.0071
K_2	Controller 2 gain	0.0032
τ_2	Controller 2 time constant	$8.0017x10^{-4}$

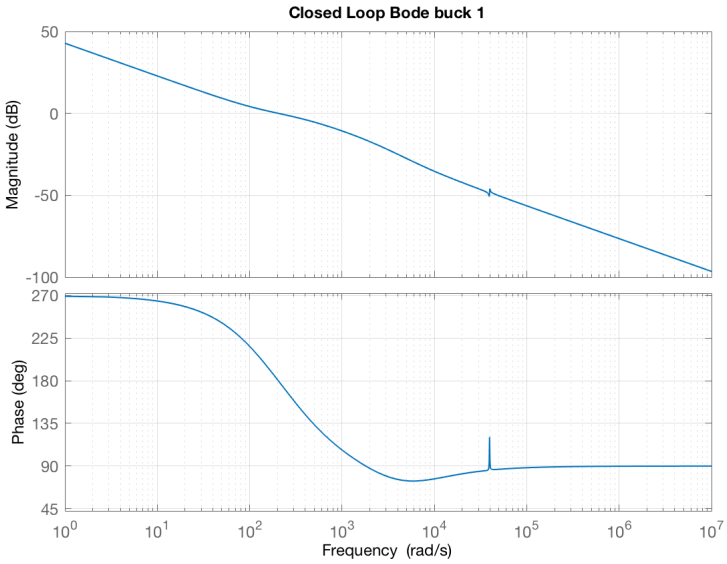

Figure 6.2.1: $\frac{V_{out,1}}{d_1}$ for dc/dc 1

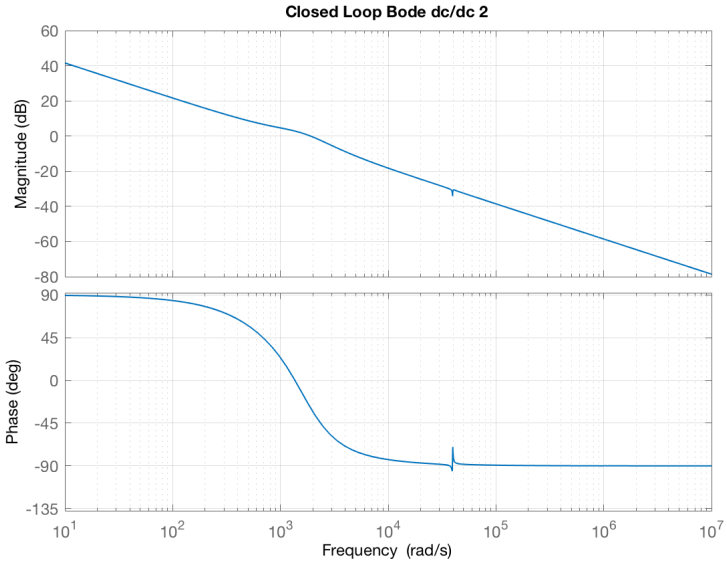

Figure 6.2.2: $\frac{V_{in,2}}{d_2}$ for dc/dc 2

Figures 6.2.3 and 6.2.4 show the closed resonse of the controller for 10V voltage step, implemented in the

simulink file of Appendix B. As can be seen the response is fast and without a large overshoot or oscillations.

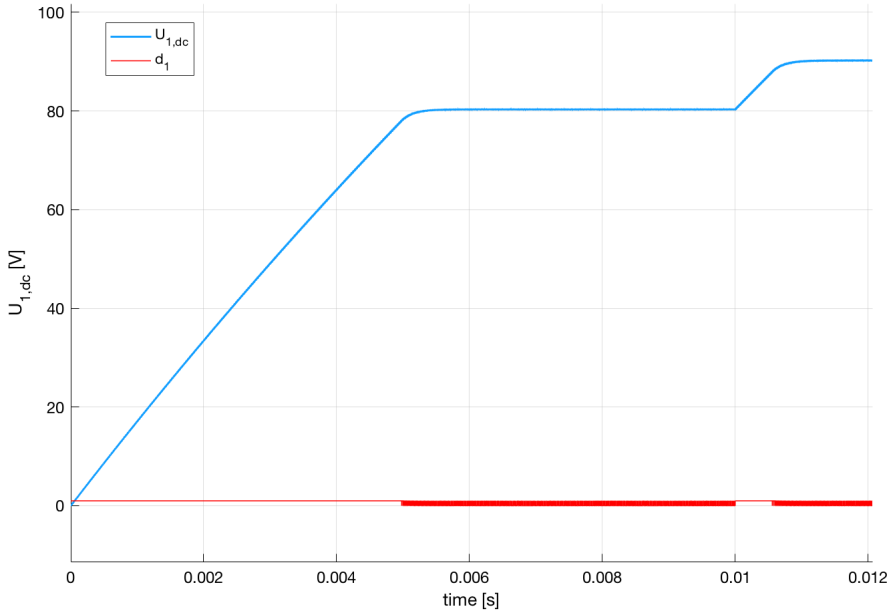

Figure 6.2.3: $V_{dc,1}$ response

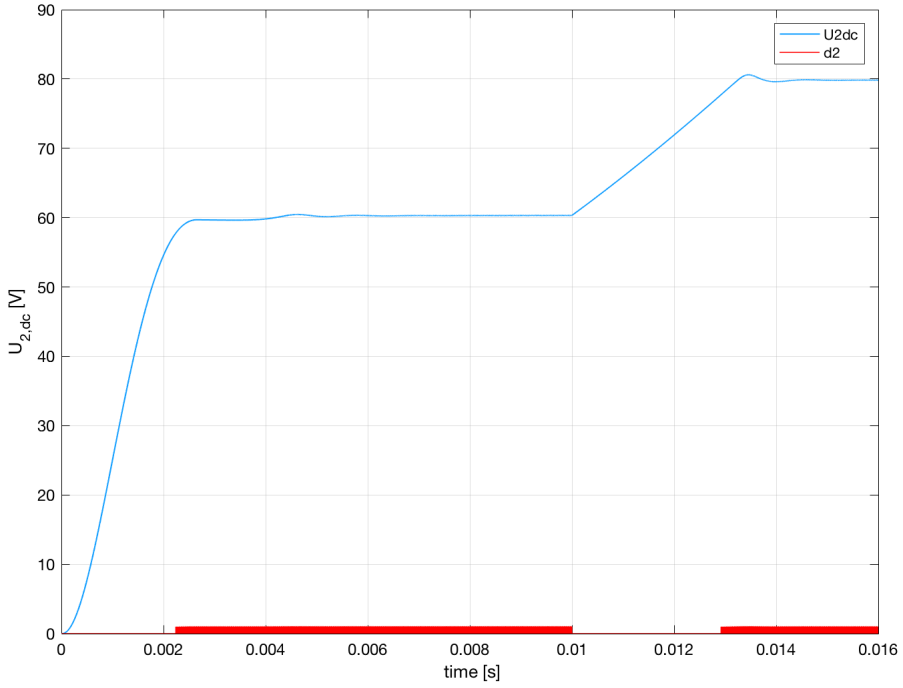

Figure 6.2.4: $V_{dc,2}$ response

6.3 Boost Controller Design

Next the design of the boost controller will be discussed. The approach is exactly the same as for the buck converter and will therefore be discussed more briefly. The design of the boost controllers are based on the bode plots shown in Figure 5.5.2-3. From these it is clear that again a Type 1 PI controller can be used, using the transfer function given in equation (6.2.1). Next the bandwidths of the controllers are chosen at 400

rad/s and 45 rad/s for dc/dc 1 and dc/dc2 respectively.
Now equation (6.2.3) is again used to determine the phase lead of the controller, using $\angle H_{p1}(f_c)) = 133°$ and $\angle H_{p2}(f_c)) = 182°$. The resulting loop phase delays are given in eq. (6.3.4) and (6.3.4).

$$\phi_1 = 60 - (180° + 133°) = 107° \tag{6.3.1}$$

$$\phi_2 = 60 - (180° + 182°) = -58° \tag{6.3.2}$$

This results in the following time constants:

$$\tau_1 = \frac{\tan(\phi_1 + 90)}{\omega_c} = 7.64 * 10^{-4} \tag{6.3.3}$$

$$\tau_2 = \frac{\tan(\phi_2 + 90)}{\omega_c} = 0.013 \tag{6.3.4}$$

Then using eq. (6.2.5), the gains are determined. Again the gains are chosen such that the gain is zero at the crossover frequency. Resulting in:

$$K_{c1,boost} = 10^{20\log(H_p(f_c1))/-20} = 3.16 * 10^{-3} \tag{6.3.5}$$

$$K_{c2,boost} = 10^{20\log(H_p(f_c2))/-20} = 5.623 * 10^{-3} \tag{6.3.6}$$

Using these controller parameters, the closed loop bode plots for $\frac{V_{in,1}}{d_1}$ and $\frac{V_{out,2}}{d_2}$ are shown in Figure 6.3.1 and 6.3.2, with the controller parameters given in table. Again it can be seen that a gain of 0 dB has been achieved at the cross over frequencies.

Symbol	Quantity	Value
K_1	Controller 1 gain	$3.16 * 10^{-3}$
τ_1	Controller 1 time constant	$7.64 * 10^{-4}$
K_2	Controller 2 gain	0.013
τ_2	Controller 2 time constant	$5.623 * 10^{-3}$

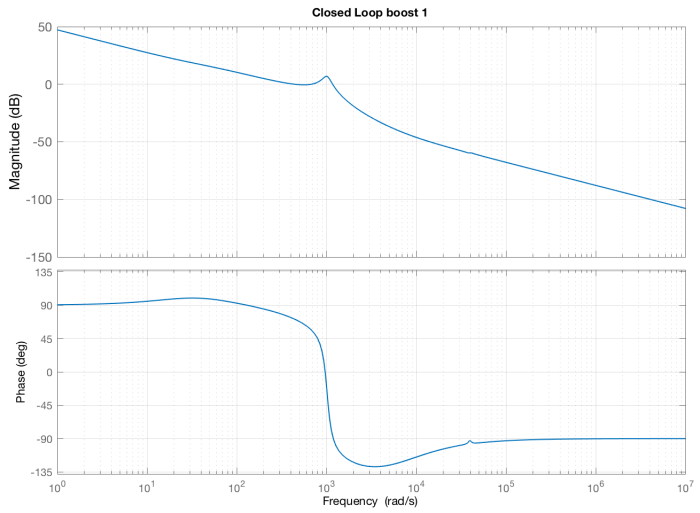

Figure 6.3.1: $\frac{V_{in,1}}{d_1}$ for dc/dc 1

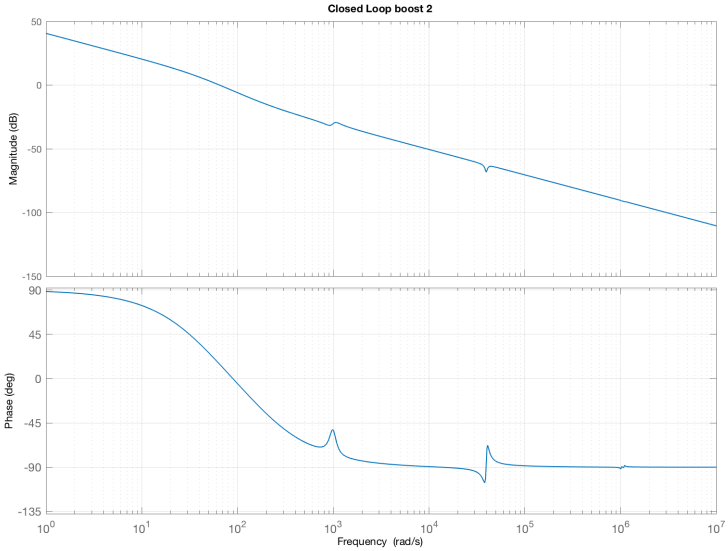

Figure 6.3.2: $\frac{V_{out,2}}{d_2}$ for dc/dc 2

Figures 6.3.3 and 6.3.4 show the closed resonse of the controllers for 10V voltage step in boost mode. The response of $U_{1,dc}$ is nicely fast and clean. However the response of $U_{2,dc}$ shows some oscillations. This could be due to a mistake in the model, however decreasing the gains does not seem to improve these oscillations and only causes large overshoots and slow response. Therefor this response is accepted.

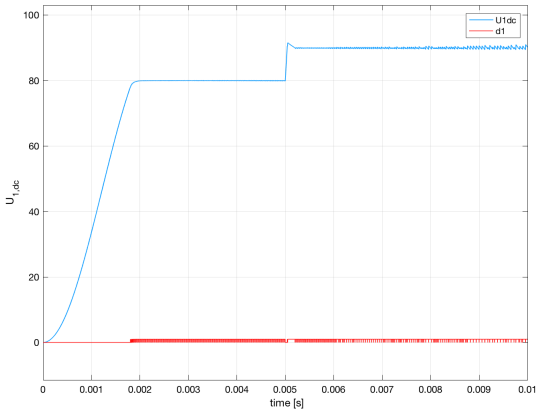

Figure 6.3.3: $U_{1,dc}$ closed loop response

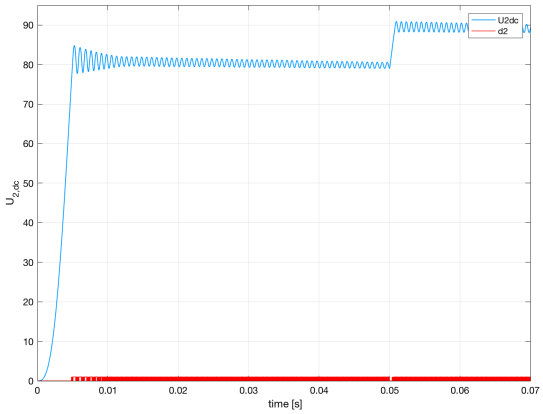

Figure 6.3.4: $U_{2,dc}$ closed loop response

6.4 Conclusion

The design of the voltage controllers concludes the design of the control loop. Next this control system will be build on an experimental setup and the results will be discussed in the next chapter.

CHAPTER 7

EXPERIMENTAL RESULTS

7.1 INTRODUCTION

In the previous chapter the voltage controller gains were determined. This concludes the design of the misalignment tolerant control scheme (besides the frequency controller gains). Now the setup given in Figure 6.1.1. was build in the lab, Figure 7.1.1. shows a picture of the prototype setup. In this chapter the results of the MEPT control scheme, coupling factor estimation and implementation of the resonance tracker are shown. Unfortunately, due to lack of time the system was not tested in boost mode. Therefor all the results discussed below are in G2V power transfer mode.

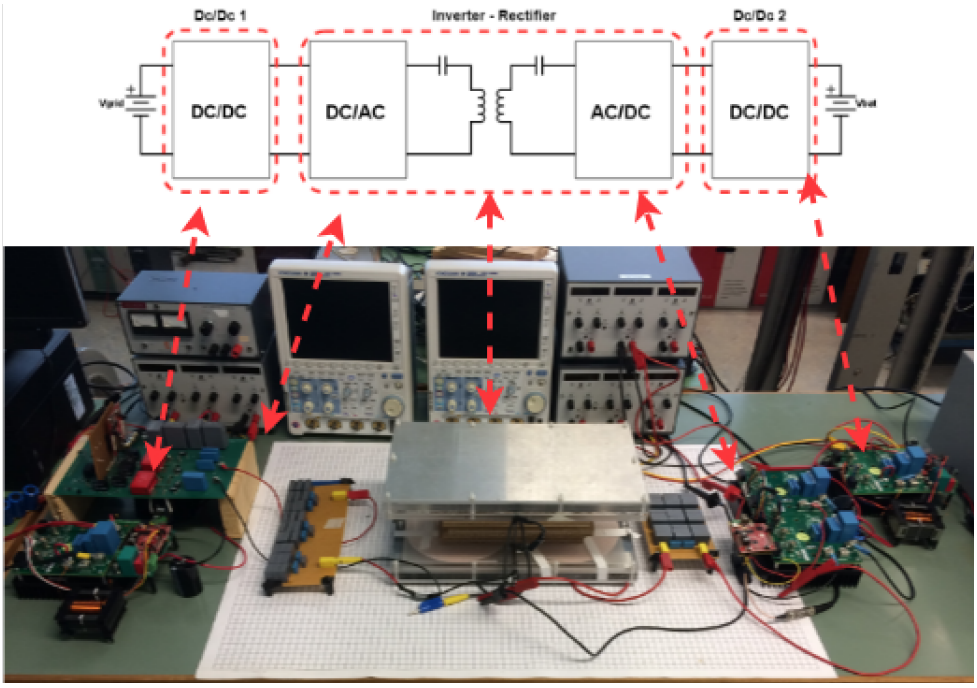

Figure 7.1.1: Lab prototype of the proposed setup.

7.2 Maximum Efficiency Point Tracking

In this section the results from the MEPT control scheme implemented on the secondary side dc/dc converter is discussed. This converter estimates the coupling as discussed in section 4.6.2. and determines the voltage setpoint. Figure 6.1.1. shows the result of this for multiple misalignments. During this test the resonance is tracked manually in order to avoid interference between the controllers. For a detailed calculation of the losses, see Appendix G.

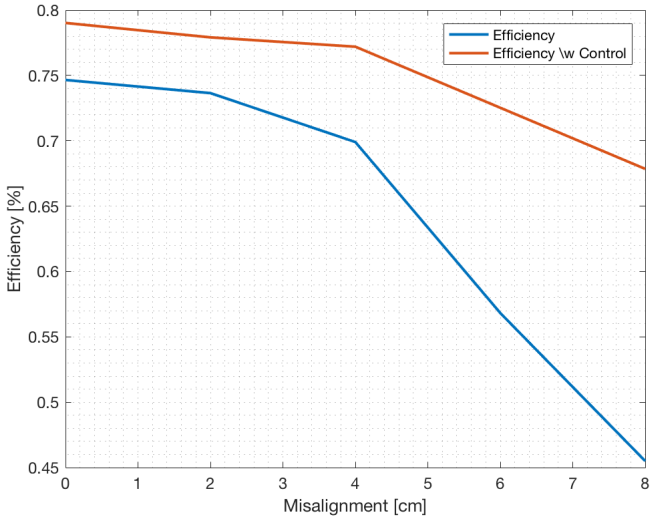

Figure 7.2.1: U_{1dc} to U_{out} efficiency

Figure 7.2.1. shows the U_{1dc} to output efficiency for 0, 2, 4, 6 and 8 cm misalignment, with and without control. For the case without control, the output of the rectifier is directly connected to the electronic load at 48V at an output power of 300W. For the case with control, the efficiency is measured after the dc/dc converter, therefor these efficiencies include the losses of the converter. It can be seen that the control gives a large improvement in efficiency, from 5% increases under perfect alignment up to 23% increase under 8 cm misalignment. The increase in efficiency increases for larger misalignment since, the efficiency vs. $U_{2,dc}$ curve gets sharper for decreasing coupling (see Figure 4.2.3). Because of this a small change in $U_{2,dc}$ results in a big change in efficiency, while for higher coupling this curve is more flat and therefor a deviation from the MEPT voltage is less drastic. Table 7.2.1. shows the values of the dc link voltages and currents needed to obtain an output power of 300W with and without control. Furthermore, Figures 7.2.2 show the resonant tank voltages and currents with and without control for 0, 4 and 8 cm misalignment.

Table 7.2.1: IPT system specifications

Parameter	0 cm	2 cm	4 cm	6 cm	8cm
$U_{1,dc}$	125 V	118 V	103 V	81 V	58 V
$U_{1,dc}$ w. control	89 V	89 V	82 V	77 V	54 V
$U_{2,dc}$	48 V	48 V	48 V	48 V	48 V
$U_{2,dc}$ w. control	76 V	71 V	66 V	59.7 V	58 V
$I_{1,dc}$	3.22 A	3.43 A	4.2 A	6.57 A	11.57 A
$I_{1,dc}$ w. control	4.39	4.35	4.61	5.75	8.45
$I_{2,dc}$	6.26 A	6.21 A	6.3 A	6.3 A	6.46 A
$I_{2,dc}$ w. control	6.41 A	6.27 A	6.05 A	6.715	6.45

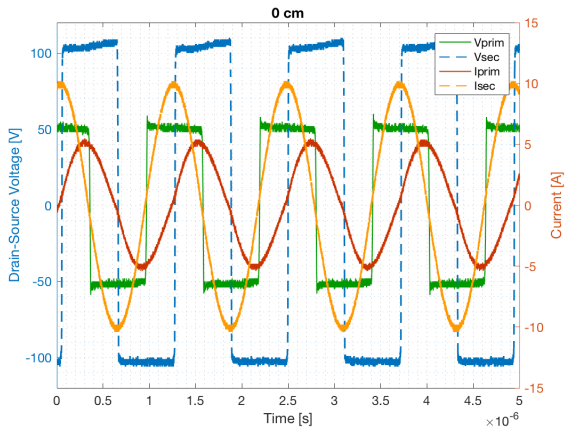

(a) without control

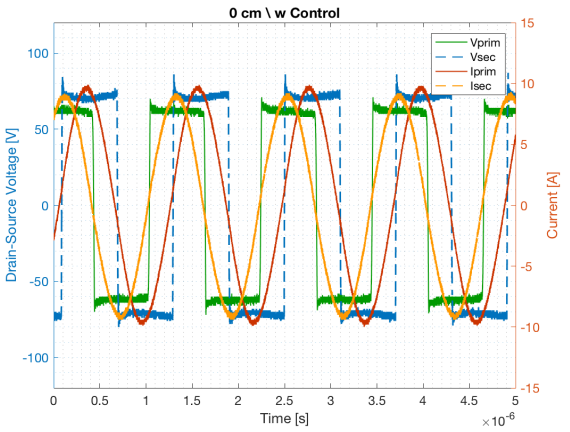

(b) with control

Figure 7.2.2: 0 cm misalignment

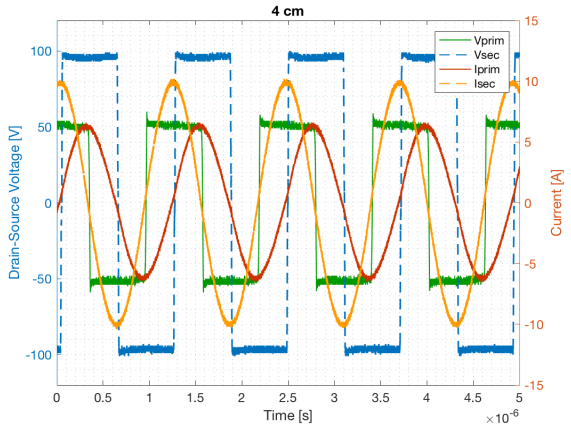

(a) without control

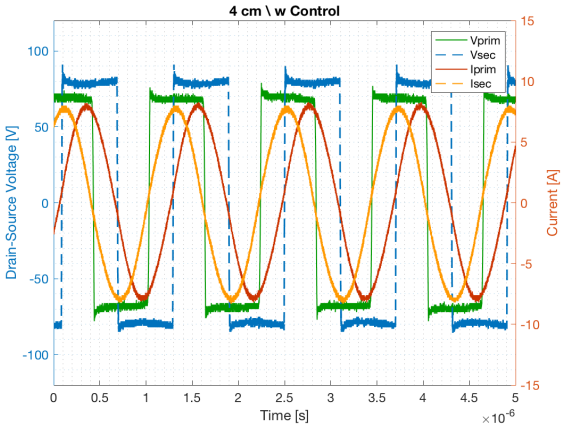

(b) with control

Figure 7.2.3: 4 cm misalignment

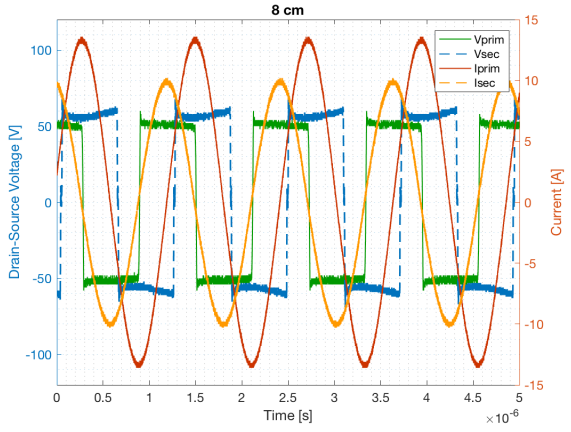

(a) without control

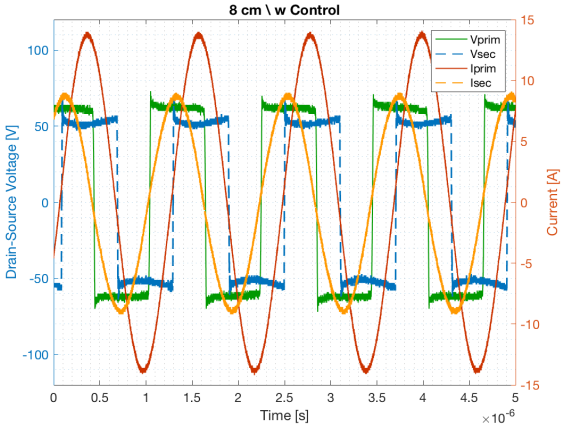

(b) with control

Figure 7.2.4: 8 cm misalignment

7.3 Coupling Factor Estimation

In this section the online coupling factor estimation is discussed. Here voltage and current measurement circuits are combined with a microcontroller integrated on the converter to estimate the coupling. The measurement circuits used for this are shown in Appendix F, the microcontroller used is a TI C2000 Launchpad. This controller board was chosen because of its ease of implementation (the board can be connected using two 2x10 header pins, also simulink models can be flashed onto the controller eliminating the need for writing code). The simulink files which are used are given in Appendix H.

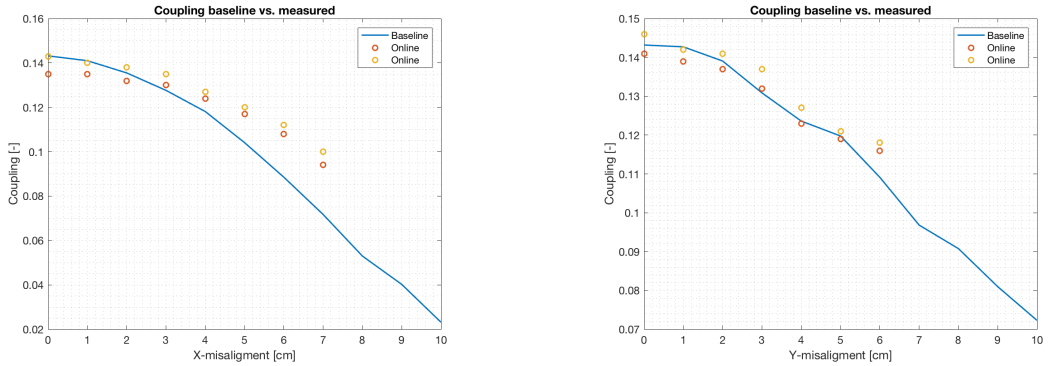

(a) X-displacement versus coupling factor, y = 0.

(b) Y-displacement versus coupling factor, x = 0.

Figure 7.3.1: Individual effect of displacement in the x- and y-direction.

The results of the online measurements are shown in Figures 7.3.1a-b, under x and y displacement respectively. Here the red and yellow circles represent the upper and lower bound of the estimated coupling. This variation is caused by jitter and noise in the voltage and current measurements. To minimize this effect the estimations were averaged (see simulink model), however this does not fully cancel out this effect. A better solution for this is to use a recursive least squares (RLS) filter, such as the filter described in [13]. However due to time limitations this was not implemented. From the figures it can be seen that for large misalignments in the x-direction the estimation error increases, this is due to the change in self inductance which is changing the resonance frequency, and was not adapted for during the measurements.

7.3.1 Resonant Tracker

For the implementation of the resonance tracker, the phase detection circuit of Figure 4.6.2 (section 4.6) is implemented on a PCB and combined with a microcontroller board (TI C2000). The layout of this PCB can be found in Appendix F. Figure 7.3.2a-b. show the experimental results of the resonance tracker. Here the yellow waveform is the actual current measured using a 100MHz probe. From this it can be seen that the delay between the current and the comparator output voltage is negligible (which is needed in order for the circuit to operate accurately). Furthermore it can be seen that the resonance tracking circuit operates as simulated. Now that the phase is detected accurately, the next step of the resonance tracker is controlling the phase to a desired value. This is done by changing the switching frequency of the inverter using a PI controller implemented on the microcontroller of the inverter. This microcontroller controls the DC output voltage of the phase detection circuit to a reference of 1.7V. This reference corresponds to a phase of 180° and was determined experimentally to be the voltage where ZVS occurs under a 300W load (However this does not vary much under different loads).
Next, the gains of the controller have to be determined. Since this can not be based on an analytical model, the gains are determined experimentally in such a way that the tracking is as fast as possible without having oscillations in the frequency. This resulted in gains of $K_p = 3$ and $K_i = 5$. The controller is implemented in Simulink, which is then translated to code and flashed on the microcontroller. The simulink model used for this can be found in Appendix H.

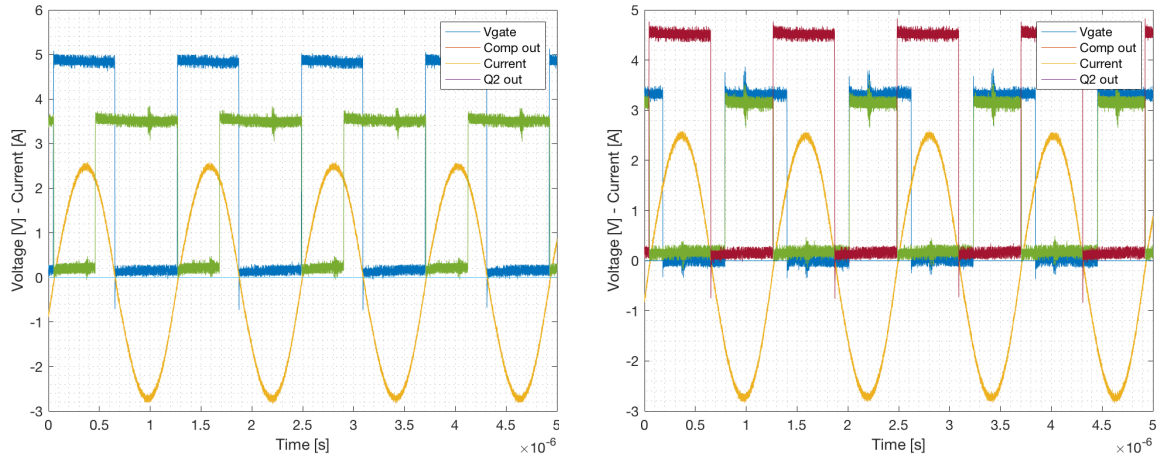

(a) Leading Current

(b) Lagging Current

Figure 7.3.2: Experimental results for leading and lagging currents

Unfortunately, it turned out that the response time was not as fast as it was supposed to be. Since the resonance trackers should be the fastest of the controller, such that the MEPT and power controllers are not affected by it. However this did not turn out to be possible, since jitter and noise caused oscillations in the frequency when the settling time was below a second. Because of this the frequency controller and voltage controllers are not able to operate at the same time and thus should be controlled seperately. Unfortunately, due to lack of time a system which deals was not made. Therefore the controllers were only tested seperately. Regarding, the resonance tracker in the rectifer. Inititially it was believed that the resonance tracker would work in the same way as with the inverter. However, since for the inverter the gate signals trigger the resonant current their phase is always proportional to their frequency difference. For the rectifier the gate signals are not triggering the current and therefore their phase is not stationary (similar to two signals on an oscilloscope, having the same frequency but not being triggered by the same pulse). Since this phase is not stationary it is also not controllable. To solve this a trigger pulse was sent from the inverter microcontroller which was synchronizing the inverter and rectifier microcontroller. This solved the problem, however this was done using a cable and in an actual wireless charging system the delay caused by the wireless communication would cause this to fail. Because of this the rectifier could not operate synchronously in an actual system. However using the diodes of the inverter and rectifier, it still possible to operate the system bidirectionally.

7.4 Conclusion

In this chapter the operation of the MEPT control scheme was shown and with an efficiency improvement of 5 to 23% it is succesfull. Furthermore the phase detection circuit is shown to work properly, unfortunately the frequency controllers could not be tuned such that these were fast enough without causing oscillations in the frequency. In the next and final chapter the entire thesis in concluded and suggestions for future work are given.

CHAPTER 8

CONCLUSION & FUTURE WORK

In this chapter the work done during this master thesis is summarized by discussing the implementation of all the research questions and objectives, which were specified in the introduction. Based on these findings an analysis on the future work is done.

8.1 CONCLUSION

In the future electric vehicles will play a big role in creating a sustainable environment. Inductive charging can play a big role in overcoming the drawbacks of electric vehicles and because of this all of its possibilities should be investigated.
As said in the introduction, this master thesis has two main goals: 1. find, design and implement the best control scheme for a misalignment tolerant inductive charging system 2. Design the system such that bidirectional power flow is possible. In order to achieve these goals multiple research questions and objectives have been set, below is a list of all these questions and objectives including a summary of how these have accomplished.

- What are the dynamics of a series-series resonant tank? By looking at the frequency behaviour of the resonant tank, it was seen that the voltage gain and input impedance of the resonant tank have a strong frequency dependancy. Furthermore, multiple resonant frequencies can occur depending on the quality factor of the tank.

- How does bifurcation play a role in a series-series resonant tank? Above a certain limit of tank quality factor, it was seen that the resonant tank becomes a fourth order system. Giving rise to multiple zero phase angle frequencies, physically this means two frequencies at which maximum voltage gain is achieved (both at lower gain than at bifurcation free operation). Because this complicates the control and decreases the efficiency, bifurcation should be avoided if possible. The limits at which bifurcation occur were determined, and from this it was clear that if the maximum efficiency point tracking control scheme is followed bifurcation is avoided.

- What is the best control method for controlling the power in a bidirectional misalignment tolerant system? In Chapter 3 multiple power control methods were discussed. It was seen that voltage control gave the highest efficiency, since this method allows the system to be operated at the resonant frequency over the whole operating range allowing for maximum power transfer efficiency and no circulating currents. Furthermore, the switching happens (almost) lossless at every inverter switching instant. Therefore the voltage control method can achieve the highest efficiency, if the losses induced by the extra dc/dc converter are not higher than the above mentioned benefits. However using SiC technology high converter efficiency is obtained.

- How can the system be controlled such that it will always achieve the maximum power transfer efficiency? By performing impedance matching of the secondary resonant tank to the load seen by the secondary side, maximum power point tracking can be performed. This way the maximum transfer efficiency of the inductive link can be achieved. Furthermore, resonance tracking controllers were implemented such that the system is always operating at the resonance frequency.

- How to estimate the alignment of the transformer coils, while using the charger? Based on the voltage equations of the resonant tank the coupling between the transformer coils can be calculated using the primary and secondary voltages and currents. These quantities are estimated by measuring the dc link voltages and transforming them to their AC Fourier equivalents. This way higher accuracy can be accomplished since only DC values have to be measured.

- What method of modelling can accurately and efficiently describe the dynamic behaviour of a series series resonant converter? When modeling the dynamic behaviour of a (resonant) system, a balance between accuracy and complexity has to be found. After some literature review, the extended describing functions method proved to be best in this. Here the system is linearized by using describing functions to approximate all non linear (sinusoid) functions inside the sytem.

- What is the frequency response of the entire system and what is the stable region for the closed loop controllers? The above descriped model is combined with two models of the dc/dc converters based on the state space averaging approach. This final model gave the frequency response of the entire system. Based on this response the gains of the voltage controllers have been determined.

- What is the efficiency of the overall system? At an output power of 180W the overall efficiency was 78% during optimal alignment. The highest efficiency which was achieved was around 80%. It should be noted that for most parts of the system these are partial load efficiencies, since the inverter, resonant tank and the evaluation boards of CREE are made for in the kW range.

From the above summary it is clear that all the research questions and objectives have been accomplished. Furthermore this bidirectional misalignment tolerant control scheme has been designed and implemented on a prototype setup with a total system efficiency of .. %.
Since this was a proof of concept design, further improvements can be made in the future. This is discussed in the next section.

8.2 Future Work & Discussion

Now that the concept of this control scheme has been proven to work, the setup can be made for higher power levels. Furthermore, a method has to be found to wirelessly communicate the power setpoint and voltage levels. Also, the rectifier pulse is something which will not work with a delay in the ms range (due to wireless communication). Therefore the following things are proposed:

- The dc/dc converters have to be designed for higher power levels, this includes a new study on possible topologies and control schemes for the converters. For example a multilevel half bridge topology operating in boundary conduction mode can be used, such as the one proposed in [1]. This way high power levels and densities can be achieved at high efficiencies.

- The resonance tracking method can be made more stable using a self oscillating system, where the zero crossing of the current can be used as a trigger for the switching of the inverter and rectifier both. This way no PI-controllers are needed which are affected by jitter and no trade off has to be made between overshoot and response time. This would also cancel the need for a trigger pulse (and the necessary wireless communication) for the synchronous rectifier. However, this would include the design of a start up circuit such that no manual triggering is needed for the system to start up.

- In order for the system to be totally contactless, wireless communication has to be installed to communicate the power setpoint and (if still necessary) the trigger pulse for the rectifier.

- Using recursive least squares filters or observer based filters, the noise in the coupling estimation can be improved. Since this coupling factor determines the duty cycle of the dc/dc converters, reducing the noise can ensure a more stable operation.

Bibliography

[1]: Y. Yang, Y. Benomar, M. El Baghdadi, O Hegazy, J. van Mierlo, *"Design, modeling and control of a bidirectional wireless power transfer system for light duty vehicles"*, Vrije Universiteit Brussel (VUB), ETEC Dept. & MOBI Research Group.

[2]: M. Fisher, Taylor, Blair Farley, Kathleen, Gao, Yabiao, Bai, Hua, Tse, Zion. (2014). *"Electric vehicle wireless charging technology: a state-of-the-art review of magnetic coupling systems"*. Wireless Power Transfer. 1. 87-96. 10.1017/wpt.2014.8.,

[3]: K. Aditya, S.S. Williamson *"a review of optimal conditions for achieving maximal power transfer"*, IEEE transactions on transportation electrification Vol 3. No. 2 June 2017.

[4]: W. Zhang, S. C. Wong, C. K. Tse, Q. Chen, *"Analysis and Comparison of Secondary Series- and Parallel-Compensated Inductive Power Transfer Systems Operating for Optimal Efficiency and Load-Independent Voltage-Transfer Ratio"*, IEEE transactions on power electronics Vol. 29, No 6. June 2014.

[5]: R. Bosshard, J.W. Kolar, J. Muhlethaler, I. Stevanovic, B. Wunsch, F. Canales, *"Modeling and n-a-Pareto Optimization of Inductive Power Transfer Coils for Electric Vehicles"*, IEEE journal of emerging and selected topics in power electronics Vol 3. No. 1. March 2015.

[6]: C.S. Wang, G.A. Covic, O.H. Stielau *"Power Transfer Capability and Bifurcation Phenomena of Loosely Coupled Inductive Power Transfer Systems"*, IEEE transactions on industrial electronics Vol. 51. No. 1 February 2004.

[7]: S.H. Hosseini, A. Y. Goharrizi. *"Harmonic Optimization of Asymmetrical Voltage-Cancellation Control for Full-Bridge Series Resonant Inverters"*, SICE-ICASE International Joint Conference 2006

[8]: M. Kosik, R. Fajtl, J. Lettl, *"Analysis of bifurcation in Two-Coil Inductive Power Transfer"*, IEEE 978-1-5090-5326-1/17$31.00 2017

[9]: R. C. Fernandes ; A. A. de Oliveira *"Theoretical bifurcation limits for wireless power transfer"*, 2015 IEEE 13th Brazilian Power Electronics Conference and 1st Southern Power Electronics Conference (COBEP/SPEC)

[10]: R. Bosshard, U. Badstubner, J.W. Kolar, I. Stevanovic *"Comparative Evaluation of Control Methods for Inductive Power Transfer"*, Power Electronic Laboratory, ETH Zurich, Switzerland.

[11]: A. Kunwar, *"Design and Implementation of an Inductive Power Transfer System for Wireless Charging of Future Electric Wireless Transportation"*, University of Ontario Institute of Technology, Oshawa, Ontario Canada, August 2016.

[12]: J.M. Burdio, L.A. Barragan, F.M. Monterde, D. Navarro, J. Acero, *"Asymmetrical Voltage-Cancellation Control for Full-Bridge Series Resonant Inverters"*, IEEE transactions on Power Electronics Vol. 19, No. 2, March 2018.

[13]: F. S. Tsai, P. Materu, F.C.Y. Lee *"Constant Frequency Clammed Mode Resonant Converters"*, IEEE transactios of Power Electronics, November 1988.

[14]: S. Bai, Z. Pantic, S. Lukic, *"A Comparison Study of Control Strategies for ZVS Resonant Converters"*, IEEE 978-1-4244-5226-2/10/$26.00 2010

[15]: R. Bosshard, U. Badstubner, J.W. Kolar, *"Control Method for Inductive Power Transfer with high partial load efficiency"*, The 2014 International Power Electronics Conference.

[16]: S. Bandyopadhyay FEM model 2018. TU delft.

[17]: K. Hata, T. Imura, Y. Hori, *"Efficiency Maximization of Wireless Power Transfer Based on Simultaneous Estimation of Primary Voltage and Mutual Inductance Using Secondary-Side Information"*, 978-1-5090-3474-1/16/$31.00 2016 IEEE

[18]: R. Bosshard, U. Badstubner, J.W. Kolar, *"Control Method for Inductive Power Transfer with high partial load efficiency"*, The 2014 International Power Electronics Conference.

[19]: M. Mohammad, S. Choi, *"Sensorless Estimation of Coupling Coefficient Based on Current and Voltage Harmonics Analysis for Wireless Charging System"*, 978-1-5090-2998-3/17/$31.00 2017 IEEE.

[20]: V. Jiwariyavej, T. Imura, Y. Hori, *"Coupling Coefficients Estimation of Wireless Power Transfer System via Magnetic Resonance Coupling Using Information From Either Side of the System"*, IEEE Journal of Emerging and Selected Topics in Power Electronics, Vol 3. No. 1. March 2015.

[21]: D. Kobayashi, T. Imura, Y. Hori, *"Real-time Coupling Coefficient Estimation and Maximum Efficiency Control on Dynamic Wireless Power Transfer for Electric Vehicles*
[22]: Maximum Efficiency Tracking for Wireless Power Transfer Systems with Dynamic Coupling Coefficient Estimation", 978-1-4799-6610-3/15/$31.00 2015 IEEE

[23]: Y. Jiang, Y. Wang, J. Liu, X. Li, L. Wang, *"An Accurate Phase Detection Method for Realizing ZVS of High Frequency Inverter in Wireless Power Transmission"*, 978-5090-5157-1/17/$31.00 2017, IEEE.

[24]: A. P. Hu, *"Modeling a Contactless Power Supply Using GSSA Method"*, Department of Electrical and Computer Engineering, the University of Auckland, Auckland, New Zealand.

[25]: A. Safaee, K. Woronowicz, *"Time-Domain Analysis of Voltage-Driven Series–Series Compensated Inductive Power Transfer Topology"*, IEEE Transactions on Power Electronics, Vol. 32, No. 7, July 2017.

[26]: E. X. Q. Yang, F.C.Lee, B. H. Cho, D. Borojevic, Y. Liu, *"Extended Describing Function Method for Small-Signal Modeling of Resonant and Multi-Resonant Converters"*, Blacksburg Virginia, February 1994

[27]: Z.U. Zahid, Z. M. Dalala, J. S. Lai, *"Modeling and Control of Series–Series Compensated Inductive Power Transfer System"*, IEEE Journal of Emerging and Selected Topics in Power Electronics, Vol 3, No. 1, March 2015.

[28]: K. Aditya, S.S. Williamson, *"Simplified Mathematical Modelling of Phase-Shift Controlled Series-Series Compensated Inductive Power Transfer System"*, 978-1-5090-0873-5/16/$31.00 2016 IEEE

[29]: *"Loop Stability Analysis of Voltage Mode Buck Regulator With Different Output Capacitor Types"*, http://www.ti.com/lit/an/slva301/slva301.pdf, Accessed: 2018-06-20

[30]: Y. Bavafa-Toosi, *"A Note On the Gain and Phase Margin Concept"*, Journal of Control and Systems Engineering, December 2015.

[31]: F. Caricchi, F. Crescimbini, F. Giulii Capponi, L. Solero *"Study of Bi-Directional Buck-Boost Converter Topologies for Application in Electrical Vehicle Motor Drives"*, 0-7803-4340-9/98/$10.00 1998 IEEE.

[32]: A. Mirzaei, A. Jusoh, Z. Salam, E. Adib,H. Farzanehfard, *"A novel soft switching bidirectional coupled inductor Buck-Boost converter for battery discharging-charging"*, 2011 IEEE Applied Power Electronics Colloquium (IAPEC)

[33]: V. V. S.K. Bhajana ; P. Drabek, *"A new soft switching bidirectional buck or boost DC-DC converter"*, 2015 IEEE International Conference on Industrial Technology (ICIT)

[34]: Y.Jang ; M. M. Jovanović, *"Soft-Switched Bidirectional Buck-Boost Converters"*, 2017 IEEE Applied Power Electronics Conference and Exposition (APEC)

[35]: N. Mohan, T.M. Undeland, W. P. Robbins, *"Power Electronics Converters, Applications and Design"*, 2nd Edition, John Wiley & Sons, Inc.

[36]: Ferroxcube, *"Power loss coefficient spreadsheet"*.

[37]: K. Aditya, S.S. Williamson, *"Simplified Mathematical Modelling of Phase-Shift Controlled Series-Series Compensated Inductive Power Transfer System"*, 978-1-5090-0873-5/16/$31.00 2016 IEEE

[38]: KIT8020CRD8FF1217P-1 CREE Silicon Carbide MOSFET Evaluation Kit, https://media.digikey.com/pdf/Data%20Sheets/CREE%20Power/KIT8020CRD8FF1217P-1_UM.pdf, visited May-August 2018, CREE company

[39]: C2M0280120D, https://www.wolfspeed.com/media/downloads/171/C2M0280120D.pdf

[40]: C4D20120D Datasheet, https://www.wolfspeed.com/media/downloads/106/C4D20120D.pdf

CHAPTER 9

APPENDICES

9.1 APPENDIX A: IPT SIMULATION IN SIMULINK

Figure 9.1.1 shows the simulink model used to analyse the different control methods. Table 9.1.1 shows the simulations parameters.

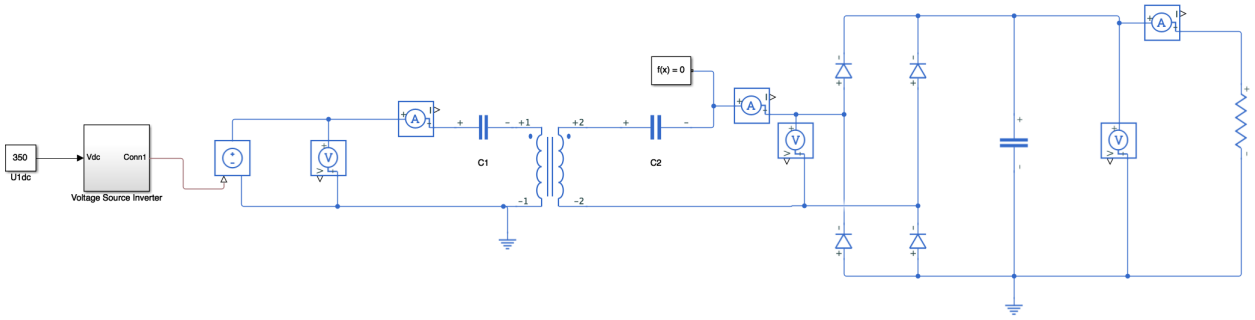

Figure 9.1.1: Simulink Model of inductive power transfer system

Table 9.1.1: Simulation Parameters

Symbol	Quantity	Value
V_{in}	Input Voltage	350V
L_P	Primary Inductance	200 μH
L_S	Secondary Inductance	200 μH
C_P	Primary Capacitance	18.9 nF
C_S	Secondary Capacitance	18.9 nF
C_{out}	Output capacitance	300 μF
R_{out}	Output resistance	20 Ω
$S_{1,4}$	Switch	

9.2 Appendix B: IPT simulation in Simulink: Voltage Control

Figure 9.2.1 shows the simulink model used to analyse the voltage control methods. Futhermore, Figures 9.2.2 and 9.2.3. shows the simulink models used to verify the controllers.

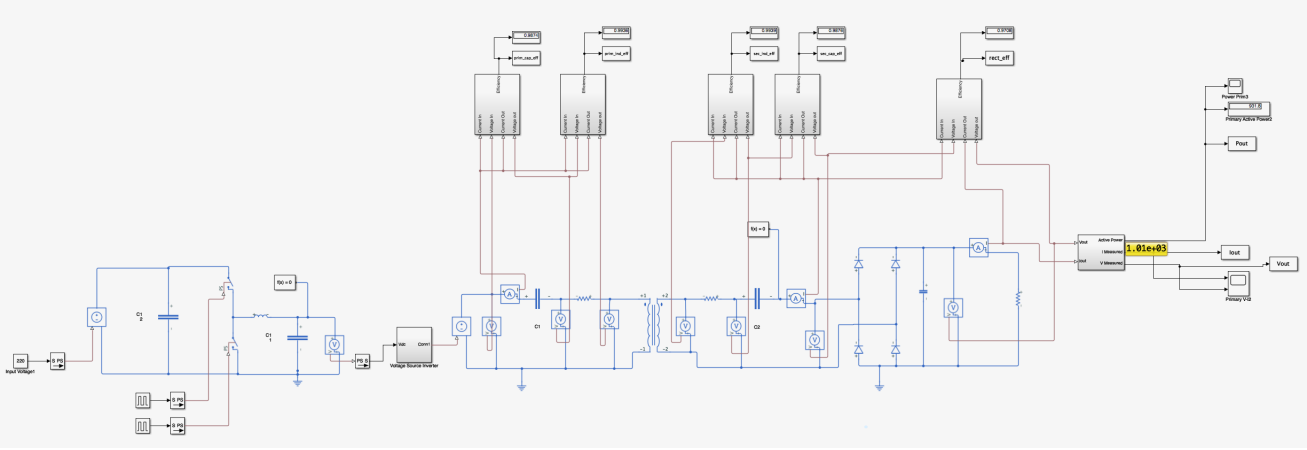

Figure 9.2.1: Simulink Model of for voltage control

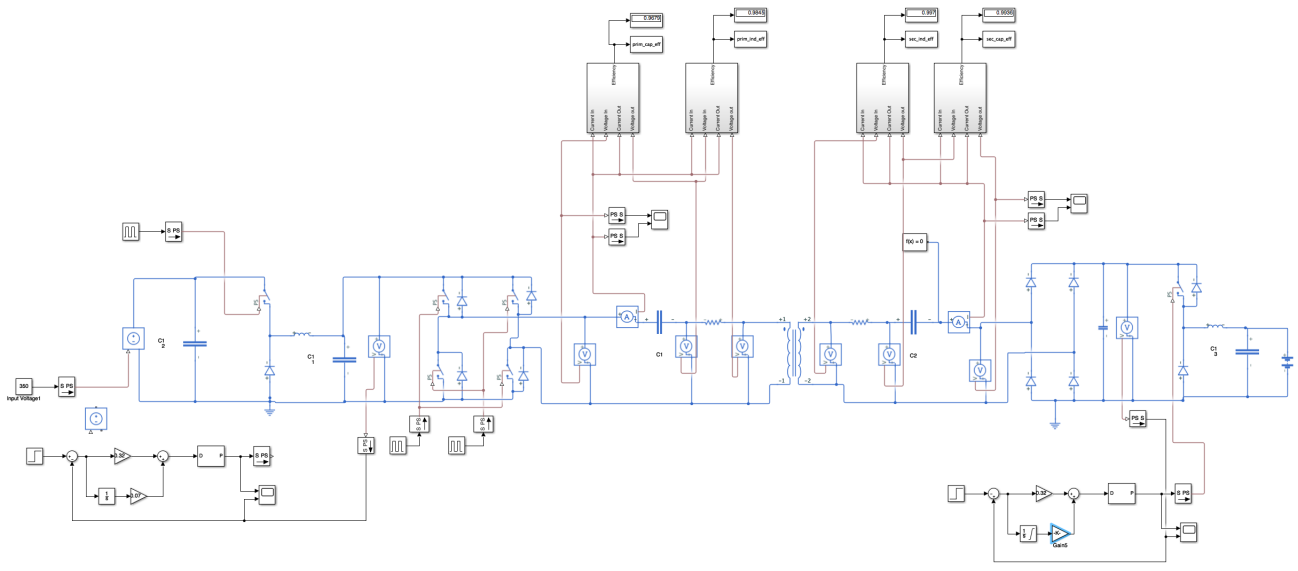

Figure 9.2.2: Buck controllers implemented in simulink

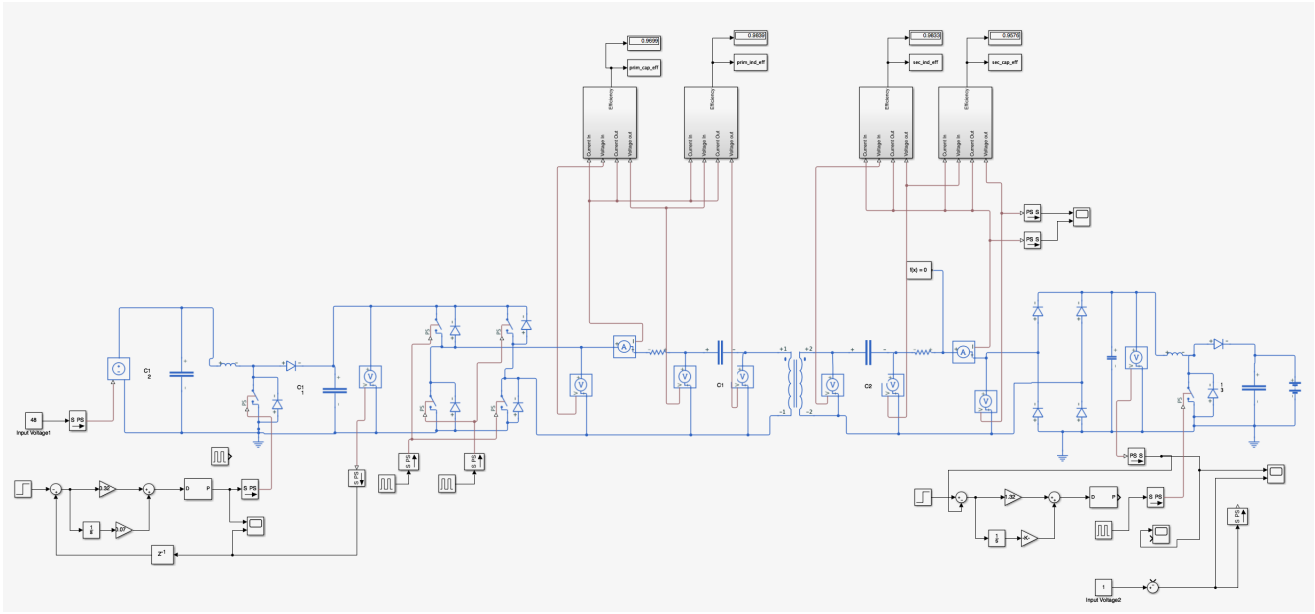

Figure 9.2.3: Boost controllers implemented in simulink

9.3 Appendix C: Dc/dc converter design

First the specifications of the converters should be specified, these can be found in table 9.3.1. Then the topology of the converter should be determined. Research into bidirectional buck-boost converters show a great variety in topologies, for example the cascaded buck-boost converter [31], the resonant cascaded buck-boost converter [32], the dual auxiliary switch converter [33] or the active snubber converter [34]. However all of these converters either use 3 or more switches and multiple inductors and apart from the cascaded buck-boost converter all of them have complex control schemes.
Furthermore, depending on the direction of power only a buck or boost operation is needed. Therefor a halfbridge topology is chosen (with a buck operation for grid to vehicle (G2V) power transfer and boost for vehicle to grid (V2G) power transfer), since it only utilizes two switches and a single inductor, it is by far the most effective topology.

Table 9.3.1: Dc/Dc converter specifications

Parameter	Value
V_{grid}	350V
$U_{1,dc}$	30-120V
$U_{2,dc}$	30-120V
U_{bat}	48V
$P_{out,max}$	500 W
$f_{s,dc/dc}$	50 kHz
$\frac{\Delta i_L}{i_{out}}$	10 % @ 500W
$\frac{\Delta V_o ut}{V_{out}}$	5 % @ 500W

The switching frequency is chosen to be 50kHz, since higher frequencies only increase the losses and power density is less important for this proof of concept design. Furthermore, the inductor current ripple is specified to 10% with respect to the output current at full load such that the converters operate in continuous conduction mode (CCM) over the entire power range. CCM has been chosen as operating mode because the peak current at BCM or DCM at high powers results in higher losses. The output voltage ripple is also specified to 10% with respect to the output voltage, such that the DC links can be assumed to be DC and are not affected much by switching.

STEADY STATE MODELING

Once the specifications are known the calculation of the in- and output capacitance and inductance value can be calculated. This is done using equations (9.3.1) and (9.3.2). In the comming analysis the design procedure will be discussed for the buck converter case, however the entire procedure is analoguos for the boost converter case.

$$V_L = L\frac{di_L}{dt} \Rightarrow L = \frac{V_L dt}{di_L} \tag{9.3.1}$$

$$i_C = C\frac{dV_c}{dt} \Rightarrow C = \frac{i_C dt}{dV_c} \tag{9.3.2}$$

Now consider the buck converter 1 operating at 500W, 350V in and 120V out, the inductor current would then look like the waveform shown in Figure 9.3.1. As specified the current ripple should be 10% of the output current, which at 500 W equals 4.2 A and the ripple current is thus 0.42A (for now the converter is assumed to be losless).

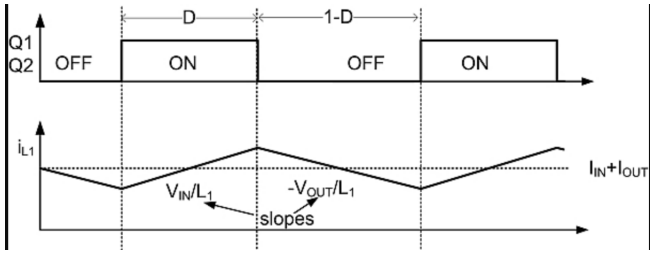

Figure 9.3.1: Buck Converter Switching cycle [35]

Then in the time period where the top switch is on:DT_s:

$$di_L = 0.42A \tag{9.3.3}$$

$$dt = DT_s = \frac{120}{350 * 50 * 10^3} = 6.58\mu s \tag{9.3.4}$$

$$V_L = V_{in} - V_{out} = 230V \tag{9.3.5}$$

Substituting this in equation (9.3.1), gives an inductor value $L_1 = 3.8mH$.
The calculation of the output capacitor can be based on the output transient response or on the output voltage ripple. Since for this case the output voltage settling time does not have to be extremely fast, it is based on the output voltage ripple. In that case the minimum value of the capacitor is based on the amount of charge which should be stored inside the capacitor, this is depicted as the dark surface shown in figure 9.3.2. and can be calculated according to equation 9.3.3. For the 500W buck converter case this results in 87.5nF.

$$C_{out,buck} = \frac{\Delta I_L T_s}{8\Delta V_{out}} \tag{9.3.6}$$

For the buck converter input capacitor, eq. (8.3.7) is used [36].

$$C_{in,buck} = \frac{I_{out} D(1-D)}{V_{ripple} * f_s} \tag{9.3.7}$$

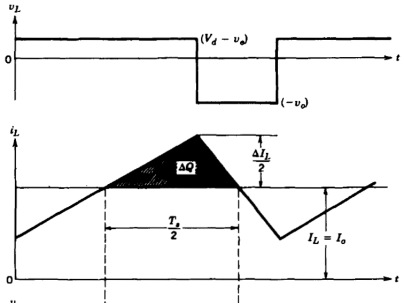

Figure 9.3.2: Capacitor stored charge [35]

Applying these methods for both dc/dc converters in both buck and boost mode, results in the circuit parameters given in table 9.3.2. The value chosen for the inductor is middle ground between the buck and boost case. Since for a too large inductor value, the right half plane zero of the inductor is too dominant. However for a smaller inductor the ripple is to big for the buck converter. Furthermore, because the system is designed to be bidirectional, it is desired to keep the system symmetrical around the transformer. Therefor the input capacitance of dc/dc1 equals the output capacitor of dc/dc2 and vice versa. Note that on the final setup much larger capacitances were used, for stability and since the expected ripple was larger.

Table 9.3.2: Dc/Dc converter specifications

Parameter	$C_{1,dc}$	$C_{2,dc}$
Buck mode	500nF	2.72 μF
Boost mode	2.88 μF	500 nF
chosen	300 μF	300 μF

In order to save time designing and testing the dc/dc converters, half bridge evaluation boards designed by CREE are used. The boards consist of two 1200V 10A SiC MOSFETs with two SiC diodes parallel to them, driven by a half bridge gate drive circuit and heatsink. More information about the modules can be found in Appendix E.
In order to finish the dc/dc converters an inductor, in- and output capacitors, measurements circuits and a microcontroller have to be added to the evaluation board. All of these, except the inductor, are put on the same PCB as the resonance tracker which will than be mounted on the evaluation boards. Based on the operating voltage and frequency, polypropylene film capacitors are chosen for the dielectric material of the output capacitors. This is based on the graph shown in Appendix F. Furthermore Appendix C shows the schematic of the in- and output voltage and current measurement circuits, as well as the PCB layout for both the resonance tracker and measurement circuits. Finally the inductor has to be designed, since it can not be chosen from off the shelf inductors. This design proces is discussed in the next section.

INDUCTOR DESIGN

When designing the inductor it was tried to minimize the losses, while still ensuring saturation free operation at the highest power level. The losses of the inductor are comprised of

- Core losses: The losses in the core consist of hysteresis losses, which are the losses which occur when it is traversing its BH-curve (also called hysteresis loop) and are caused by the effort to align the magnetic dipoles to the magnetic field. Other core losses are eddy current losses, caused by the current induced in the material, due to the flux passing through a conductive layer. Both of the above losses are dependant on the magnitude of the flux density, since for higher flux densities the area under the BH-curve gets bigger and more current is induced in the material. Furthermore, both of the losses are dependant on the frequency with which the core is excited, since at higher frequencies the dipoles have to change their alignment more often, while a higher rate of change of flux induces a higher voltage and current inside the material causing more eddy current losses as well.
  Finally there are some residual losses, often negligible, which is a collective name for multiple non-idealities such as non-isotropicality or internal resonances inside the material. However these are

very hard to calculate and often negligible compared to the hysteresis and eddy current losses and there for neglected in this thesis.
The formula used for calculating the core losses is given in equation (5.1.7) [36].

$$P_{iron} = \iiint (C_{hys} f^x ||B||^y) dV (C_2 T^2 - C_1 T + C) + \frac{1}{V} \iiint (C_{eddy} f^2 ||B||^2) dV \tag{9.3.8}$$

Here C_{hys}, C_{eddy},x,y are material specific coefficients, also C_1 and C_2 are temperature coefficients of the material. All of them should be specified by the manufacturer of the material. For multiple materials these values (apart from C_{eddy} are found in Appendix I. Since C_{eddy} is not specified in the material leaflet given in Appendix I, and because of the relative low operating frequency and low conductivity of the ferrite material, the eddy current losses can be neglected when calculating the core losses. Equation (9.3.7) can then be simplified to equation (9.3.8). Here V_e is the effective volume of the core.

$$P_{hys} = C_{hys} f^x ||B||^y (C_2 T^2 - C_1 T + C) V_e \tag{9.3.9}$$

- Winding losses: the other part of the inductor losses occur in the windings in the form of ohmic losses. Primarly these losses are determined by the conductivity of the material and the amount of current running through the wires, Ohm's law. However since the current through the windings is AC, skin and proximity effects also have to be taken into account. Skin effect is the effect where eddy currents prevent the inner parts of a wire to carry any current, as discussed above this effect increases with frequency. The skin depth of a material can be calculated according to:

$$\delta = \frac{1}{\sqrt{\mu_r \mu_0 \sigma \pi f}} \tag{9.3.10}$$

Here μ_r, μ_0 are the relative and initial permeability of the material, σ is the conductivity of the material and f is the frequency. Besides skin effect, also the proximity effect affects the spatial orientation of current in a wire. The proximity effect is caused by eddy currents induced in a wire adjacent to another current carrying wire. The current induced in this first mentioned wire will reinforce the main current of this wire at the adjacent side, while it opposes the main current at the opposing side. This causes the current distribution to shift towards to adjacent side of the wire, this effect increases dramatically when multilayer windings are used.
Combining both skin- and proximity effect, determining the effective AC resistance of a wire is hard, therefor graphs such as the one shown in Appendix J are used.

Now that the inductor losses are clear, the design process of the inductor can begin. As said in the begin of this section it is desired to minimize the losses, then using equation (9.3.8) and the material specifications in Appendix G, it can be seen that the best material at this frequency is 3C90. Next the type and size of the core and wires need to be determined, here only ETD cores and the wire sizes available at the university are taken into account to limit the amount of choice (see Appendix K.)
Next, from the electrical circuit it is known that for dc/dc 1 an inductor value of 2 mH is desired. Then using eq. (9.3.11) the minimum amount of turns needed to avoid saturation can be chosen.

$$N = \frac{L\hat{I}}{B_{max} A_e} \tag{9.3.11}$$

Here L is the inductance value, $\hat{I}$ is the peak current through the inductor, B_{max} is the maximum allowable flux density and A_e is the effective cross section of the core. Then chosing the maximum allowable fluxdensity at 0.4T. Then from the formula for the core loss it is seen that the core loss has an exponential increase in loss with respect to the flux density and a linear increase with respect to the volume of the core. Since it is desired to minimize the core losses and the amount of turns, the core with the largest cross section is chosen (ETD59/31/22). Then using the fact that the peak current through inductor 1 is equal to 6A, the minimum amount of turns to avoid saturation is $N = 81$ turns.
At this point the inductance value of the core is to high, due to the large permeability of the ferromagnetic material. Therefore an airgap is introduced. The lenght of this airgap is determined using the fact that the airgap reluctance will dominate the total reluctance of the core and will be equal to:

$$R_{gap} = \frac{l_{gap}}{\mu_0 A_e} \tag{9.3.12}$$

Here l_{gap} is the length of the air gap and μ_0 is the permeability of free space. Then using magnetic circuit theory and using the fact that the airgap will dominate the total reluctande the following equation can be made:

$$NI = \frac{3}{2} B A_e R_{gap} \tag{9.3.13}$$

Here NI is the magnetomotive force and is equal to the amount of turns multiplied with the current. The factor $\frac{3}{2}$ is introduced because an ETD core, with 3 airgaps, is used and therefore the total equivalent gap reluctance is $\frac{3}{2}$ times the reluctance of a single gap. Combining eq. (9.3.12) with eq. (9.3.11) and solving for l_gap results in:

$$l_{gap} = \frac{\mu_0 N \hat{I}}{B_max} = 1.53mm. \tag{9.3.14}$$

Due to fringing effects the total reluctance of the core will be lower. To counteract for this a 2 mm airgap is used. Using the same approach for the second inductor gives $N_2 = 75$ and $l_{gap,2} = 2.55$ mm.

9.4 Appendix D: Reduced Extended Describing Functions Model

In the figure below is the bode plot using the reduced extended describing functions (REDF) concept described in [37]. As can be seen the model is not accurate and therefor not used.

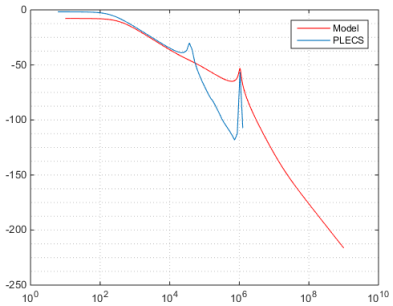

Figure 9.4.1: Bode plot of the REDF model compared with PLECS simulation

9.5 Appendix E: PLECS model

The figure below shows the plecs model which was used for verifying the small signal response of the extended describing function method.

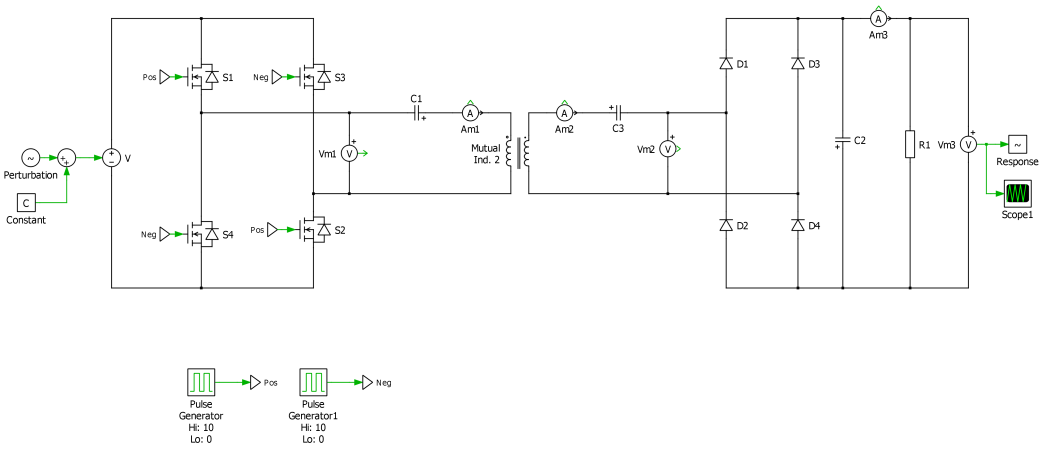

Figure 9.5.1: PLECS model

9.6 Appendix F: Dc/Dc Control Board + Resonance tracker Schematic and PCB layout

Figures 9.6.1-3 show the three different parts of the schematic. All of which are on the same PCB.. Figures 9.6.4 shows the entire routing of the PCB, while Figure 9.6.5-7 show the four layers seperately. Here the third layer (Route 15 in Eagle) is used as the GND plane.

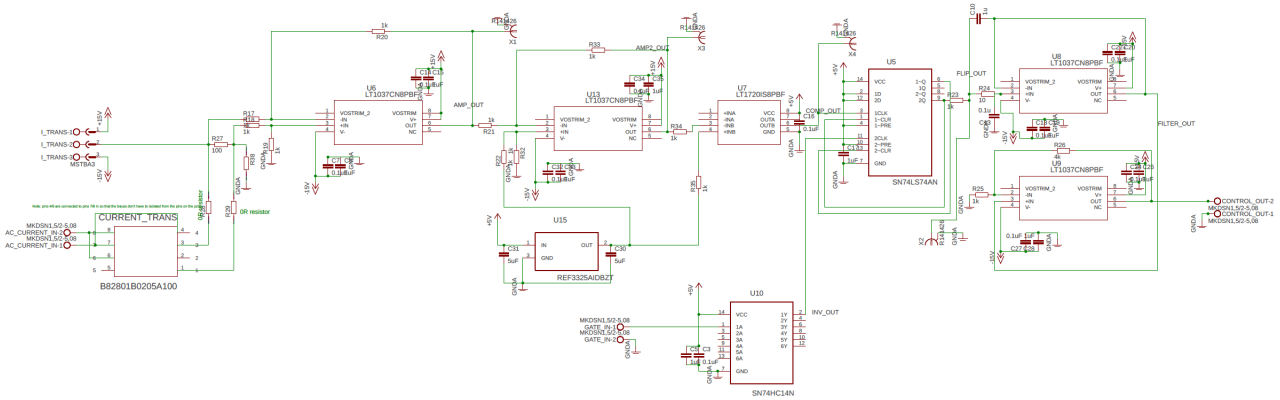

Figure 9.6.1: Resonance tracker schematic

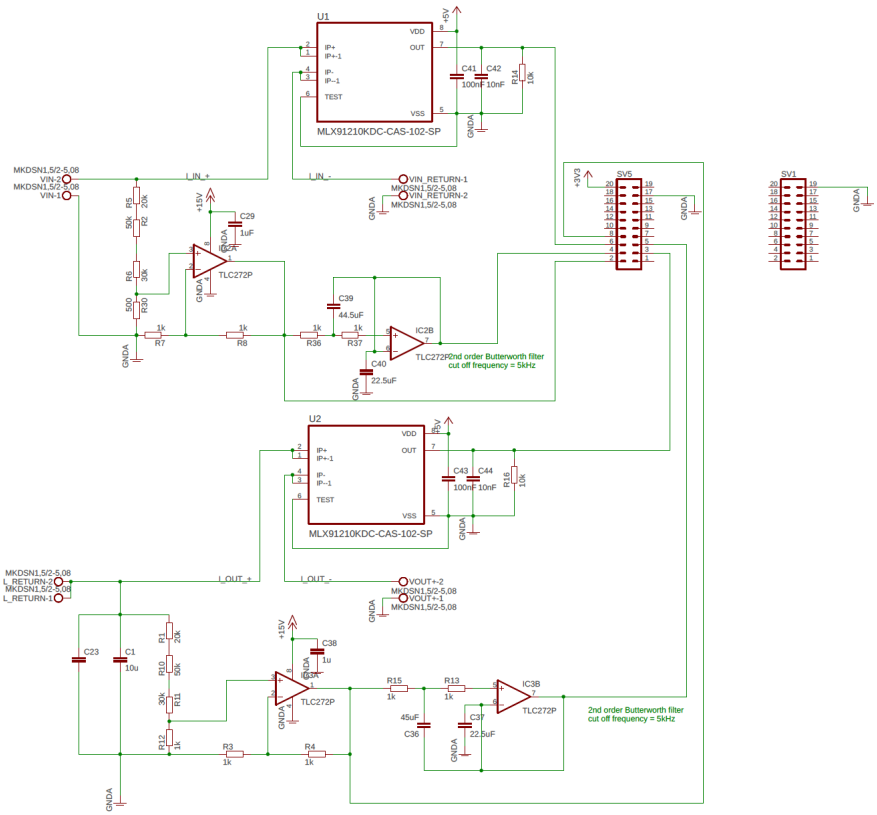

Figure 9.6.2: Dc/dc Control board Schematic

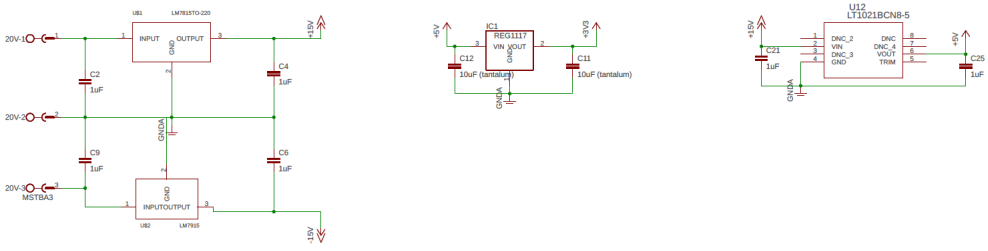

Figure 9.6.3: Auxilliary supply schematic

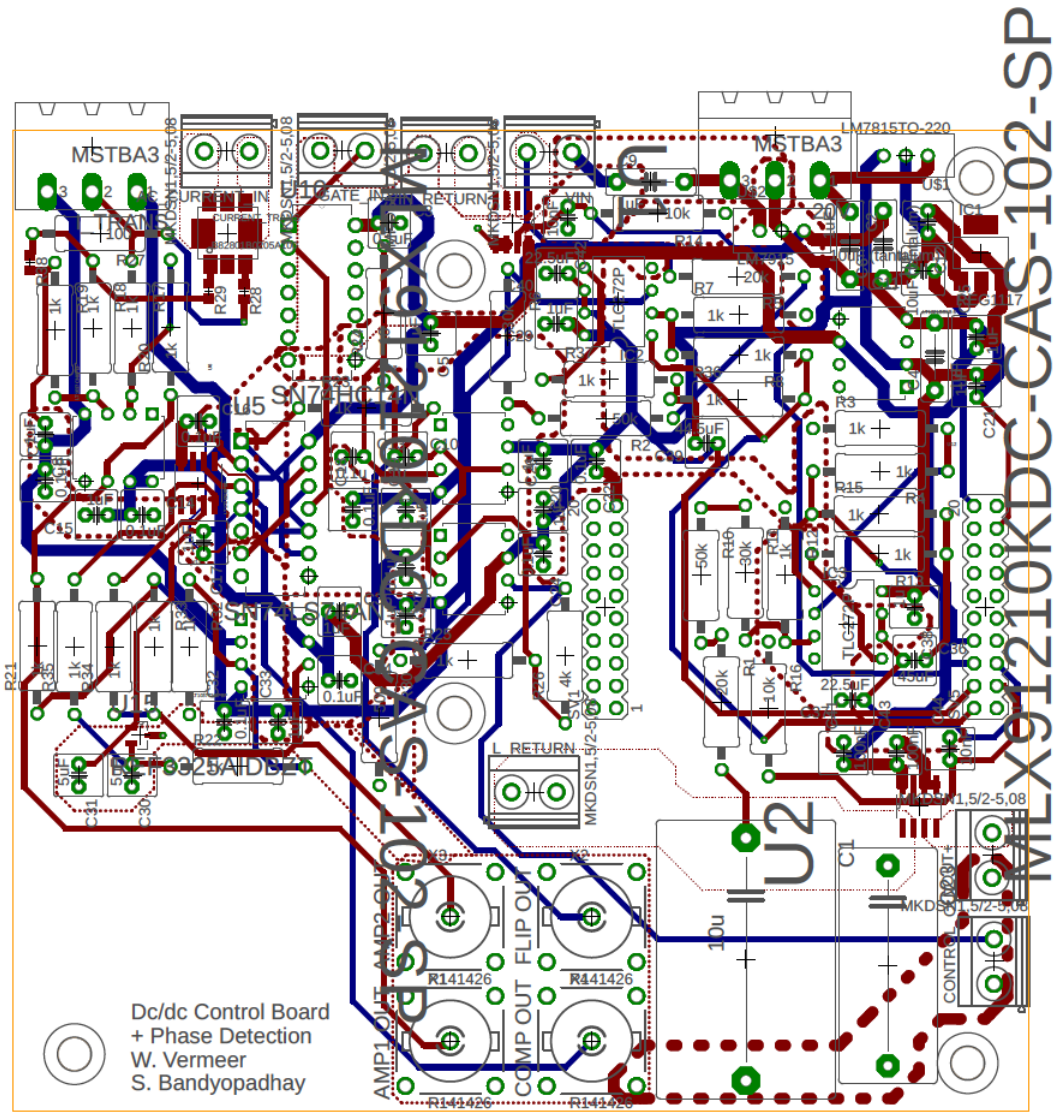

Figure 9.6.4: Complete PCB routing

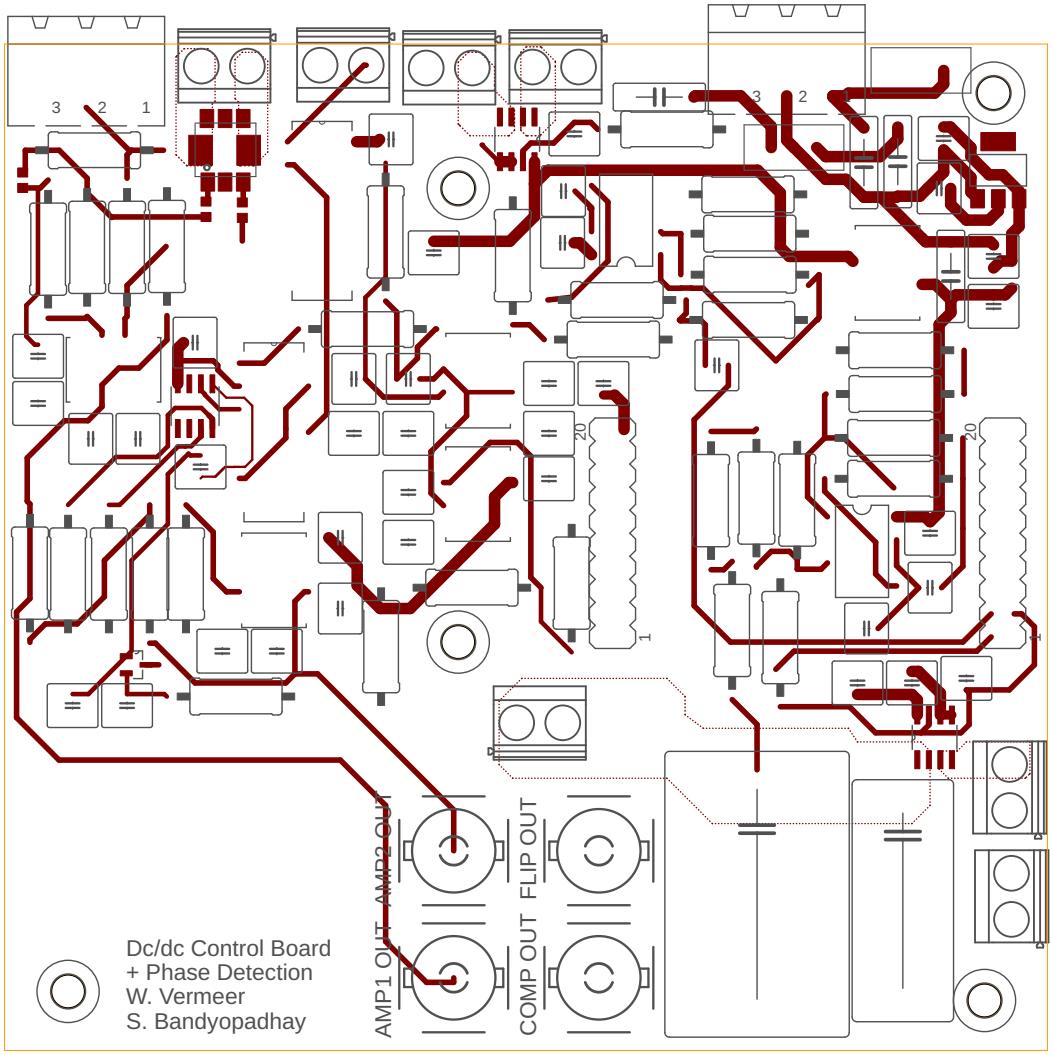

Figure 9.6.5: Top layer

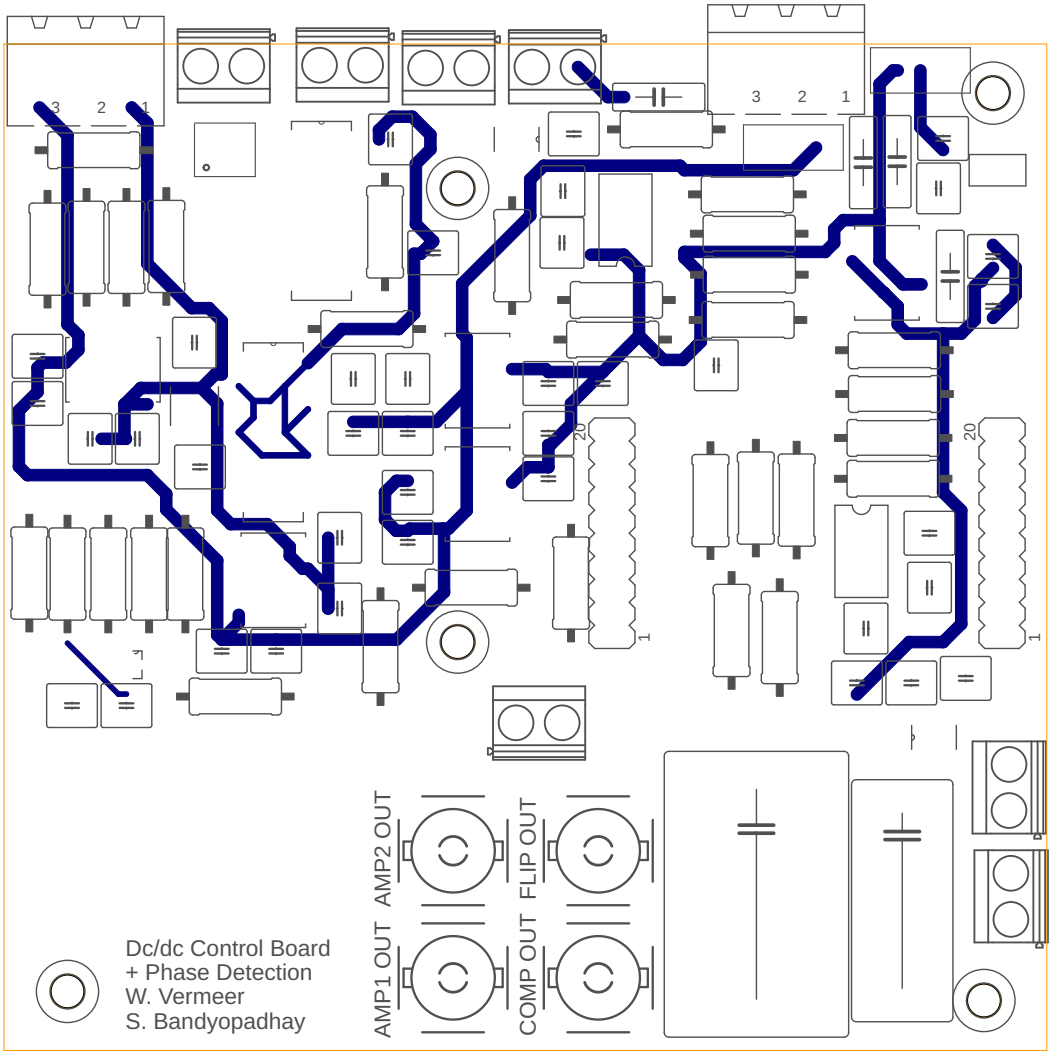

Figure 9.6.6: 2nd layer (Route 2 in Eagle)

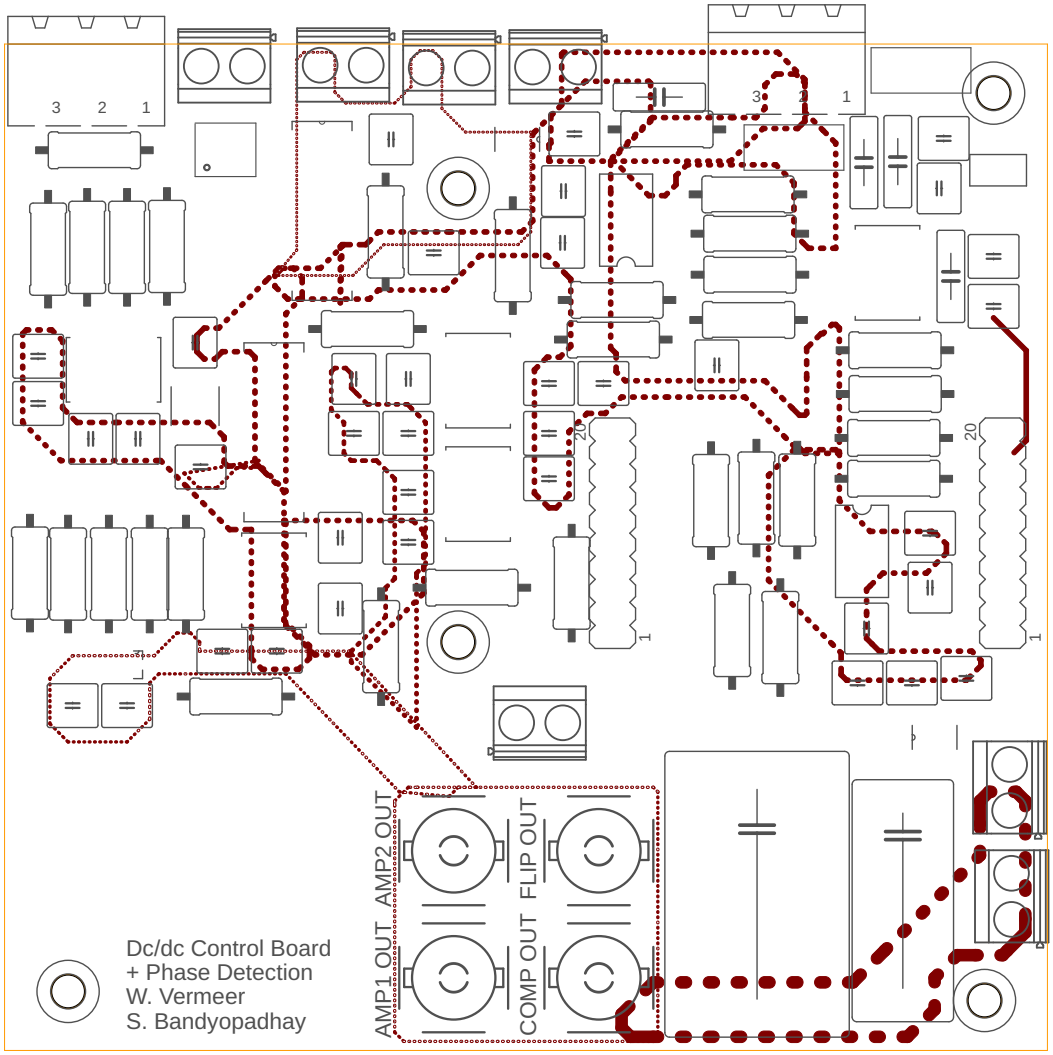

Figure 9.6.7: 3rd layer (Route 15 in Eagle)

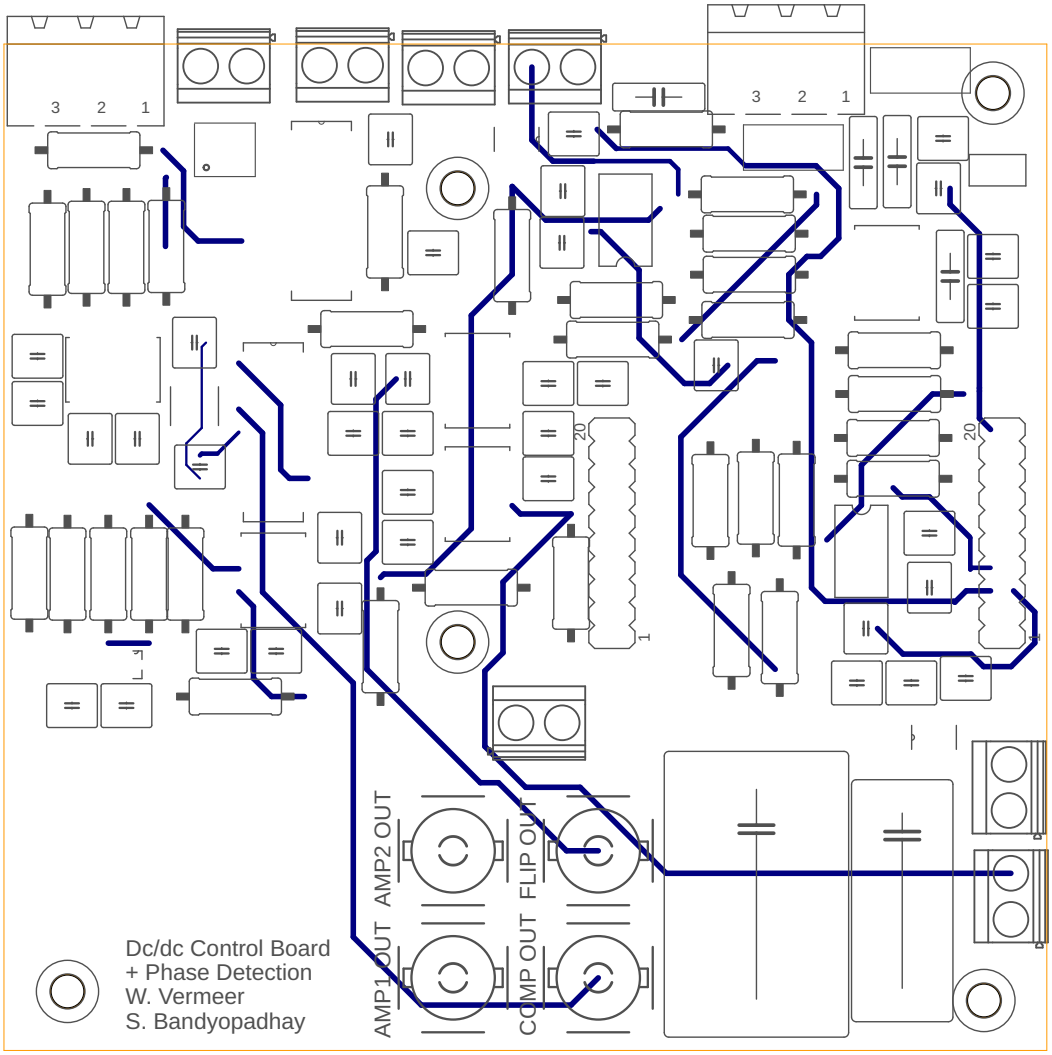

Figure 9.6.8: 4rd/bottom layer

9.7 Appendix G: Loss Calculation

In this chapter a detailed calculation of all the losses inside the system is done, based on measurements performed on the setup. By identifying the losses it can be seen which parts of the system can be improved by future work. In order to calculate these losses measurements are performed on the setup with an electronic load in constant voltage mode at $V_{out} = 48V$ producing $177W$ output power and at the input $V_{in} = 350V$ and $P_{in} = 227W$.

9.7.1 DC/DC 1

dc/dc 1 was operated at 50 kHz with $V_{in} = 350V$ $V_{out} = 74V$ at an efficiency of .. %. First the losses in the switch will be calculated, after which the losses in the inductor and capacitors are calculated. In this section only the losses in the power loop are considered, therefor losses due to gate driving and control are neglected.

Switch losses

The losses in the switch are comprised of the switching losses and the conduction losses. For calculating the switching losses, both drain-source voltages and the drain current of the bottom switch are measured (it is only possible to measure the drain current of the bottom switch, for the schematic see Appendix E.). These can be seen in Figure 9.7.1. Here it can be seen that the bottom switch is turned on/off with zero voltage, since the current is commuted to the diode before the switch is turn on/off.

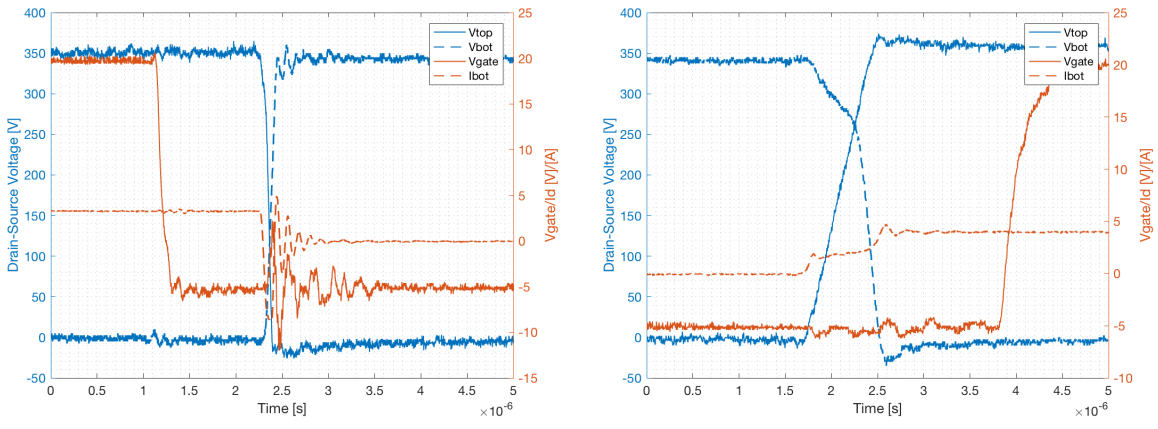

Figure 9.7.1: dc/dc 1 Switching waveforms

The process of commutating the current from top to bottom (or vice versa) can be divided into multiple phases. Figure 9.7.2 shows the division of these phases

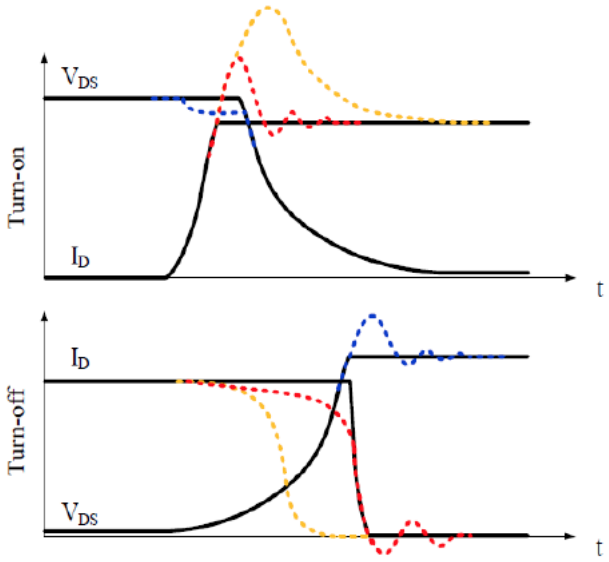

Figure 9.7.2: V_{ds}, I_d during switching transitions

First the turn on process of the top switch will be discussed. This can be divided into three phases:

1. Current rise period
2. Voltage fall period
3. Oscillations

1. Current Rise Period
The losses during the first period are calculated according to eq. (9.7.1) Here the mosfet channel current is assumed to be equal to the drain current, which is assumed to have a linear decline during this phase and is therefor averaged. The second part of eq. (9.7.1) is to account for the losses due to the partial discharge of the switch output capacitor, which occurs due to decrease in V_{ds}, $V_{ds} = 308V$ at the time the current has fallen to zero. Since the drain current of the top switch can not be measured, the current rise time is calculated using eq. (9.7.3)

$$P_{\text{turn on,ph1}} = f_{sw} \int_0^{t_{ir}} v_{ds}(t) i_{d,av} dt + \frac{C_{ds}(V_o) + C_{gd}(V_o)}{2} \left(V_{in}^2 + V_{DS}^2(t_{ir}) f_{sw} \right. \tag{9.7.1}$$

Here,

$$i_d(t) = \frac{I_L(t_{ir})}{2} \qquad \& \qquad v_{ds}(t) = V_{in} \tag{9.7.2}$$

and

$$t_{ir} = R_G C_{iss} \ln\left(\frac{V_{gs}(on) - V_{TH}}{V_{gs}(on) - V_{plateau}}\right) \tag{9.7.3}$$

Here $V_{plateau}$ is the Miller plateau voltage at which the gate-source voltage stays during the voltage fall period, since the MOSFET is still operating in the saturation region and the drain current stays equal to the inductor current. Since this voltage can not be seen from the measurement (due to the SiC technology the gate-drain capacitance is small), it is calculated according to:

$$V_{plateau} = V_{th} + g_{fs}^{-1} I_L = 3.06V. \tag{9.7.4}$$

This results in a current rise time of 0.268ns. Since the Miller plateau is not visible in the scope plot, and since the current fall time of the bottom switch is approximately 35ns this result is considered inaccurate and a rise time of 35ns was used (equal to the fall time of the bottom switch).
Furthermore, the drain soure voltage at the time the current has fallen to zero is equal to 308V. Then using the device capacitances at 350V, and all known data from the plot the losses during this phase come down to $P_{IR} = 0.698W$. 2.Voltage Fall Period

After the current rise phase the entire inductor current is commutated to the bottom diode and the voltage starts to fall. During this phase the switch channel current increases above the inductor current due to discharging of the switch output capacitor into the channel. Note that SiC Schottky diodes are used in parallel to the switch, since these have no reverse recovery this is not included in the losses. Furthermore, by zooming in on Figure 9.7.1. it can be seen that the decay of $V_{ds,top}$ can be approximated to be linear and is thus averaged over the period.

$$P_{\text{turn on,ph2}} = f_{sw} \int_{t_{ir}}^{t_{vf}} \frac{v_{ds}(t_{ir})}{2} \left(I_L + C_{ds} \frac{dV_{ds}}{dt}\right) dt \tag{9.7.5}$$

From the figures, the voltage fall time (90ns), the slope of $\frac{dV_{ds}}{dt}$ (308V in 90ns), and the inductor current (3.68A) can be determined. Filling this in eq. 9.7.5 results in a loss of $P_{VF} = 0.122mW$. This concludes the losses during the turn on of the top switch.
As can be seen from the figure the bottom switch, switches at zero voltage because the diode takes over the inductor current before the bottom switch is turned on. Therefor the only losses in the bottom leg are equal to:

$$P_{diode,bottom} = V_{forw} I_L \frac{t_{on}}{T_s} = 3.3 * 3.2 \frac{1x10^{-6}}{\frac{1}{50x10^3}} = 0.528W. \tag{9.7.6}$$

3. Oscillations
The last part of this transition are the oscillations in the bottom drain current. These oscillations arise from resonance between the switch output capacitance and the parasitic inductances on the PCB. These oscillations are dissipated in different parts of the circuit and are therefor approximated by the amount of power at the start of the oscillations, calculated by:

$$P_{osc} = \frac{1}{2} I_{ds,max}^2 L_{par} \tag{9.7.7}$$

Here $I_{ds,max}$ is the top of the current oscillations, and L_{par} is the parasitic inductance determined by:

$$L_{par} = \frac{1}{\omega^2 C_{ds}} \tag{9.7.8}$$

From the figure the frequency is determined to be $82kHz$ with a starting peak current of -8.62A. This results in a dissipated power of 25.47μW. which is negligible. This concludes all the losses during this switching transition. The total losses during this transition equal 1.226W.
Next, the turning off of the top switch is discussed, again the bottom switch turns on with zero voltage. During this transition two phases can be identified:

1. Voltage rise phase
2. Current fall phase

In this transition no power is dissipated in oscillations, since the drain of the top switch is always connected to the power loop and therefore oscillations can not be sustained.
1. Voltage Rise Period During the first phase the drain source voltage of the switch rises to the DC value, while the current in the channel of the switch decreases from the load current due to the charging of the switch output capacitor. The channel current at the end of this phase is given by:

$$i_{\text{channel}} = I_L - \frac{2C_{oss}\left(I_L + g_{fs} V_{TH}\right)}{g_{fs} R_g C_{gd} + 2C_{oss}} \tag{9.7.9}$$

Note here that both the top and bottom switch output capacitance have to be taken into account since both are discharging current into the channel. Then using the data from the datasheet and the measurements the current at the end of this phase equals -6.49A. This shows that the channel current drops to zero before the voltage has risen to the DC value, because of this the losses in the switch can be neglected. Therefore the only losses during this transition are the losses in the diode, using eq. (9.7.6) these losses are calculated to equal 0.97W. This concludes the losses due to switching. Besides losses due to switching, also conduction losses occur when the switches are conducting. These are calculated according to:

$$P_{\text{cond,top}} = I_{\text{average,switch}}^2 R_{\text{ds,on}} = 3.68A^2 x 80m\Omega = 1.08W. \tag{9.7.10}$$

The total losses in the switches then sum up to 3.3W. Next the losses in the passive components are discussed.

INDUCTOR LOSSES

The losses in the inductor are made up of ohmic losses in the wire and core losses. Using the 3C90 material and the ETD59/31/22 core (see Appendix I for the core dimensions), the core losses are given eq. (9.7.9). :

$$P_{\text{core}} = 3.2 f^{1.46|} |B||^{2.75} (0.000165T^2 - 0.031T + 2.45) \frac{V_e}{1000} W \tag{9.7.11}$$

Here, f is the switching frequency, T is the temperature of the core in $^\circ C$ and V_e is the effective core volume. The peak fluxdensity can be calculated according to:

$$||B|| = \frac{N I_{peak}}{A_{eff} R_{tot}} \tag{9.7.12}$$

where N is the amount of turns on the winding, I_{peak} is the peak current through the winding, A_e is the effective area of the core and R_{tot} is the equivalent reluctance of the core, calculated using the core dimensions and material:

$$R_{tot} = \frac{3}{2} R_{gap} + R_{core} = \frac{l_{eff,core}}{2\mu A_{eff,core}} + \frac{l_{gap}}{\mu A_{gap}} = 1388497[1/H] \tag{9.7.13}$$

That the airgap reluctance is multiplied with a factor of $\frac{3}{2}$ since the total flux passes through the middle leg, then divides in two going through the two outer legs, therefore the total equivalent reluctance is $\frac{3}{2}$ the reluctance of one airgap. Then using the total reluctance of eq. (9.7.12), and the fact that $N = 52$, $I_{peak} = 3.6A$ and $A_{eff} = 368mm^2$. The peak flux density is calculated to be 0.36T. At a temperature of $50^\circ C$ the core losses are then equal to 0.11W.
Next the ohmic losses are calculated according to:

$$P_{\text{wire}} = R_{AC} I_{L,rms}^2 \tag{9.7.14}$$

HereR_{AC} is the AC approximated resistance as discussed in Chapter 5.1 section inductor design. Using eq. (5.1.9) and the fact that the wire used has a diameter of $\phi = 0.6mm$ stacked 1 layer high around the core, the AC resistance is determined to be equal to DC resistance, which is measured to be 0.22Ω. This results in ohmic losses equal to 2.98W. The total losses inside the inductor are then equal to 3.1W.

CAPACITOR LOSSES

The losses inside a capacitor are specified by its equivalent series resistance (ESR) and are made up of the ohmic losses from the electrodes and the dielectric losses and is most of the time specified in the datasheet. The power dissipated inside a capacitor is equal to this ESR times the RMS of the ripple going through that capacitor:

$$P_{\text{cap}} = \frac{\tan(\delta)}{\omega C} I_{rms}^2 = ESR I_{rms}^2 \tag{9.7.15}$$

At the input three 100 μF capacitors are used in parallel, each with an ESR of 170Ω at 50kHz. The current is then divided over these three capacitors (with an input ripple of 1.5A peak), resulting in a total input capacitor loss of 42.5mW.
The same thing holds for the output capacitor, here a 560 μF electrolytic capacitor was used with an ESR of $32m\Omega$. and an output ripple of 1A resulting in 32mW losses.

TOTAL LOSSES DC/DC 1

Table 9.7.1. shows an overview of all the losses in dc/dc1. At an input power of 227W, this results in an efficiency of $\frac{227-6.36}{227} x100\% = 97.2\%$.

Quantity	Value [W]
Switching loss	2.12 W
Switch conduction loss	1.08W
Inductor ohmic loss	2.98 W
Inductor core loss	0.11 W
Input capacitor loss	42.5 mW
Output capacitor loss	32 mW
Total losses dc/dc 1	6.36W

9.7.2 DC/DC 2

Figures 9.7.1A and 9.7.1.B show the switching transitions of the second dc/dc converter. Since the calculation of all the losses inside this converter are analogue to those in the first dc/dc converter these will not be elaborated further. A summary of all the losses can be found in table 9.7.1. At an output power of 179W, with 5.95W losses, this converter has an efficiency of 97%.

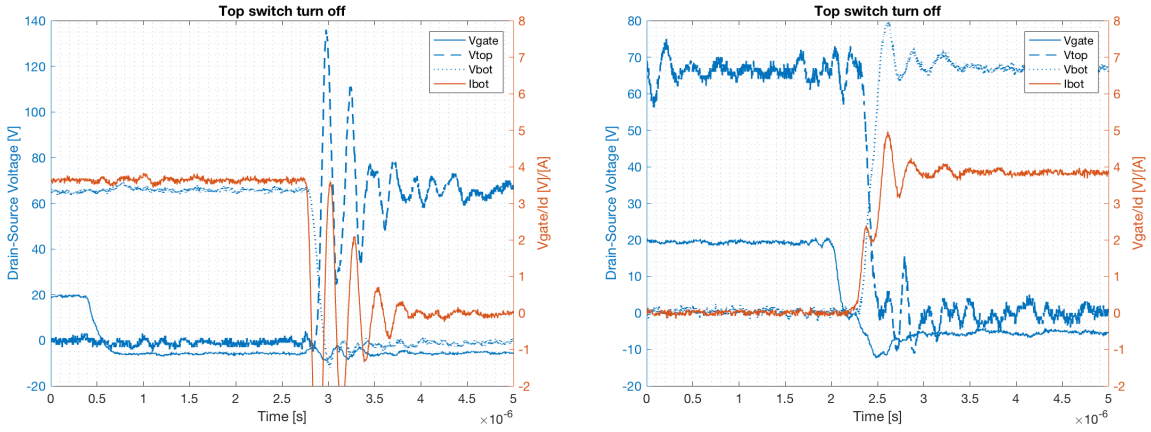

Figure 9.7.3: dc/dc 2 Switching waveforms

Quantity	Value [W]
Switching loss	1.68 W
Switch conduction loss	1.21 W
Inductor ohmic loss	2.88 W
Inductor core loss	0.13 W
Input capacitor loss	48.7 mW
Output capacitor loss	6.4 mW
Total losses dc/dc2	5.95 W

9.7.3 INVERTER

The losses inside the inverter are made up off switching losses, switch conduction losses and losses in the input capacitor. Figures 9.7.1a-d. show the switching transitions of the top switches in the full bridge. Due to symmetry, the switching transitions of the bottom right switch is similar to the top left switch, and bottom left is similar to top right. As can be seen from the figures the turn off is done with zero voltage. Due to a small deadtime the duty cycle is not exactly 50% and the turn on is not done with zero voltage, but almost zero current. Furthermore the figures show the voltage dependance of the gate drain capacitance with respect to the drain source voltage: as the drain source voltage decreases the gate drain capacitance increases which decreases the gate source voltage for a small amount of time.

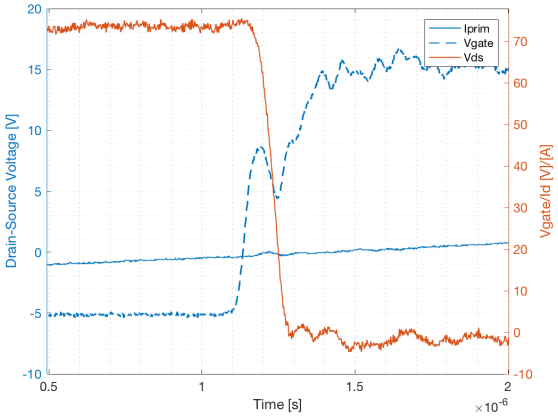

(a) Turn on

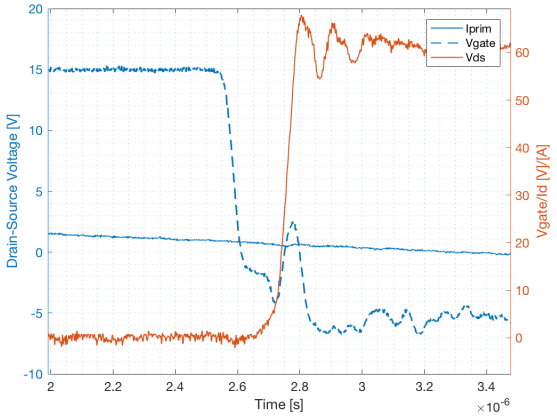

(b) Turn off

Figure 9.7.4: Top left switch transitions

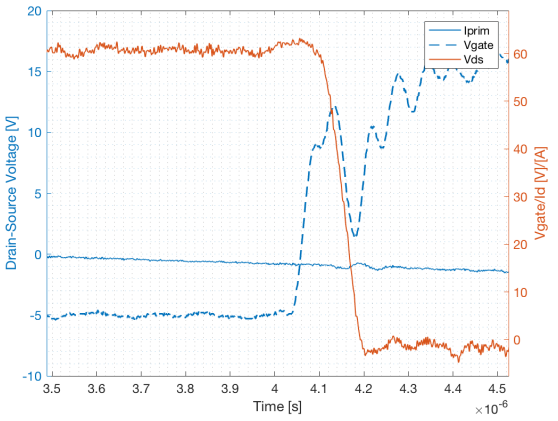

(a) Turn on

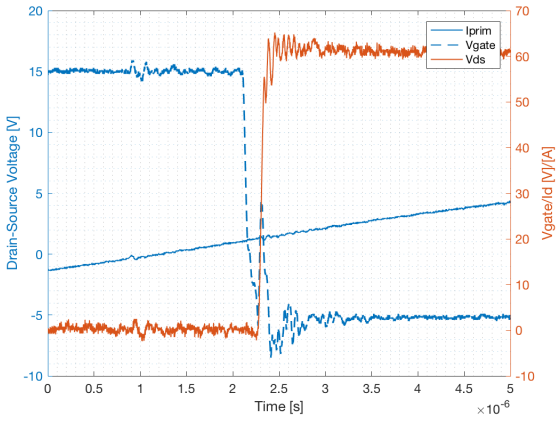

(b) Turn off

Figure 9.7.5: Top right switch

SWITCHING LOSSES

As said above, due to the resonant current the turn on transitions occur at almost zero current. In this section it will be show that the switching losses inside the inverter are negligible. To do this the turn on process of the top left switch is analyzed. Using the same approach as the for dc/dc 1. With a $V_{plateau} = 8V$ (Around this voltage the effect of a changing V_{DS} is seen). gives a current rise time $3.65ns$. Then using eq. (9.7.1.), with $V_{DS}(t_{ir}) = 67V$ and the device capacitances from the datasheet, the losses in this phase are equal to 17mW. During the voltage fall phase, using eq. (7.1.5) where $t_{vf} = 152ns$, $I_{prim,av}(phase3) = \frac{1}{2}A$, the losses are equal to $6.7\mu W$.
Since the resonant current is small ($\frac{1}{2}A$ average) at the time of switching and due to the fast switching of the SiC switches the switching losses are neglected.

CONDUCTION LOSSES

The conduction losses inside the inverter are equal to eq. (9.7.16), here the primary RMS current is $4.3A$ with an $80m\Omega$ on resistance. This results in a conduction loss of 1.48W.

$$P_{cond} = i^2_{prim,rms} R_{ds,on} \tag{9.7.16}$$

CAPACITANCE LOSSES

The final losses in the inverter are the losses in the input capacitance. The ripple current through these capacitors is equal to the RMS of the primary current. Metal film capacitors are used with an ESR of $3.1 m\Omega$. This results in negligible capacitor losses. The total losses inside the inverter are then approximately equal to the conduction losses which equal $350 mW$.

9.7.4 RECTIFIER

Since the rectifier is triggered by the inverter (with a 90° phase shift) and uses the same amount of deadtime, the switching behaviour is the same. This is also seen in the figures below. Therefor only the conduction losses are taken into account, these amount to 1.25W.

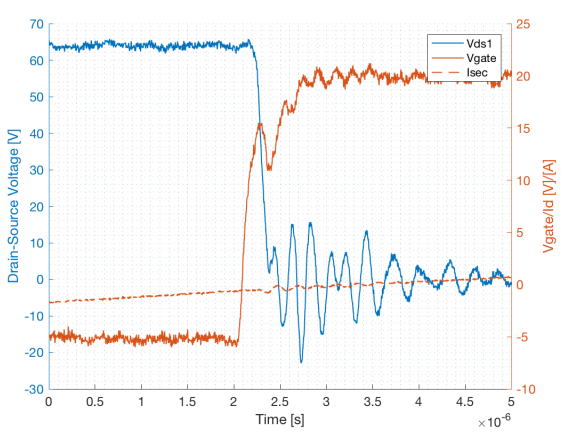

(a) Turn on

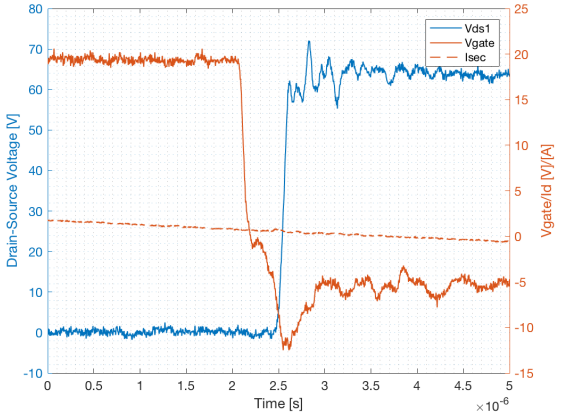

(b) Turn off

Figure 9.7.6: Top left switch transitions

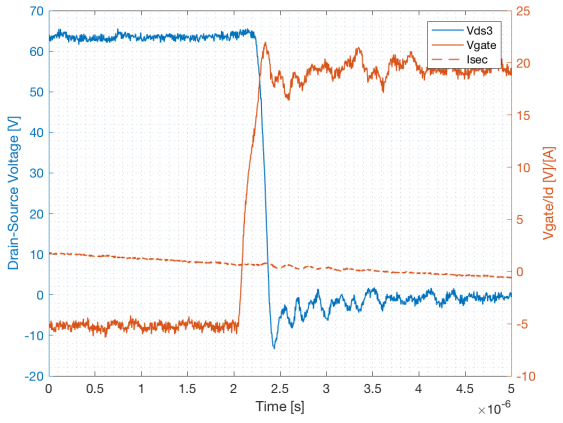

(a) Turn on

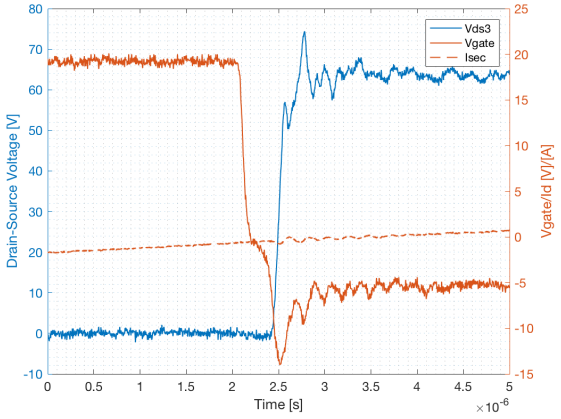

(b) Turn off

Figure 9.7.7: Top right switch transitions

9.7.5 RESONANT TANK LOSSES

In the resonant tank, power is also lost in the capacitors and in the transformer (Ohmic losses core losses and eddy current losses). All these losses are summed up in an equivalent AC resistance, the losses then equal:

$$P_{transformer} = I_{prim}^2 R_{AC,eq,prim} + I_{sec}^2 R_{AC,eq,sec} \tag{9.7.17}$$

Here $R_{AC,eq,prim}$ and $R_{AC,eq,sec}$ are equivalent AC resistance which are comprised of core losses, eddy current losses (in the aluminium shielding) and electrical resistance. These were obtained using a FEM analysis of a different project [2]. At a primary and secondary current of 6A these were determined to be 0.525Ω and 0.518Ω for primary and secondary respectively. At an a primary and secondary current of $4.2 A_{RMS}$ and $4.1 A_{RMS}$ respectively, the total losses in the transformer are 18.14W.

The last losses to be calculated are the losses inside the resonant capacitors. In the datasheet of the capacitors the dissipation factors are specified to be 0.1% at 100kHz. From this the ESR at 100kHz is calculated according to:

$$ESR = \frac{\sigma}{\omega C} \tag{9.7.18}$$

Which results in 0.55Ω at 100kHz and 18.29 nF. The total losses inside the capacitors are then

9.7.6 Total Losses

The total losses in the system are summarized in the table below:

Quantity	Value [W]
dc/dc 1	6.36 W
dc/dc 2	5.95 W
Inverter	1.48 W
Rectifier	1.25 W
Transformer	18.14W
Resonant Capacitors	19.13 W
Total calculated losses	52.3 W
Total measured losses	50.62 W

9.8 Appendix H: CREE evaluation boards

Figure 9.8.1 shows a picture of the evaluation board. The product number used for the kit is: KIT8020CRD8FF1217P-1. It uses two 1200V 10A MOSFETS (C2M0280120D) and two 1200V 33A SiC diodes (C4D20120D). For more information about the kit, MOSFETS and diode see: [38][39][40].

Figure 9.8.1: CREE evaluation board

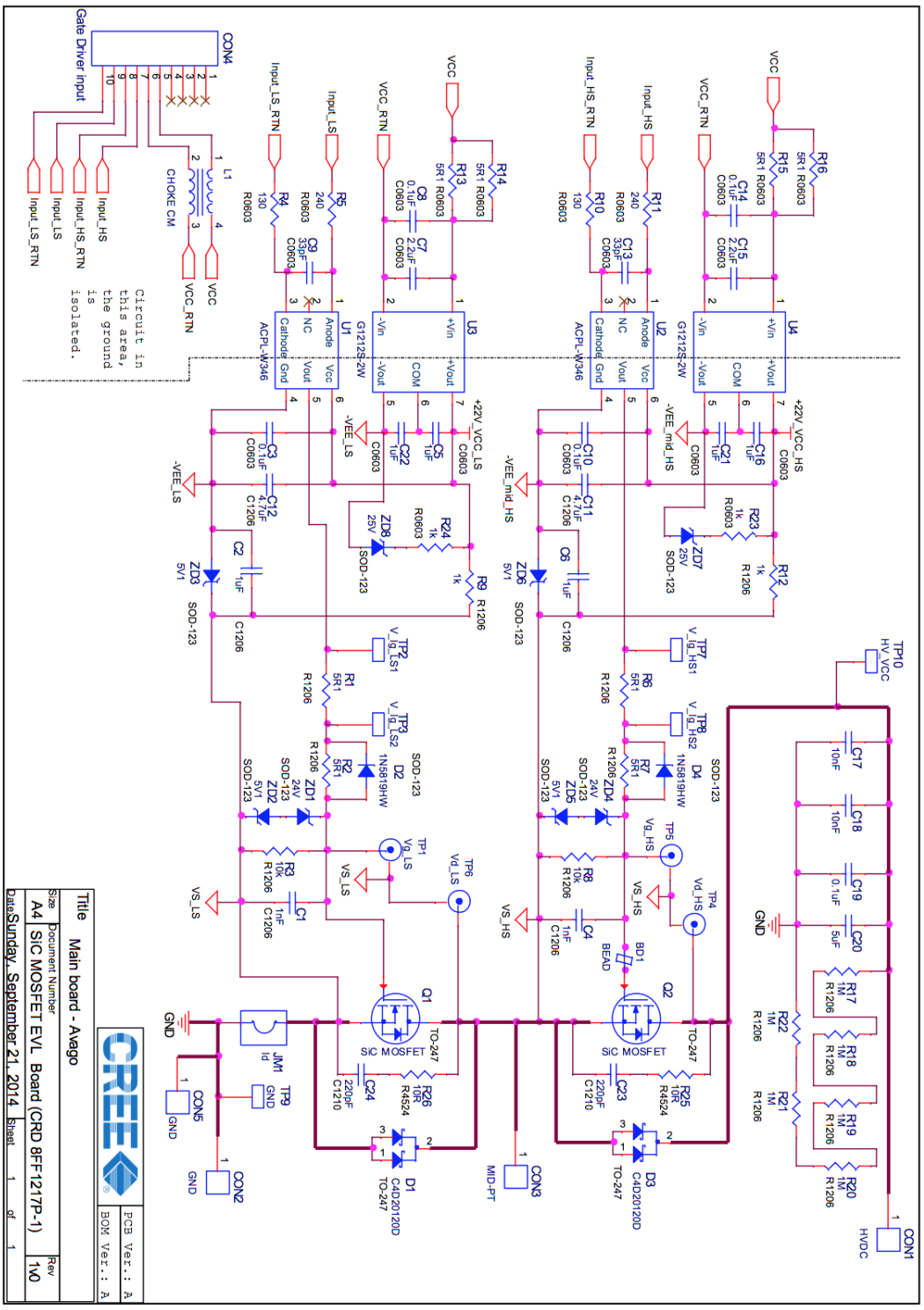

Figure 9.8.2: Schematic of CREE evaluation board

9.9 Appendix I: Capacitor Technologies

Figure 9.9.1 shows the operating ranges and losses for various capacitor ranges. From here it is clear that polypropylene is the best material for the operating conditions of the dc/dc converters.

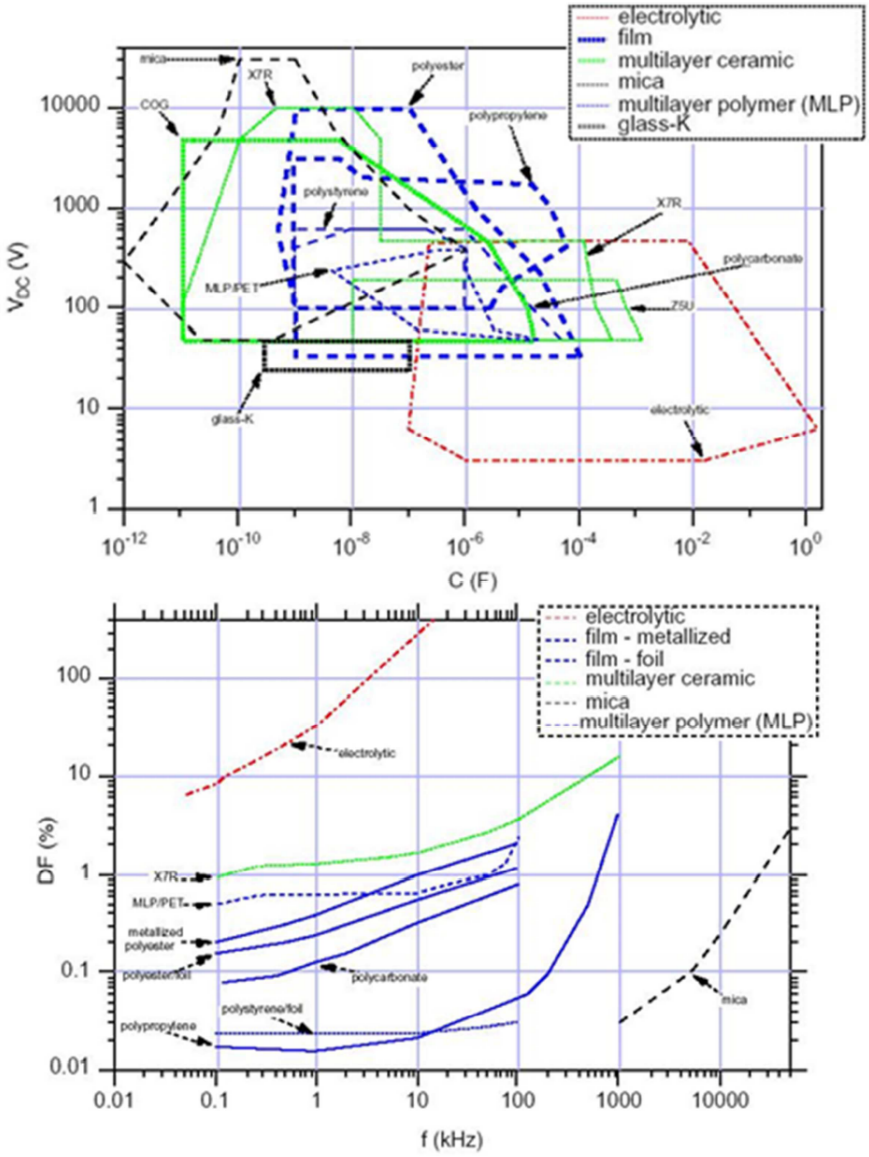

Figure 9.9.1: Various capacitor technologies and its operating ranges.

9.10 Appendix H: Magnetic Material Loss Coefficients

In the table below are the coefficients to calculate the hysteresis losses, for different ferrite materials.

FERROXCUBE
A YAGEO COMPANY

(f in Hz, B in T, T in deg C)

Freq 1.000.000
B 0,1
T 100

(see not in the bottom)

Material	Status	Freq min	Freq max	Cm	x_1	y_1	Ct2_1	Ct1_1	Ct_1	Freq chk			Pv (mw/cc)
3C90	Standard	20000	200001	3,2	1,46	2,75	0,000165	0,031	2,45	1	0	1	
3C91	Standard	10000	100000	3,5	1,4	2,5	0,000142	0,013	0,88	1	0	1	
3C91		100000	200000	3,5	1,4	2,5	0,000142	0,013	0,88	1	0	1	
3C91		200000	400001	3,33E-14	4,05	2,5	0,000142	0,013	0,88	1	0	1	
3C92	Design in	20000	100000	26,52000126	1,194999973	2,649999941	0,000267895	0,054329115	3,7539611	1	0	1	
3C92		100000	200000	0,349247262	1,589999964	2,67499994	0,000150599	0,030541568	2,548162342	1	0	1	
3C92		200000	400001	0,000119	2,24499995	2,66499994	0,000208173	0,04371632	3,289902504	1	0	1	
3C94	Standard	20000	150000	3,530102481	1,419999968	2,884999936	0,000125359	0,022263625	1,972776047	1	0	1	
3C94		150000	400000	0,000588	2,124999953	2,70499994	0,000116598	0,023272995	2,1613195	1	0	1	
3C94		400000	400001	0,0000021	2,6	2,75	0,000165	0,031	2,45	1	0	1	
3C95	Design in	20000	150000	92,16643453	1,045	2,44	4,62E-05	7,94E-03	1,332362959	1	0	1	
3C95		150000	300000	7,47E-03	1,955	3,07	6,06E-05	0,0126	1,654230769	1	0	1	
3C95		300000	400001	7,87E-04	2,055	2,535	9,55E-05	9,78E-03	1,022919887	1	0	1	
3C96	Design in	20000	100000	5,120544636	1,33999997	2,66499994	0,000547543	0,110384636	6,563034122	1	0	1	
3C96		100000	200000	0,082700122	1,719999962	2,804999937	0,000183438	0,036614276	2,827045247	1	0	1	
3C96		200000	400001	0,0000917	2,21999995	2,464999945	0,000232691	0,047189773	3,39206666	1	0	1	
3C97	Design in	20000	150000	42,36588301	1,16	2,8	6,35519E-05	0,01100719	1,465	1	0	1	
3C97		150000	300000	0,003448693	1,99	2,935	7,85219E-05	0,0136	1,575	1	0	1	
3C97		300000	400001	0,000449188	2,055	2,415	8,74899E-05	0,01403339	1,528	1	0	1	
3C98	Prototype	Coef not available		Best material for 100 kHz, 100 C. Contact sales for updates									
~~3F4~~	~~Standard~~	~~500000~~	~~3000000~~	~~1932000000~~	~~3,20E-02~~	~~3,185474956~~	~~0,000095~~	~~0,011~~	~~1,15~~	~~1~~	~~1~~	~~2~~	~~**1.961,25**~~
~~3F4~~		~~3000000~~	~~3000001~~	~~1680000000~~	~~3,20E-02~~	~~3,185474956~~	~~0,000034~~	~~0,0001~~	~~0,67~~	~~0~~	~~1~~	~~1~~	
3F36	Design in	100000	499999	6,83	1,43902	3,26718	0,000083946	0,010783518	1,232717265	1	0	1	
3F36		500000	799999	0,000112499	2,19515	2,71986	8,92639E-05	0,011719438	1,28161335	1	0	1	
3F36		800000	1200000	2,23928E-07	2,61053	2,49772	6,11871E-05	0,006141983	1,010843873	1	1	2	**3.305,61**
4F1	Prototype	3000000	5000000	19,525	1,37	2,425	9,01169E-05	0,01337335	1,436165854	0	1	1	
4F1		5000000	7500000	19,56258061	1,37	2,425	0,000149007	0,027	2,209933775	0	1	1	
4F1		7500000	10000001	21,3125	1,37	2,425	0,000237741	0,031001448	1,722733153	0	1	1	

Figure 9.10.1: Loss Coefficients of different ferrite materials

Loss Coefficients v2.pdf

9.11 Appendix J: Dowell's Graph

Figure 9.11.1 shows the relationship between the AC and DC resistance depending on the amount of layers used and the relative penetration depth in each wire.

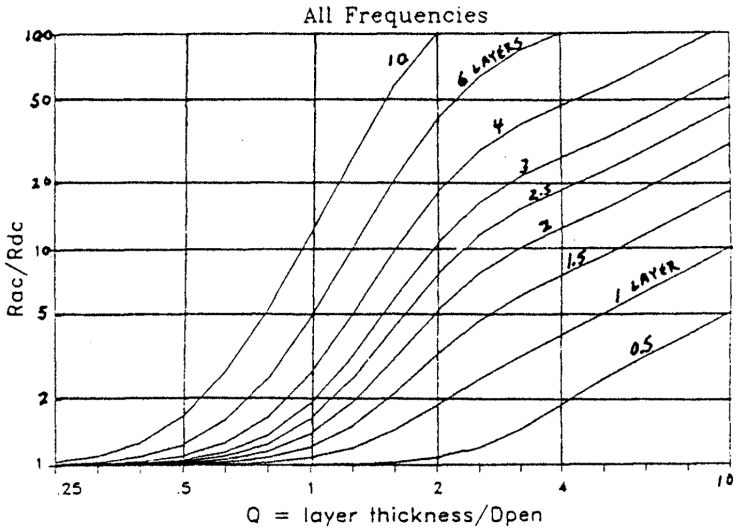

Figure 9.11.1: AC to DC resistance relationship [4]

9.12 Appendix K: Inductor Cores and Wires

Table 9.12.1 shows the different cores with part of their dimensions. Furthermore Table 9.12.2 shows the different wire types.

Table 9.12.1: Inductor cores

Number	Core	V_{ef} $[mm^3]$	A_{ef} $[mm^2]$	L_{ef} $[mm]$
1	ETD29/16/10	5260	81.4	64
2	ETD34/17/11	7640	97.1	78.6
3	ETD39/20/13	11500	125	92.2
4	ETD44/22/15	17800	173	103
5	ETD49/25/16	24000	211	114
6	ETD59/31/22	51500	368	139

Table 9.12.2: Inductor cores

Number	N	Wire diameter $[mm]$	Total diameter $[mm]$
1	1	0.2	0.22
2	1	0.3	0.32
3	1	0.4	0.43
4	1	0.5	0.55
5	1	0.6	0.65
6	130	0.071	1
7	280	0.071	1.51
8	600	0.071	2.16
9	130	0.04	0.54